Beyond the Born-Oppenheimer static surface model for molecule-surface reactions

Spiering, P.

Cover Page

The handle http://hdl.handle.net/1887/81817 holds various files of this Leiden University dissertation.

Author: Spiering, P.
Title: Beyond the Born-Oppenheimer static surface model for molecule-surface reactions
Issue Date: 2019-12-16

Beyond the

Born-Oppenheimer Static Surface Model

for Molecule-Surface Reactions

PROEFSCHRIFT

ter verkrijging van

de graad van Doctor aan de Universiteit Leiden,

op gezag van Rector Magnificus prof. mr. C. J. J. M. Stolker,

volgens besluit van het College voor Promoties

te verdedigen op maandag 16 december 2019

klokke 13:45 uur

door

Paul Spiering

geboren te Bergschenhoek, Nederland, 1990

Promotiecommissie

Promotor:	Prof. dr. G. J. Kroes
Co-promotor:	Dr. J. Meyer

Overige leden:	Prof. dr. H. S. Overkleeft	voorzitter
	Prof. dr. M. T. M. Koper	secretaris
	Prof. dr. H. Guo	University of New Mexico, Albuquerque, NM, USA
	Prof. dr. J. G. E. M. Fraaije	
	Dr. R. J. Maurer	University of Warwick, UK
	Dr. K. Doblhoff-Dier	

Contents

Acronyms

AIMD *ab-initio* molecular dynamics.

BOA Born-Oppenheimer approximation.

COM center of mass.

CRP corrugation reducing procedure.

DFPT density functional perturbation theory.

DFT density functional theory.

DOF degrees of freedom.

ehp electron-hole pair.

GGA generalised gradient approximation.

GLE generalized Langevin equation.

HEG homogeneous electron gas.

KS Kohn-Sham.

LDA local density approximation.

LDFA local density friction approximation.

MD molecular dynamics.

MDEF molecular dynamics with electronic friction.

MEP minimum energy path.

NN neural network.

ODF orbital-dependent friction.

PES potential energy surface.

QC quasi-classical.

RMSE root-mean-square error.

SCM static corrugation model.

SRP specific reaction parameter.

Chapter 1

Introduction

Chemical reactions convert some group of molecules, the reactants, into an other group of molecules, the products. It is then the job of a chemist to understand how and why these processes take place, at a fundamental level, in order to predict new chemical processes or improve existing ones. Fundamentally, a chemical process can be understood as a concerted movement of atoms constituting the reactants from their original arrangement to the arrangement making up the products. This concerted movement is governed by the interactions between these atoms. Figure 1.1 shows the total interaction between atoms, the potential energy, as a function of the arrangement of the atoms during their concerted movement from reactant state to product state (progress of reaction) in blue. Before the reactant can be converted into its product, it must generally first overcome a barrier in energy, where the interaction between atoms becomes more repulsive and an initial investment of energy is necessary. While this is sometimes understood as walking over a mountain, it is more accurate to compare it to walking through a mountain pass as movements of atoms in other directions than the concerted movement generally require even more energy. Once the chemical process is past the barrier, the invested energy is released again and can, in principle, be reused for other chemical processes. An example that should be well known to the general reader is lighting a campfire. First an initial energy source, heat, is added to wood
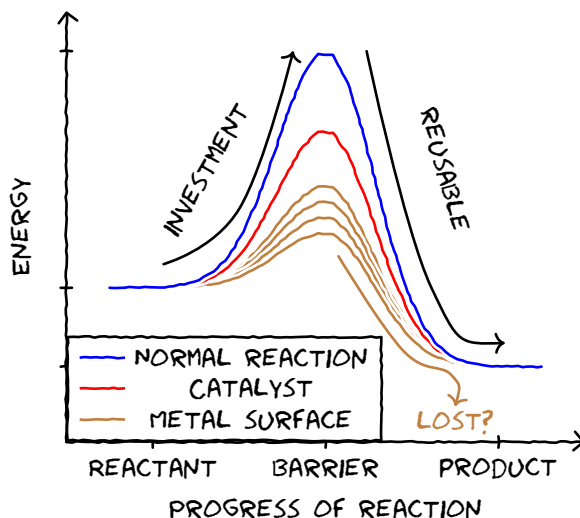
Figure 1.1: A schematic overview of the role of (heterogeneous) catalyis in chemical processes.

and O_2 in order to allow some of the atoms to rearrange into CO_2, H_2O and partially oxidated wood remains (e.g. ashes). The subsequently released energy can be reused to keep the wood burning. A simplified picture such as in figure 1.1 can not account for the complexity of burning wood and instead the total process can be broken down into a network of elementary reaction steps, which can no longer be further devided into smaller steps. These elementary reaction steps, which describe the conversion of specific reactants into products, are linked by providing their products as reactants for other elementary steps. Using the knowledge of these elementary reaction steps and their interconnection, a chemist can design a process in such a way that specific products are formed by choosing which, and the order in which, reactants are combined. Moreover, a chemist can use the understanding of these elementary reaction steps to determine the physical conditions for which they are more likely to commence than competing elementary reaction steps that do not yield the desired products. One such way is catalysis.

1.1 Heterogeneous Catalyis

In catalysis, an additional chemical substance, the catalyst, is added to reactants and interacts in such a way that the energy required to overcome the barrier of an elementary reaction step is changed. A special property of a catalyst is that it is found, in the same quantity, in both the reactants and the products, although it may only be regenerated after several elementary reaction steps and decay over time. This property means that instead of introducing a new elementary reaction step with different reactants and products, catalysis can be considered as modifying (several) elementary reaction steps. In Fig. 1.1 this is indicated in red, where the reactant and product energies remain the same, whereas the barrier has decreased. By selectively increasing and decreasing barrier heights of elementary steps, it is possible to 'guide' the reactants towards desired products.

Heterogeneous catalysis [1], where the catalyst is in a different phase than the products and reactants, is used on a large scale in industry [2]. The importance of heterogeneous catalysis in our current society can not be overstated. It is used in the electrolytic production of H_2 as well as in hydrogen fuel cells using that H_2. Gaseous exhaust fumes from car engines are ran past metal surfaces to convert the more toxic and environmentally burdening compounds to more acceptable ones [3]. One of the most influential chemical processes, both on lives [4] and deaths [5], is the conversion of H_2 and N_2 to NH_3 in the heterogeneously catalysed Haber-Bosch process [6]. White [5] argues that up to 150 million deaths can be directly attributed to weapons manufactured that make use of NH_3 produced using the Haber-Bosch process. On the flip side, Erisman et al. [4] show that about half (48%) of the world's population in 2008 is sustained due to artifical fertilizers, again made from NH_3 resulting from the Haber-Bosch process. They expect the contribution of Haber-Bosch NH_3 to only grow. Moreover, they state that approximately 1% of the world's primary energy source is used for the Haber-Bosch process. This thoroughly motivates studying the underlying elementary reaction steps of these processes as a small improvement in the catalyst can, even with a tiny improvement, reduce energy consumption and polution, enormously

in absolute amounts. In fact, Ertl and coworkers have already studied these elementary reaction steps experimentally, for which Ertl has been awarded the 2007 Nobel prize in chemistry [7].

1.2 Metal Surfaces as Catalysts for Molecules

A large group of effective catalysts for the conversion of small molecules consists of metal surfaces. Unlike for molecules, the electrons of a metal (surface) are delocalized and are thus more conveniently described according to their momuntum instead of position. This view of electrons is typically associated with a "physical" rather than "chemical" picture [8]. The quantum mechanical states of these electrons are grouped together in bands. What distinguishes a metal from other crystalline solids is the fact that at least on such band crosses the so-called Fermi level that separates occupied from unoccupied states.

Electrons of a molecule are more conveniently described by localized orbitals in a more chemical picture. It is exactly the fact that these two pictures meet that makes metal surfaces so interresting as a catalyst. The metal surface has electrons available that can be donated to the molecule at hardly any energetic cost and, likewise, can accept an electron from the molecule. These exchanges of electrons are what facilitates the lowering of the barrier in Fig. 1.1.

1.3 Interaction of Molecules with Metal Surfaces

The exact way in which a metal surface modifies the potential energy of molecules must be understood at a fundamental level in order to make accurate predictions for industrially relevent catalytic processes. To study these processes, it is necessary to design controlled experiments. A top-down approach starts from industrially relevant conditions, which makes it very challenging to disentangle the multitude of concurrently competing effects. The surface science approach to heterogeneous catalysis on the other hand is from the bottom up, where extremely simplified elementary reaction steps

are studied and subsequently combined until the industrial conditions are reproduced. Ideally, both approaches can complement each other on the way towards understanding how to design better catalysis.

This thesis focusses on the bottom-up approach, starting from the Schrödinger equation [9] to understand specific elementary reaction steps. One way to study elementary reaction steps, like, e.g., dissociative chemisorption, which is often the rate limiting step in the Haber-Bosch process, is the study of molecular beam experiments [10–14]. These experiments study the fate of molecules that are prepared in a beam directed towards a (single crystal) surface.

1.4 Aim of this Thesis

The main topic of this thesis is the theoretical description of the reactive scattering of small molecules with transition metal surfaces beyond the Born-Oppenheimer static surface model. One particular goal is to obtain fundamental understanding of the processes governing the exchange of energy between molecules and metal surfaces by comparing simulations at different levels of theory both with each other and experimental results. Specifically, energy exchange beyond the Born-Oppenheimer approximation (facilitated by the lack of a band gap for electronic excitations in the metal surface) at the level of molecular dynamics with electronic friction (MDEF) is compared with experiments.

In Chap. 2 established theory that is commenly used for modeling molecular beam experiments is summarized. First, the theoretical background behind potential energy surfaces is described, followed by the quasi-classical trajectory method [15–17] for studying surface reactions. Afterwards, the generalized Langevin equation is introduced in order to model electronically non-adiabatic effects with a friction tensor [18–25]. This chapter concludes with details on how to compute electronic friction tensors using two different (sets of) approximations: the local density friction approximation (LDFA) [26–29] and the orbital dependent friction (ODF) method [18–25].

In Chap. 3 , the aim is to improve a previously developed Static Corrugation Model (SCM) [30] in order to describe reactive scattering at elevated surface temperatures. A large database of energies of surface atom displacements of a surface-adsorbate system is necessary for constructing and validating the improved SCM [31].

In Chap. 4 , the focus is on accurately describing electronically non-adiabatic effects for the reactive scattering of H_2 and D_2 on Cu(111) using electronic friction theory [24]. A continuous representation of the friction tensor is necessary in order to obtain the large amount of trajectories required for computing observables such as the dissociative chemisorption probability and rovibrationally (in)elastic scattering probabilities with sufficient statistical averaging.

In Chap. 5 , orbital-dependent friction (ODF) is used to model the reactive scattering of N_2 on Ru(0001) [25] as earlier both experimental and theoretical work by Luntz and coworkers [32, 33] had suggested that non-adiabatic effects may be extremely important for this system.

In Chap. 6 , the goal is to develop and compare machine learning models for continuous representations of electronic friction tensors, which account for symmetry properties of molecule-surface systems.

1.5 Main Results

This section summarizes the main scientific results obtained during the research that resulted in this thesis.

Chapter 3: An Improved Static Corrugation Model

The computationally efficient static corrugation model (SCM), which describes reactive scattering at elevated temperatures and is based on the sudden approximation, was improved by adding three-body interactions for H_2 on Cu(111). The improvement was achieved by making the parameters defining the model from Wijzenbroek and Somers

[30] linearly dependent on the H_2-bond distance and thus effectively including three-body effects. The three-body static corrugation model (SCM) was fitted using 15 113 configurations with either one or two surface atom displacements. At elevated surface temperatures of 900 K, both using 6-dimensional dynamics with the specific reaction parameter (SRP)48 density functional [16] in combination with the SCM or using [34] full dimensional dynamics (i.e. *ab-initio* molecular dynamics, AIMD) with SRP48 [35] accurately reproduces experimental reaction probabilities of associative desorption. Theory and experiment are not in agreement for molecules in the rovibrational ground state, which is attributed to the intrinsic, and not the extrinsic, curvature of the potential energy surface (PES) along the minimum energy path (MEP). Considering the sudden approximation made in the SCM, it can thus be concluded that surface motion is not important to obtain a chemically accurate description of those experiments for H_2 on Cu(111). It is, however, neccesary to take into account the change of the H_2-Cu(111)interaction potential due to Cu atoms being displaced from their equilibrium position at elevated temperatures.

Chapter 4: Testing Electronic Friction Models

Orbital-dependent friction (ODF) coefficients were computed for H_2 on a frozen Cu(111) surface to obtain 6×6 electronic friction tensors [24]. Good agreement was found between the newly calculated ones and the (by nowadays computational possibilities) very few reported ones by Luntz et al. [33] along a reaction path towards dissociation. The 21 independent elements of these tensors were subsequently fitted to construct a continuous neural network (NN) representation with symmetry adapted coordinates [36]. Electronic friction coefficients according to the local density friction approximation (LDFA) [26–29] were also calculated bases on the electron density of the clean Cu(111) surface by treating both hydrogen atoms as independent and continuously represented by a NN afterwards. MDEF simulations mimicking molecular beam experiments using both ODF and LDFA coefficients showed no significantly different H_2 dissociation probabilities compared to each other, and compared to simulations without electronic friction (i.e. within the Born-Oppenheimer static surface approximation). State-to-

state scattering probabilities, on the other hand, are heavily affected by including electronic friction and also by whether ODF or LDFA is used as the friction model. Moreover, comparing the difference in initial and final kinetic energy for these simulations of state-to-state scattered molecules allows one to distinguish between the ODF and LDFA models. This suggests "fingerprint" experiments for validating inherent approximations of both models.

Chapter 5: Effect of Orbital-Dependent Friction

A continuous NN representation was obtained for ODF tensors of N_2 on Ru(0001). Molecular beam simulations using MDEF [17] were performed including the effects of elevated surface temperatures ($T_s = 575K$). Initial dissociative sticking probabilities for N_2 on Ru(0001) are approximately two times smaller when ODF is used as the friction model compared to LDFA, which also improves the agreement with the best currently available experimental data. Like for most other systems, LDFA yields the same results as simulations without electronic friction. Furthermore, considering the best estimates based on experimental data, ODF also improves the description of energy exchange with the surface. One of the main challenges for describing N_2 scattering from Ru(0001) is the correct description of the quenching of vibrational excitation. ODF was the only model that predicts enough vibrational quenching to fall within the experimentally determined bounds. Only when taking into account both surface motion and ODF was it possible to accurately reproduce experiments.

Chapter 6: Machine-Learning based Representations

First, a formalism is presented to describe symmetry properties of electronic friction tensors for molecules on frozen metal surfaces. Two methods result that allows these properties to be enforced on machine learning algorithms: an "*a priori*" and an "*a posteriori*" method. These methods can be seen as an extension to established methods used to obtain symmetry adapted potential energy surfaces. For symmetry adapted machine-learning based potential energy surfaces the neural network is presented with

symmetry adapted coordinates or descriptors such that the neural network yields the same result for symmetry equivalent inputs. For tensors, it is necessary to also transform the outputs in a symmetry adapted way. In this chapter a comparison is made on how different symmetry adapted coordinates can affect the fitting accuracy and computational efficiency of neural-network-based machine learning models. The best result is obtained for an analytical "*a priori*" continuous representation when using "asymmetric" contributions. Another accurate method is to use a simple expression for mapping coordinates to a single unit cell and subsequently applying the "*a posteriori*" method to correct for the symmetry contraints. Also a method based on the work of Jiang and coworkers [21, 22] is shown to provide accurate fits, although discontinuities are found. Furthermore, two different ways to obtain tensors as an output from neural networks are compared. The elements of the tensor can either be obtained by assigning a unique neural network to each element, or by constructing a neural network with multiple outputs and subsequently arrange these outputs as a tensor. Positive definite tensors can be enforced by generating a lower triangular tensor that is subsequently squared. The best results are obtained for single neural networks with multiple outputs where positive definiteness is enforced.

1.6 Outlook

While the scientific results reported in this thesis are only a small step to fundamentally understand how to go beyond the Born-Oppenheimer static surface approximation, it paves the way for many further advances.

The newly improved static corrugation model (SCM) provides many new theoretical opportunities. Using a simple and physically meaningful analytical expression with few parameters, it might become possible to use the SCM for nuclear quantum dynamics. It is not clear what the effect of surface temperature would be in combination with quantum dynamics. These quantum dynamical calculations need a potential energy surface that does not contain any unphysical features such as very localized peaks in the second derivative [37, 38]. Moreover, an accurate description of the potential energy surface is

also needed outside of the classically accesible region. Usually, high-dimensional neural networks, which is an alternative way to include the effect of surface displacements, contain small unphysical features and only accurately fit the clasically accesible region. Unlike high-dimensional neural networks, these are no issues for the SCM, although the accuracy of the fit is generally lower compared to neural networks. In combination with a sudden approximation, where multiple quantum dynamical calculations are performed for differently initialized surface displacements, the SCM can thus be used as a potential energy surface for wave-packet calculations [39] where surface temperature is taken into account quantum mechanically.

In order to obtain a potentially more accurate fit for the SCM, it is possible to replace the Rydberg-like potenial, which is used for the SCM in this thesis, with a low dimensional neural network fit. For such a low-dimensional fit it would be possible inspect if any of the aforementioned problems of high-dimensional neural networks are present, thus still allowing its use for quantum dynamics.

The current SCM does not allow for a description of the movement of surface atoms, which means that it does not account for energy transfer to the surface. Instead, only the effect on the movement of the absorbate due to displacements of the surface atom is taken into account. This effect could be trivially included by adding a "strain" potential which describes the interaction between surface atoms. Such an interaction is conveniently described using an embedded atom potential [40] and would allow for the description of surface motion without sacrificing the advantages of the SCM.

The large influence of ODF found for the dissociative chemisorption of N_2 on Ru(0001) is very important. Until now, electronic friction commonly based on LDFA for the simulation of molecular beam experiments has never been shown to significantly affect experimental observables. The results presented here show electronic friction can have such effects after all, although limitations on both the experimental and theoretical side prevent unequivocal verification of the importance of Beyond-Born-Oppenheimer effects for systems that are commenly considered as "weakly non-adiabatic". This justifies further experimental and theoretical research in electronically non-adiabatic effects of molecular beam experiments and its connection to catalysis.

One of the major limitations for the verification of (ODF) electronic friction theory is the availability of specific experiments and the accuracy of currently available experimental data. While for theoretical modeling one can simply "switch off" the coupling between the electronic and nuclear system, this is option is not available for experiments. Therefore, it is neccesary to find observables which are mainly or at best only sensitive to non-adiabatic effects, and thus hardly or not at all affected by other theoretical shortcomings. The results from Chap. 4 enable the design of such an experiment. The energy loss during rovibrationally inelastic scattering of H_2 on Cu(111) turns out to be a "fingerprint" that is essentially independent of other state-of-the-art theoretical approximations like e.g. potential surfaces based on density functional theory (DFT).

Furthermore, there is now also new motivation for further improvements on theoretical modeling. In comparison to the many years of development of obtaining accurate PESs from DFT, there is hardly any systematic research on the effect of many of the approximations inherent to the use of electronic friction theory in practice. While some work on this topic is being done, and it is now possible for different groups to obtain comparable values for ODF tensors, this research is far from being complete.

The range of the chemical space that has been explored with the electronically non-adiabatic methods presented in this thesis is extremely small. Only N_2 on Ru(0001) and H_2 on Cu(111) are have been investigated here. Other researchers have also investigated H_2 on Pd [19, 23], CO on Cu(100) [19, 23, 41] and H_2 on Ag(111) [18, 21, 22]. For understanding the potential relevance of non-adiabatic effects in heterogeneous catalysis this is only a very first step - a much larger database including different molecules on different transition metal surfaces is required.

The continuous representation of electronic friction tensors has proven to be quite challenging. The machine learning models I present in Chap. 6 allows to obtain such a description using symmetry adapted coordinates. The asymmetric contributions neccesary to describe the symmetry correctly can so far not be obtained systematically. One way to obtain a "universal" solution could be to use embedded atom density based descriptors as symmetry adapted inputs for these models, as has recently been shown

to be advantageous for potential energy surfaces [42]. These descriptors are defined as fictitious electron densities imposed on each atom in the system due to each other atom in the system. Specifically, these descriptors need to include angular contributions in the form of

$$x^{l_x} y^{l_y} z^{l_z}, \tag{1.1}$$

where x, y, and z are the Cartesian distances between two atoms in the system and l_i are integer parameters. It is then possible to define 8 partitions based on all combinations of the signs of x, y, and z. By taking each partition as an asymetric contribution, the correct symmetric continuous representation of (electronic friction) tensors is obtained for any system consisting of atoms.

Ultimately, a better understanding of the energy dissipation dynamics during chemical reactions on transition metal surfaces that are relevant for heterogeneous catalysis could be a first step towards reducing the energy consumption of chemical reactors used for industrial processes.

References

[1] R. Schlögl. "Heterogeneous Catalysis". In: *Angew. Chem. Int. Ed.* 54 (2015), pp. 3465–3520. DOI: 10.1002/anie.201410738.

[2] Z. Ma and F. Zaera. "Heterogeneous Catalysis by Metals". In: *Encyclopedia of Inorganic Chemistry*. American Cancer Society, 2006. DOI: 10.1002/0470862106.ia084.

[3] P. A. J. Bagot. "Fundamental Surface Science Studies of Automobile Exhaust Catalysis". In: *Mater. Sci. Technol.* 20 (2004), pp. 679–694. DOI: 10.1179/026708304225016789.

[4] J. W. Erisman, M. A. Sutton, J. Galloway, Z. Klimont, and W. Winiwarter. "How a Century of Ammonia Synthesis Changed the World". In: *Nat. Geosci.* 1 (2008), pp. 636–639. DOI: 10.1038/ngeo325.

[5] M. White. *Historical Atlas of the 20th Century*. http://users.erols.com/mwhite28/20centry.htm. 2003.

[6] G. Ertl. "Surface Science and Catalysis—Studies on the Mechanism of Ammonia Synthesis: The P. H. Emmett Award Address". In: *Catal. Rev.* 21 (1980), pp. 201–223. DOI: 10.1080/03602458008067533.

[7] G. Ertl. "Reactions at Surfaces: From Atoms to Complexity (Nobel Lecture)". In: *Angew. Chem. Int. Edit.* 47 (2008), pp. 3524–3535. DOI: 10.1002/anie.200800480.

[8] R. Hoffmann. "Building Bridges Between Inorganic and Organic Chemistry (Nobel Lecture)". In: *Angew. Chem. Int. Ed.* (1982), pp. 711–724. DOI: 10.1002/anie.198207113.

[9] E. Schrödinger. "An Undulatory Theory of the Mechanics of Atoms and Molecules". In: *Phys. Rev.* 28 (1926), p. 1049. DOI: 10.1103/PhysRev.28.1049.

[10] H. A. Michelsen, C. T. Rettner, and D. J. Auerbach. "On the Influence of Surface Temperature on Adsorption and Desorption in the D_2/Cu(111) System". In: *Surf. Sci.* 272 (1992), pp. 65–72. DOI: 10.1016/0039-6028(92)91422-8.

[11] L. Diekhöner, H. Mortensen, A. Baurichter, and A. C. Luntz. "Laser Assisted Associative Desorption of N2 and CO from Ru(0001)". In: *J. Chem. Phys.* 115 (2001), pp. 3356–3373. DOI: 10.1063/1.1386810.

[12] O. Bünermann, H. Jiang, Y. Dorenkamp, A. Kandratsenka, S. M. Janke, et al. "Electron-Hole Pair Excitation Determines the Mechanism of Hydrogen Atom Adsorption". In: *Science* 350 (2015), pp. 1346–1349. DOI: 10.1126/science.aad4972.

[13] H. Mortensen, E. Jensen, L. Diekhöner, A. Baurichter, A. C. Luntz, et al. "State Resolved Inelastic Scattering of N2 from Ru(0001)". In: *J. Chem. Phys.* 118 (2003), pp. 11200–11209. DOI: 10.1063/1.1575210.

[14] C. T. Rettner, D. J. Auerbach, and H. A. Michelsen. "Observation of Direct Vibrational Excitation in Collisions of H_2 and D_2 with a Cu(111) Surface". In: *Phys. Rev. Lett.* 68 (1992), pp. 2547–2550. DOI: 10.1103/PhysRevLett.68.2547.

[15] C. Diaz, R. A. Olsen, H. F. Busnengo, and G.-J. Kroes. "Dynamics on Six-Dimensional Potential Energy Surfaces for H2/Cu(111): Corrugation Reducing Procedure versus Modified Shepard Interpolation Method and PW91 versus RPBE". In: *J. Phys. Chem. C* 114 (2010), pp. 11192–11201. DOI: 10.1021/jp1027096.

[16] C. Díaz, E. Pijper, R. A. Olsen, H. F. Busnengo, D. J. Auerbach, et al. "Chemically Accurate Simulation of a Prototypical Surface Reaction: H2 Dissociation on Cu(111)". In: *Science* 326 (2009), pp. 832–834. DOI: 10.1126/science.1178722.

[17] K. Shakouri, J. Behler, J. Meyer, and G.-J. Kroes. "Analysis of Energy Dissipation Channels in a Benchmark System of Activated Dissociation: N2 on Ru(0001)". In: *J. Phys. Chem. C* 122 (2018), pp. 23470–23480. DOI: 10.1021/acs.jpcc.8b06729.

1

[18] R. J. Maurer, B. Jiang, H. Guo, and J. C. Tully. "Mode Specific Electronic Friction in Dissociative Chemisorption on Metal Surfaces: H_2 on Ag(111)". In: *Phys. Rev. Lett.* 118 (2017), p. 256001. DOI: 10.1103/PhysRevLett.118.256001. arXiv: 1705.09753 [cond-mat.mtrl-sci].

[19] M. Askerka, R. J. Maurer, V. S. Batista, and J. C. Tully. "Role of Tensorial Electronic Friction in Energy Transfer at Metal Surfaces". In: *Phys. Rev. Lett.* 116 (2016), p. 217601. DOI: 10.1103/PhysRevLett.116.217601.

[20] R. J. Maurer, M. Askerka, V. S. Batista, and J. C. Tully. "Ab Initio Tensorial Electronic Friction for Molecules on Metal Surfaces: Nonadiabatic Vibrational Relaxation". In: *Phys. Rev. B* 94 (2016), p. 115432. DOI: 10.1103/PhysRevB.94.115432.

[21] Y. Zhang, R. J. Maurer, H. Guo, and B. Jiang. "Hot-Electron Effects during Reactive Scattering of H_2 from Ag(111): The Interplay between Mode-Specific Electronic Friction and the Potential Energy Landscape". In: *Chem. Sci.* 10 (2019), pp. 1089–1097. DOI: 10.1039/C8SC03955K.

[22] R. J. Maurer, Y. Zhang, H. Guo, and B. Jiang. "Hot Electron Effects during Reactive Scattering of H_2 from Ag(111): Assessing the Sensitivity to Initial Conditions, Coupling Magnitude, and Electronic Temperature". In: *Faraday Discuss.* 214 (2019), pp. 105–121. DOI: 10.1039/C8FD00140E.

[23] M. Askerka, R. J. Maurer, V. S. Batista, and J. C. Tully. "Erratum: Role of Tensorial Electronic Friction in Energy Transfer at Metal Surfaces [Phys. Rev. Lett. 116, 217601 (2016)]". In: *Phys. Rev. Lett.* 119 (2017), p. 069901. DOI: 10.1103/PhysRevLett.119.069901.

[24] P. Spiering and J. Meyer. "Testing Electronic Friction Models: Vibrational De-Excitation in Scattering of H_2 and D_2 from Cu(111)". In: *J. Phys. Chem. Lett.* 9 (2018), pp. 1803–1808. DOI: 10.1021/acs.jpclett.7b03182.

[25] P. Spiering, K. Shakouri, J. Behler, G.-J. Kroes, and J. Meyer. "Orbital-Dependent Electronic Friction Significantly Affects the Description of Reactive Scattering of N_2 from Ru(0001)". In: *J. Phys. Chem. Lett.* 10 (2019), pp. 2957–2962. DOI: 10.1021/acs.jpclett.9b00523.

[26] M. Alducin, R. Díez Muiño, and J. I. Juaristi. "Non-Adiabatic Effects in Elementary Reaction Processes at Metal Surfaces". In: *Prog. Surf. Sci.* 92 (2017), pp. 317–340. DOI: 10.1016/j.progsurf.2017.09.002.

[27] M. J. Puska and R. M. Nieminen. "Atoms Embedded in an Electron Gas: Phase Shifts and Cross Sections". In: *Phys. Rev. B* 27 (1983), p. 6121. DOI: 10.1103/PhysRevB.27.6121.

[28] N. Gerrits, J. I. Juaristi, and J. Meyer. "Atoms in Jellium Revisited - Implications for the Local Density Friction Approximation?" In: *Prep.* (2017).

[29]   P. M. Echenique, R. M. Nieminen, and R. H. Ritchie. "Density Functional Calculation of Stopping Power of an Electron Gas for Slow Ions". In: *Solid State Communications* 37 (1981), pp. 779–781. DOI: `10.1016/0038-1098(81)91173-X`.

[30]   M. Wijzenbroek and M. F. Somers. "Static Surface Temperature Effects on the Dissociation of H2 and D2 on Cu(111)". In: *J. Chem. Phys.* 137 (2012), p. 054703. DOI: `10.1063/1.4738956`.

[31]   P. Spiering, M. Wijzenbroek, and M. F. Somers. "An Improved Static Corrugation Model". In: *J. Chem. Phys.* 149 (2018), p. 234702. DOI: `10.1063/1.5058271`.

[32]   A. C. Luntz and M. Persson. "How Adiabatic Is Activated Adsorption/Associative Desorption?" In: *J. Chem. Phys.* 123 (2005), p. 074704. DOI: `10.1063/1.2000249`.

[33]   A. C. Luntz, I. Makkonen, M. Persson, S. Holloway, D. M. Bird, et al. "Comment on "Role of Electron-Hole Pair Excitations in the Dissociative Adsorption of Diatomic Molecules on Metal Surfaces"". In: *Phys. Rev. Lett.* 102 (2009), p. 109601. DOI: `10.1103/PhysRevLett.102.109601`.

[34]   F. Nattino, C. Díaz, B. Jackson, and G.-J. Kroes. "Effect of Surface Motion on the Rotational Quadrupole Alignment Parameter of D_2 Reacting on Cu(111)". In: *Phys. Rev. Lett.* 108 (2012), p. 236104. DOI: `10.1103/PhysRevLett.108.236104`.

[35]   F. Nattino, A. Genova, M. Guijt, A. S. Muzas, C. Díaz, et al. "Dissociation and Recombination of D_2 on Cu(111): Ab Initio Molecular Dynamics Calculations and Improved Analysis of Desorption Experiments". In: *J. Chem. Phys.* 141 (2014), p. 124705. DOI: `10.1063/1.4896058`.

[36]   J. Meyer. "Ab Initio Modeling of Energy Dissipation during Chemical Reactions at Transition Metal Surfaces". PhD thesis. Freie Universität Berlin, Freie Universität Berlin, Germany, 2012.

[37]   S. Manzhos and T. Carrington. "A Random-Sampling High Dimensional Model Representation Neural Network for Building Potential Energy Surfaces". In: *J. Chem. Phys.* 125 (2006), p. 084109. DOI: `10.1063/1.2336223`.

[38]   S. Manzhos, R. Dawes, and T. Carrington. "Neural Network-Based Approaches for Building High Dimensional and Quantum Dynamics-Friendly Potential Energy Surfaces". In: *Int. J. Quantum Chem.* 115 (2015), pp. 1012–1020. DOI: `10.1002/qua.24795`.

[39]   S. Nave, D. Lemoine, M. F. Somers, S. M. Kingma, and G.-J. Kroes. "Six-Dimensional Quantum Dynamics of (V=0,J=0)D2 and of (V=1,J=0)H2 Scattering from Cu(111)". In: *J. Chem. Phys.* 122 (2005), p. 214709. DOI: `10.1063/1.1902944`.

1

[40] M. I. Baskes. "Modified Embedded-Atom Potentials for Cubic Materials and Impurities". In: *Phys. Rev. B* 46 (1992), pp. 2727–2742. DOI: 10.1103/PhysRevB.46.2727.

[41] D. Novko, M. Alducin, and J. I. Juaristi. "Electron-Mediated Phonon-Phonon Coupling Drives the Vibrational Relaxation of CO on Cu(100)". In: *Phys. Rev. Lett.* 120 (2018), p. 156804. DOI: 10.1103/PhysRevLett.120.156804.

[42] Y. Zhang, C. Hu, and B. Jiang. "Embedded Atom Neural Network Potentials: Efficient and Accurate Machine Learning with a Physically Inspired Representation". In: *ArXiv Phys.* (July 2019). arXiv: 1907.06159 [physics].

1

Chapter 2

Theory

This chapter details the theoretical background neccesary to describe the interactions between molecules and metal surfaces needed for performing dynamical simulations, which can be directly compared with molecular beam experiments. In the scope of this thesis, the focus is on homonuclear diatomic molecules. In order to simplify the presentation, atomic units are used throughout this chapter ($\hbar = m_e = 1$).

2.1 Simulations of Molecular Beam Experiments

In a molecular beam experiment, molecules can be prepared in a specific (subject to experimental challenges) vibrational, rotational and electronic quantum state $|\Psi\left(\mathbf{R}, \mathbf{r}, t\right)_0\rangle$ in the gas phase. Obviously, the molecules are prepared in such a way that they are on a trajectory to collide with a surface. In principle, the time dependent Schrödinger equation can be used to model the time evolution of this experiment given the initial condition $|\Psi\left(\mathbf{R}, \mathbf{r}, t\right)_0\rangle$ according to

$$i\hbar\frac{\partial}{\partial t}\left|\Psi\left(\mathbf{R}, \mathbf{r}, t\right)\right\rangle = \hat{H}\left|\Psi\left(\mathbf{R}, \mathbf{r}, t\right)\right\rangle, \tag{2.1}$$

where $|\Psi\left(\mathbf{R}, \mathbf{r}, t\right)\rangle$ is the wave function of the system with nuclei $\mathbf{R}$ and electrons $\mathbf{r}$. The Hamiltonian ($\hat{H}$) describes all the relevant interactions between individual molecules in the surface.

In practice, Eq. 2.1 cannot be evaluated without further approximations in the context of molecular beam simulations, due to the large amount of computational effort required. In particular, it is often assumed that the quantum state $|\Psi\left(\mathbf{R}, \mathbf{r}, t\right)\rangle$ can be written as a product of the electronic (φ) and nuclear (ϕ) states together with the electronic ($\hat{H}_e$) and nuclear ($\hat{H}_N$) Hamiltonian according to

$$\hat{H}\left|\Psi\left(\mathbf{R}, \mathbf{r}, t\right)\right\rangle \approx \left(\hat{H}_N + \hat{H}_e\right)|\phi\rangle\,|\varphi\rangle, \tag{2.2}$$

within the Born-Oppenheimer approximation (BOA). The electronic system can then be solved first and separately by taking the electronic Hamiltonian

$$\hat{H}_e = \underbrace{\sum_{n=1}^{N_e}\frac{-\nabla_{\mathbf{r}_n}^2}{2}}_{\hat{T}_e} + \underbrace{\frac{1}{2}\sum_{m\neq n}^{N_e}\frac{1}{|\mathbf{r}_m - \mathbf{r}_n|}}_{\hat{V}_{ee}} - \underbrace{\sum_{n=1}^{N_e}\sum_{N=1}^{N_N}\frac{Z_N}{|\mathbf{R}_N - \mathbf{r}_n|}}_{\hat{V}_{Ne}} \tag{2.3}$$

where $\hat{T}_e$ is the kinetic energy of the electrons $\hat{T}_e$, the electron-electron interaction $\hat{V}_{ee}$ and the nuclear-electron interaction $\hat{V}_{Ne}$. The Schrödinger equation for the electronic system is then solved at a specific, i.e. depending parametrically on, nuclear configuration $\mathbf{R}$ according to

$$\hat{H}_e\left|\varphi\left(\mathbf{r}, \mathbf{R}\right)\right\rangle = V_e\left(R\right)\left|\varphi\left(\mathbf{r}, \mathbf{R}\right)\right\rangle, \tag{2.4}$$

where the eigenvalue $V_e(\mathbf{R})$ can then be interpreted as the energy of the electronic subsystem given the nuclear coordinates $\mathbf{R}$. Within the scope of this work Eq. 2.4 is used to solve for the electronic ground-state.

It is then possible to solve Eq. 2.2 for the nuclear system according to

$$\left(\hat{H}_N + \hat{V}_e\right)|\phi\rangle = V(R)|\phi\rangle, \tag{2.5}$$

since within the BOA the nuclear dynamics are completely defined by the ground state potential energy surface $V_e + V_{NN}$. The BOA is often justified because the coupling between the electronic and nuclear system, which is neglected here, has a magnitude of the ratio of the electron and nuclear masses, which is smaller than 10^{-3}. For molecules interacting with metal surfaces, this approximation is severely challenged: while the coupling for each state i is small due to the mass ratio, there is a large amount of states available for coupling at zero energetic cost due to the lack of a band gap. In fact, there are several (molecular and atomic beam) experiments that demonstrate the failure of the BOA [1, 2].

The following sections will describe how the potential energy is obtained and how the nuclear dynamics are calculated in this work. The potential energy (Sec. 2.2) is found by approximating the ground state electronic Hamiltonian using DFT and obtaining the concomitant ground-state energies. Nuclear dynamics as described by Eq. 2.5 are solved approximately using the method of quasi-classical (QC) dynamics (Sec. 2.3). Finally, the foundations of electronic friction theory are presented in Sec. 2.4, which allows to reintroduce effects beyond the BOA in a computationally affordable manner for molecules moving near metal surfaces. Based on these methods, observables have been computed that are accessible in molecular beam experiments. These results either stand as predictions, or can be compared with existing experimental data as a means of validating the underlying theoretical methodology and approximations.

2.2 Potential Energy

Given the computational demand for performing electronic structure calculations of even small molecules interacting with *metal* surfaces and the large amount of such

calculations needed for dynamics calculations, density functional theory (DFT) is currently the best compromise between accuracy and computational cost for the treatment of the electronic structure.

2.2.1 Density Functional Theory

The first Hohenberg-Kohn theorem states that there is a one-to-one mapping between the electronic wave function (φ), the electron density (ρ) and the so-called external potential (V_{ext}) which includes all external influences on the electronic system [3]. In the context of this work the external potential is given by the nuclear-electron interaction $\hat{V}_{Ne}$ (Eq. 2.3) since no other fields that may perturb the electronic system (e.g. external electric or magnetic fields) are considered.

Since the total energy (E) of the system can be defined by the functional $E[\varphi]$, it can also be defined by ρ or V_{ext} using

$$E[\varphi] \Leftrightarrow E[\rho] \Leftrightarrow E[V_{ext}]. \tag{2.6}$$

The functional defining the energy using ρ can be written as a sum of two contributions: the interaction of the electron density with the external potential ($V_{ext}[\rho]$) and the Hohenberg-Kohn functional ($F_{HK}[\rho]$) describing all other interactions according to

$$E[\rho] = V_{ext}[\rho] + F_{HK}[\rho]. \tag{2.7}$$

In the second Hohenberg-Kohn theorem, also known as the Hohenberg-Kohn variational principle, the ground state electron density ρ_0 is proven to minimize the total energy functional

$$E_0 := E[\rho_0] \leq E[\rho], \forall \rho \neq \rho_0. \tag{2.8}$$

The ground state can therefore be found by finding the stationary point using a functional derivative

$$\frac{\delta E[\rho]}{\delta \rho} = 0 \Rightarrow \rho_0. \tag{2.9}$$

Consequently, the ground state energy becomes a function of the nuclear coordinates according to

$$E_0[V_{ext}(\mathbf{R})] = E_0(\mathbf{R}), \tag{2.10}$$

which is exactly the definition of the PES needed to perform dynamics.

Unfortunately, the Hohenberg-Kohn functional is not known. In order to construct a (first) approximation, Kohn and Sham [4] have split up the Hohenberg-Kohn functional into the electrostatic interaction of the electron density with itself and the kinetic energy of the electron density.

$$E[\rho] = V_{ext}[\rho] + F_{HK}[\rho] = \underbrace{V_{ext}[\rho] + J[\rho] + T_s[\rho]}_{\text{exact}} + V_{xc}[\rho]. \tag{2.11}$$

The electrostatic interaction is approximated by the classical coulomb interactions of the electron density

$$J[\rho] = \frac{1}{2} \int d\mathbf{r}d\mathbf{r}' \frac{\rho(\mathbf{r})\rho(\mathbf{r}')}{|\mathbf{r} - \mathbf{r}'|}. \tag{2.12}$$

In order to evaluate the kinetic energy, Kohn and Sham have reintroduced orbitals, denoted here as Kohn-Sham orbitals φ_i^{KS}, that represent a fictitious system of n non-interacting electrons with the same density as a system of interacting electrons. The density is given in terms of the Kohn-Sham orbitals as

$$\rho\left(\left\{\varphi_1^{\mathsf{KS}}..\varphi_n^{\mathsf{KS}}\right\}\right) = \sum_i \langle\varphi_i^{\mathsf{KS}}|\varphi_i^{\mathsf{KS}}\rangle. \tag{2.13}$$

The kinetic energy is then approximated by a quantum system with the same electron density, but where the electrons do not interact

$$T_s[\rho] = \sum_i \langle\varphi_i^{\mathsf{KS}}| \frac{-\nabla^2}{2} |\varphi_i^{\mathsf{KS}}\rangle. \tag{2.14}$$

A certain part of the electron-electron interaction is not correctly described by $J[\rho]$ and, likewise, $T_s[\rho]$ does not correctly describe the energy for interacting electrons. These contributions are collected in the exchange-correlation functional $V_{xc}[\rho]$, for which approximations are discussed below.

The Kohn-Sham equations are effective single particle Schrödinger equations that result from reexpressing the total density constrained Hohenberg-Kohn variational principle

$$\frac{\delta}{\delta\rho}\left(E[\rho] - \mu\left(\int d\mathbf{r}\rho(\mathbf{r}) - n\right)\right) = 0, \tag{2.15}$$

with Lagrangian multiplier μ, in terms of the Kohn-Sham orbitals according to

$$\left(\frac{-\nabla^2}{2} + v_{eff}\right) \varphi_i^{\mathsf{KS}} = \epsilon_i \varphi_i^{\mathsf{KS}}. \qquad (2.16)$$

Here v_{eff} is given by

$$v_{eff}(\mathbf{r}) = \underbrace{\int d\mathbf{r}' \frac{\rho(\mathbf{r}')}{|\mathbf{r} - \mathbf{r}'|}}_{v_{\mathsf{Coul}}} + \underbrace{\frac{\delta V_{Ne}[\rho]}{\delta\rho(\mathbf{r})}}_{v_{\mathsf{ext}}} + \underbrace{\frac{\delta V_{xc}[\rho]}{\delta\rho(\mathbf{r})}}_{v_{\mathsf{XC}}}, \qquad (2.17)$$

with v_{ext} being the one-electron external potential. Solving Eqs. 2.11 and 2.16 self-consistently from an initial guess of the Kohn-Sham orbitals then yields the single particle energies ϵ_i and the total energy is given by

$$E[\rho] = \sum_i \epsilon_i - J[\rho] + V_{xc}[\rho] - \int d\mathbf{r} v_{xc}[\rho](\mathbf{r}). \qquad (2.18)$$

There are several classes of approximations for the exchange-correlation functionals. In the local density approximation (LDA) the exchange-correlation functional is designed to reproduce the homogeneous electron gas (HEG)

$$V[\rho] = \int d\mathbf{r}\rho(\mathbf{r})v_{xc}^{\mathrm{HEG}}(\rho(\mathbf{r})), \qquad (2.19)$$

and is based on local evaluations of the density only. The generalised gradient approximation (GGA) the gradient of the electron density is also evaluated as a first order approximation to non-local effects,

$$V[\rho] = \int d\mathbf{r}\rho(\mathbf{r})v_{xc}^{\mathrm{GGA}}(\rho(\mathbf{r}), \nabla_{\mathbf{r}}\rho(\mathbf{r})), \qquad (2.20)$$

which for most applications is an improvement compared to the LDA. A further improvement to the accuracy is the meta-GGA which includes even more non-local effects. Including the higher order non-local contributions generally comes at an increased computational effort.

In this thesis functionals at the GGA level (mainly PBE [5, 6] and RPBE [7], depending on the system) constitute the main 'work horses' for the construction of PESs. In addition, the semi-empirically motivated SRP method [8] is used where a

new functional is created by taking the linear combination of two existing functionals A and B based on the parameter α

$$E[\rho] = V_{ext}[\rho] + J[\rho] + T_s[\rho] + \alpha V_{xc}^{\mathrm{A}}[\rho] + (1 - \alpha)V_{xc}^{\mathrm{B}}[\rho], \tag{2.21}$$

in such a way that an experimental observable is reproduced more accurately. Ideally, the (groundstate) PES given by this new functional is better approximated than by the underlying functionals.

2.2.2 Continuous Representations of the Potential Energy Surface

While DFT is in principle able to produce $V_e(\mathbf{R})$ needed to solve the nuclear Schrödinger equation 2.5, it is neccesary to obtain this potential for all configurations $\mathbf{R}$ of the nuclear system that are relevant for the dynamics in a simulation of a molecular beam experiment. One way to do this is to do *ab-initio* molecular dynamics (AIMD) by performing a DFT calculation every time $V_e(\mathbf{R})$ is needed for a specific configuration $\mathbf{R}$ during the dynamics. However, if one is interested in obtaining observables with statistical significance for rare events during dynamics, such as reactions for molecules with a very low reaction probability, this becomes too computationally demanding. Instead, continuous representations of the PES are used. Generally, a large data set of configurations with concomitant energies is generated which is consequently interpolated or fitted. When the resulting continuous representation is not of sufficient quality, a larger data set can be obtained, or a different strategy can be used. For diatomic molecules, the coordinates $\mathbf{R}$ can be conveniently described w.r.t. a surface atom in the first layer as two single atom Cartesian coordinates $\mathbf{R}_A$ and $\mathbf{R}_B$, or using the molecular coordinate system where the center of mass (COM) (equivalent to the geometric centre for homonuclear molecules) X, Y and Z coordinates are used together with the bond distance r, polar angle θ, and azimuthal angle ϕ (see Fig. 2.1). Three different methods have been used in this thesis to obtain continuous representations of PESs. First the corrugation reducing procedure (CRP) in combination with an interpolation using symmetry adapted basis functions is used for H_2 interacting with (an ideal 0K) Cu(111) surface (Chap. 3). This method only allows for 6 degrees of freedom of the
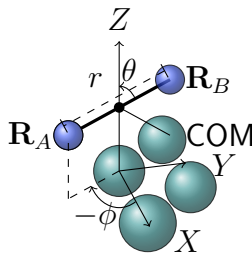
Figure 2.1: Six-dimensional coordinate system for the description of diatomic molecules (atoms in blue) on metal surfaces (atoms in green), consisting of the center of mass (COM) coordinates (X,Y,Z) and the bond distance r as well as the polar angle θ and azimuthal angle ϕ. X,Y,Z = 0 corresponds to the position of a surface layer atom in the surface plane (top site).

molecule while the motion and displacements of the metal is neglected. Secondly, the SCM model (Chap. 3) allows to introduce the effect of surface atom displacements. This effect is introduced within a so-called sudden approximation and realised as a perturbation to the 6D CRP PES. Such a treatment precludes energy exchange with the phonons of the surface. Finally, to also include the effect of surface motion, NN fits (Chap. 5) have been used to model all degrees of freedom of the nuclear system.

Corrugation Reducing Procedure

Within the CRP, the PES is represented by

$$V_{CRP}(\mathbf{R}) = V_{3D}(\mathbf{R}_A) + V_{3D}(\mathbf{R}_B) + I_{6D}(\mathbf{R}), \qquad (2.22)$$

as sum of two 3D potentials (V_{3D}), which describe the interaction of two independent atoms A and B with the metal surface, and a 6D interpolation function (I_{6D}), which describes the molecular contribution of the system. Here $\mathbf{R} = (\mathbf{R}_A, \mathbf{R}_B)$ represents the coordinate vector composed of both individual atom coordinate vectors $\mathbf{R}_A$ and $\mathbf{R}_B$. Much of the corrugation is then already contained in the 3D potentials and the rest

term is then more easily interpolated. The 3D potential

$$V_{3D}(\mathbf{R}_x) = \sum_i^N V_{1D,ref}(|\mathbf{R}_x - \mathbf{S}_i|) + I_{3D}(\mathbf{R}_x), x \in \{A, B\} \qquad (2.23)$$

consists of the sum of two-body interactions ($V_{1D,ref}$) with the N closest surface atoms, described by the vectors $\mathbf{S}_i$ together with a 3D interpolation function (I_{3D}). Surface symmetry (C_{3v}) and periodicity can be fully taken into account using the CRP. The 3D and 6D interpolation functions are based on symmetry adapted basis functions defined using the Grand Orthogonality Theorem. For the 6D interpolation function a spline interpolation is made for several 2D PES cuts in the r-Z plane at several surface sites (X,Y) and molecular orientations (ϕ,θ). The symmetry adapted basis functions are then used to interpolate between the different r-Z cuts. Because the error of the CRP interpolation is generally much smaller than that of the underlying DFT, it is considered appropriate to use the CRP to represent the 6D PES.

Static Corrugation Model

The effect of surface atom displacements can be taken into account by treating the displacements as perturbations to the ideal lattice using the SCM, which has originally been developed by Wijzenbroek and Somers [9] Chap. 3 describes the model in detail, together with the further development and improvments that are introduced as part of this thesis [10].

Neural Networks

For the reactive scattering of N_2 on Ru(0001) a significant amount of energy exchange with the phonons of the surface has been found. Consequently, a significant influence of surface motion on the dissociative chemisorption probability was also observed [11, 12]. Thus both the CRP and SCM are not suitable for this system. Instead a continuous representation of the PES including surface atom motion has been obtained using a high-dimensional NN [12]. In order for the NN to predict energies with the correct symmetry, the Behler-Parrinello method has been used [13, 14]. This method uses radial and angular symmetry functions to describe the chemical environment for each

atom in the system. The total PES is decomposed into individual atomic contributions, where differently optimized NN-parameters are used for different atom types. The resulting single atom energies are added together, ensuring the correct symmetry. In Chap. 6 more details on NN topologies are provided. Although the focus there is not on PESs, this details also apply for NN-based PES representation.

2.3   Quasi-Classical Molecular Dynamics

Using any of the previously discussed continuous PES representations(CRP plus SCM or NN), it is possible to describe the dissociative chemisorption and rovibrational (in)elastic scattering of diatomic molecules on metal surfaces. The PES itself is not a directly measurable quantity, but it is possible to do molecular dynamics simulations with the PES to compute observables. In this thesis, dynamics simulations were performed of H_2 and N_2 molecules coming from the gas phase towards a Cu(111) and Ru(0001) surface respectively, in a collision event. The dynamics were performed using the method of QC dynamics [8, 11, 15].

A dynamics calculation is performed by first determining the initial configuration for the molecule and in the case of a non-zero surface temperature also determining the initial displacements of surface atoms from their equilibrium positions. Initial conditions are determined using a Monte-Carlo sampling scheme, where zero point energy is taken into account for the initial configuration of the molecule. Then the system is propagated classically by solving Newton's equations of motion until certain stopping criteria are fulfilled and the resulting trajectory is then analysed. This process is repeated many (10^4 to 10^6) times - depending on the observable to be calculated - to get a good statistical average using the Monte-Carlo scheme. The details are discussed in the following sections.

2.3.1   Initial Conditions

The initial conditions are generated by first calculating the rovibrational energy levels of the diatomic molecule for their respective PES in the gas phase using the Fourier grid

Hamiltonian method [16]. To get the QC distribution for the atom-atom separation r of the molecule, the gasphase molecule was propagated for one complete phase in its vibration, after which the initial atomic positions and velocities were chosen using standard Monte Carlo methods such that the sampling is homogenous in time. The ϕ angle is chosen from an uniform random distribution in the range $[0, 2\pi]$ while θ is chosen from an uniform random distribution in the range $[0, \theta_L]$ where $\theta_L = \pi$ if J=0 and $cos(\theta_L) = \frac{m_J}{\sqrt{J(J+1)}}$ if J≥1. The angular velocities are chosen according to the quantized angular momentum $L^2 = J(J+1)\hbar^2$. The initial COM position is then shifted 9 Å in Z away from the surface (Z=9 Å) while the COM position along the surface is given by X = U + $\frac{1}{2}$V and Y = $\frac{1}{2}\sqrt{3}$V where U and V are chosen from an uniform random distribution in the range $[0, a]$ with a being the lattice constant. This process is identical to earlier work [8, 9, 15, 17, 18]. In the case of finite surface temperature, a detailed description of the surface atom displacement is given in Chap. 3.

2.3.2   Propagation

Once the initial conditions are defined, the system is propagated according to Hamilton's formulation of classical mechanics, i.e. based on the Hamiltionian

$$H = \frac{p_A^2(t)}{2m_A} + \frac{p_B^2(t)}{2m_B} + V(R(t)), \qquad (2.24)$$

where $p_A(t)$ and $p_B(t)$ are the momenta of atoms A and B respectively at time t and $V(R(t))$ is the potential energy at time t. The time propagation of simulations of H_2 have been performed using the predictor-corrector method of Bulirsch and Stoer [19]. Simulations with N_2 on the other hand have been propagated as detailed in Sec. 2.4. The propagation of a trajectory is stopped when either the maximum time limit has been reached (as detailed in the respective chapters), or the H (N) atoms are separated by more than 2.25Å (2.75Å), in which case the original corresponding diatomic is considered to have dissociated (i.e. reacted).

2.3.3 Analysis

After a trajectory has been stopped, it is analysed to determine the outcome.

Reaction Probability

The reaction probability is defined as the number of trajectories that result in a reaction, divided by the total number of trajectories and gives a measure of how likely it is for the reaction to take place under a certain set of initial conditions (e.g. molecular velocity distribution and/or rovibrational state, surface temperature).

Rovibrational Elastic and Inelastic Scattering

When an incoming trajectory is not reactive, it can either scatter back into the gasphase or get trapped on the surface. The incoming trajectories that turn out to scatter can be divided into two groups: either the molecule returns from the surface in the same rovibrational state, or it does not. Scattered molecules in the same rovibrational state are considered to have scattered elastically, while scattered molecules that are not in the same rovibrational state are considered to have scattered inelastically. In order to relate the outcome of a quasiclassical trajectory to a (discrete) rovibrational quantum state a binning procedure is necessary. That means that the final rovibrational energy has to be assigned to a rotational (J) and a vibrational (v) state. Generally the energy difference between rotational states is much smaller than vibrational states which means if the total rovibrational energy of two states is similar, we can easily distinguish by first binning to the rotational state and then to the vibrational state. The quantum rotational state J has a direct classical analogue according to

$$L^2 = J(J+1). \tag{2.25}$$

The rotational state of a molecule in the quasiclassical approximation can be described in a similar way as a quantum rotational state by first assigning a non-integer number for J. Next the value of J is rounded while taking into account selection rules. These selection rules preclude a transition of J before the collision with the surface to a J after the collision that is different by an odd number. This approach works because

L is well defined in classical dynamics. For a classical trajectory, the momenta of all atoms are known at all times. If there is no interaction between the surface and the diatomic molecule at the time of analysis, i.e. at sufficiently large molecular-surface distances, the angular momentum L of the diatomic is conserved and given by

$$L = |\overrightarrow{r} \times \overrightarrow{p}|, \tag{2.26}$$

where $\overrightarrow{r}$ is the distance vector from one atom to the other and $\overrightarrow{p} = \mu \dot{\overrightarrow{r}}$ is the momentum vector along the internal coordinates of the molecule with

$$\mu = \frac{m_A m_B}{m_A + m_B}. \tag{2.27}$$

When the J state is assigned, the rovibrational energy of the scattered molecule (E_{rovib}) is determined by subtracting the COM kinetic energy ($E_{kin,COM}$) and the potential energy ($V(r)$) relative to the equilibrium potential energy ($V(r_0)$) from the total kinetic energy of the molecule according to

$$E_{rovib} = E_{kin} - E_{kin,COM} - (V(r_0) - V(r)). \tag{2.28}$$

The COM kinetic energy for a diatomic is defined by

$$E_{kin,COM} = \frac{(m_A + m_B)\left(\dot{X}^2 + \dot{Y}^2 + \dot{Z}^2\right)}{2}. \tag{2.29}$$

The rovibrational energy is then compared to the rovibrational eigenstates of the molecule that has the previously determined J state (according to Eqs. 2.25 and 2.26) and the candidate with the closest energy is selected.

2.4 Nuclear Dynamics Beyond the Born-Oppenheimer Approximation

With dynamics on a (single) PES, it is not possible to take into account the exchange of energy between the electronic and nuclear system due to electron-nuclear couplings that are neglected within the BOA. In order to reintroduce the effect of these couplings and

concomitant electron-hole pair excitations on the nuclear dynamics (while maintaining a classical description of the latter), electronic friction theory [20, 21] is used in this work. This work-horse theory for dynamics of molecules on metal surfaces, which can be considered as "weakly non-adiabatic", is based on a generalized Langevin equation (GLE)

$$
m_i \frac{d^2 \{\mathbf{R}, \mathbf{S}\}_i}{dt} = -\nabla_i V(\mathbf{R}, \mathbf{S}) \ \ \underbrace{- \sum_j \eta_{ij}^{\mathsf{mol}}(\mathbf{R}) \frac{dR_j}{dt}}_{\text{dissipative}} + \underbrace{\mathcal{F}^{\mathsf{mol}}(\boldsymbol{\eta}, T_{\mathsf{s}})}_{\text{random}} \quad . \tag{2.30}
$$

This equation introduces two additional terms compared to Newtonian dynamics (see previous section): a dissipative term based on the electronic friction tensor η^{mol} and the velocities $\frac{d\mathbf{R}}{dt}$, and random forces $\mathcal{F}^{\mathsf{mol}}$ that depend on the surface temperature T_s and the friction tensor. The friction tensor is based on matrix elements that couple the electronic and nuclear system and the GLE thus goes beyond the Born-Oppenheimer Approximation. Motivated by previous work [22–25], in this thesis the focus has been on obtaining electronic friction coefficients for the diatomic molecule $\mathbf{R}$ but not for the surface atoms $\mathbf{S}$.

The non-adiabatic energy loss, i.e. energy that is dissipated into electron-hole pairs at time t starting from time t_0, in the absence of random forces, is given by

$$
E_{\mathsf{diss}}(t) = \int_{t'=t_0}^{t} dt' \dot{R}_i(t') \eta_{ij}(\mathbf{R}(t')) \dot{R}_j(t'). \tag{2.31}
$$

All dynamical calculations for H_2 on Cu(111) including electronic friction make use of the static surface approximation ($T_s = 0$ K), for which the stochastic term ($\mathcal{F}^{\mathsf{mol}}$) vanishes (see also Chap. 4). The calculations for N_2 on Ru(0001) on the other hand have been performed for a surface temperature $T_S = 575$ K. In order to do so, the "OVRVO" algorithm of Sivak, Chodera, and Crooks [26] has been adapted (see Chap. 5). This algorithm is a split-operator method where first half a time step of friction and random force is propagated using the Ornstein–Uhlenbeck (O) method [27], then half a time step of the deterministic velocity (V) is updated, next a full time step of the deterministic position (R) is updated and finally half a time step of V and then O are updated. When no friction is present, this algorithm simplifies to the velocity-Verlet algorithm.

Already in 1975 have Suhl and coworkers [20] derived an expression for the electronic
friction tensor (here expressed for spin-unpolarized systems)

$$\eta_{ij}^{\mathsf{mol}} = 2\pi \sum_{m,n} \langle \psi_m | \, \hat{F}_i \, | \psi_n \rangle \, \langle \psi_n | \, \hat{F}_j \, | \psi_m \rangle \times \delta \left(\epsilon_{\mathsf{F}} - \epsilon_m \right) \delta \left(\epsilon_{\mathsf{F}} - \epsilon_n \right). \qquad (2.32)$$

Their derivation is based on a "bootstrap" method to compare the friction tensor $\boldsymbol{\eta}^{\mathsf{fric}}$
based on the Fokker-Planck equation with rigorous formulas using the full Hamiltonian
of the system. Here $\hat{F}_{i,j}$ describes the response of a perturbation to the electronic
system of the adsorbate-surface system within a single-particle picture with states
ψ_n, ψ_m and concomitant energies ϵ_n, ϵ_m. The perturbation results from the motion
along adsorbate coordinates R_i and R_j in the limit of slow adsorbate motion (quasi-
static limit) and small electronic temperatures corresponding to energy equivalents
that are small relative to the Fermi energy ϵ_{F} of the metal.

Subotnik and coworkers [28–31] have shown that there is only one "universal" elec-
tronic friction tensor, which is the temperature dependent version of Eq. 2.32. Other
formulations of electronic friction then are either equivalent or contain further approx-
imations.

In this thesis I have used two methods to calculate electronic friction coefficients
(i.e. elements of the friction tensor): i) the Local-Density Friction Approximation
(LDFA) [25, 32] where the friction tensor of an atom in jelium is computed and ii) the
orbital-dependent friction (ODF) [20, 21, 33–36] where the friction tensor is obtaind
from density functional perturbation theory (density functional perturbation theory
(DFPT)). Detailed derivations of both LDFA and ODF can be found elsewhere [20,
28, 29]. Brief summaries of these derivations are presented in the remainder of this
section since some of the underlying approximations are important for comparing the
LDFA and ODF results as is done later in this thesis.

2.4.1 Local Density Friction Approximation

Within the LDFA Eq. 2.32 is used to evaluate the electronic friction tensor of a model
system, namely an atom (moving) in a homogeneous electron gas (jellium) with a
given density ρ_e. In this case the matrix elements $\langle \psi_m | \, \hat{F}_i \, | \psi_n \rangle$ can be conveniently

obtained by considering the scattering of the electronic continuum from the nucleus of the atom embedded therein. Assuming spherical symmetry, the scattering problem becomes (effectively) one dimensional, and the aforementioned matrix elements can be obtained from the scattering phase shifts of partial (spherical) waves belonging to different angular momentum channels l. As a result of the spherical Hamiltonian assumption, the friction tensor becomes diagonal in Cartesian coordinates and the elements are the same in every direction for the same atom and jelium, resulting in a single friction coefficient per atom.

$$\eta^{\text{AiJ}}\left(\rho_e\right) = \rho_e \frac{8}{3\pi} \epsilon_{\text{F}} \sum_l \left(l+1\right) \sin^2\left(\delta_l - \delta_{l+1}\right). \tag{2.33}$$

Juaristi and coworkers [24] have suggested to use these friction coefficients for simulations of molecular beam experiments on metal surfaces. Diatomic molecules are treated within an independent atom approximation. That means that the friction coefficient for each individual atom is taken as the friction of that atom in a jelium with an electron density ρ_e equal to that of the electron density of a clean metal surface, at the position of the atom $\mathbf{R}_A$:

$$\eta^{\text{LDFA}}\left(\mathbf{R}_A\right) = \eta^{\text{AiJ}}\left(\rho_e^{\text{clean surface}}\left(\mathbf{R}_A\right)\right). \tag{2.34}$$

The friction coefficient for a specific atom is then computed for several electron densities and a simple analytical fit is made to map the density to the friction coefficient. These friction coefficients can easily be fitted in 3D, e.g. by using machine learning techniques (NNs).

2.4.2 Orbital-Dependent Friction

Within a Kohn-Sham (KS) time-dependent DFT picture, an expression corresponding to Eq. 2.32 for the electronic friction tnesor has been obtained by various authors [21, 33, 35, 37, 38]. Unlike for LDFA, the matrix elements of this "orbital-dependent" friction (ODF) tensor are based on the KS orbitals of atoms and molecules on an actual metal surface and the changes of the KS effective potential due to motion

$$\eta_{ij}^{\text{ODF}} = 2\pi \sum_{m,n} \langle \psi_m^{\text{KS}} | \frac{\partial v_{\text{eff}}^{\text{KS}}}{\partial R_i} | \psi_n^{\text{KS}} \rangle \langle \psi_n^{\text{KS}} | \frac{\partial v_{\text{eff}}^{\text{KS}}}{\partial R_j}^* | \psi_m^{\text{KS}} \rangle \delta\left(\epsilon_n^{\text{KS}} - \epsilon_{\text{F}}\right) \delta\left(\epsilon_m^{\text{KS}} - \epsilon_{\text{F}}\right). \tag{2.35}$$

These so-called electron-phonon matrix elements $\langle \psi_n^{\mathsf{KS}} | \frac{\partial v_{\mathsf{eff}}^{\mathsf{KS}}}{\partial R_i} | \psi_m^{\mathsf{KS}} \rangle$ can be conveniently obtained from DFPT. Within DFPT, the Kohn-Sham equations are rewritten in a derivative form, where a change in the position of nuclear coordinates is considered. The Kohn-Sham equations now become

$$\left(\frac{-\nabla^2}{2} + v_{\mathsf{eff}}^{\mathsf{KS}} - \epsilon_m^{\mathsf{KS}} \right) | \Delta_i \varphi_m^{\mathsf{KS}} \rangle = - \left(\Delta_i v_{\mathsf{eff}}^{\mathsf{KS}} - \Delta_i \epsilon_m^{\mathsf{KS}} \right) | \varphi_m^{\mathsf{KS}} \rangle, \qquad (2.36)$$

where $\Delta_i = \frac{\partial}{\partial R_i}$ denotes the potential derivative with respect to nuclear displacement R_i. Eq. 2.36 leaves some room for interpretation on how to sum over the states n and m, especially when considering a periodic system where also a k-point index is introduced. Throughout this thesis, the method of Trail, Graham, and Bird [39] for an overlayer of adsorbates on a metal surface is used when performing this summation. Both the perturbation of the external potential $\Delta_i v_{\mathsf{ext}}$ and an induced perturbation due to the response of the system are included in the change of the effective potential according to

$$\Delta_i v_{\mathsf{eff}}^{\mathsf{KS}} = \underbrace{\Delta_i v_{\mathsf{ext}}}_{\text{perturbation}} + \underbrace{\int d\mathbf{r}' \frac{\Delta_i \rho \left(\mathbf{r}'\right)}{|\mathbf{r} - \mathbf{r}'|} + \left. \frac{\delta v_{\mathsf{XC}} \left(\rho\right)}{\delta \rho} \right|_{\rho = \rho(\mathbf{r})} \Delta \rho \left(\mathbf{r}\right)}_{\text{induced}}. \qquad (2.37)$$

The perturbed quantities $\Delta_i \epsilon_m^{\mathsf{KS}}$, $\Delta_i \varphi_m^{\mathsf{KS}}$ and $\Delta_i \rho$ are found by

$$\Delta_i \epsilon_m^{\mathsf{KS}} = \langle \varphi_m^{\mathsf{KS}} | \Delta_i v_{\mathsf{eff}}^{\mathsf{KS}} | \varphi_m^{\mathsf{KS}} \rangle, \qquad (2.38)$$

$$\Delta_i \varphi_m^{\mathsf{KS}} = \sum_{n \neq m} \varphi_n^{\mathsf{KS}} \frac{\langle \varphi_n^{\mathsf{KS}} | \Delta_i v_{\mathsf{eff}}^{\mathsf{KS}} | \varphi_m^{\mathsf{KS}} \rangle}{\epsilon_m^{\mathsf{KS}} - \epsilon_n^{\mathsf{KS}}}, \qquad (2.39)$$

and

$$\Delta_i \rho = 4 \sum_{m=1}^{N/2} \sum_{n \neq m} \varphi_m^{\mathsf{KS}*} \varphi_n^{\mathsf{KS}} \frac{\langle \varphi_n^{\mathsf{KS}} | \Delta_i v_{\mathsf{eff}}^{\mathsf{KS}} | \varphi_m^{\mathsf{KS}} \rangle}{\epsilon_m^{\mathsf{KS}} - \epsilon_n^{\mathsf{KS}}} \qquad (2.40)$$

respectively. Solving Eqs. 2.36 through 2.40 self-consistently (as nowadays implemented in many standard DFT packages) yields the neccesary electron-phonon matrix elements.

From a computational point of view, it is important to note that the δ-functions in the 'sum over states' (Eq. 2.35) cannot be analytically eliminated - unlike in the (final) expression for for η^{LDFA} (Eq. 2.33). For a summation over a finite set of states, which

are not all located at the Fermi surface (for practical reasons), the δ-functions thus are broadened, i.e., usually substituted by Gaussians with a finite width [34–36, 40–44]. This approximation has been criticized by Novko and coworkers [45] and might in the future be overcome by a new technique, which has been suggested only very recently by Jin and Subotnik [46].

A continuous representation of η_{ij}^{ODF} that accounts for symmetries of the adsorbate-surface system is by far not as easy to obtain as $\eta_{ij}^{\mathsf{LDFA}}$. The representations used in Chap. 4 and Chap. 5 have been developed as part of this thesis, and the underlying methodology is described in detail in Chap. 6.

References

[1] A. M. Wodtke. "Electronically Non-Adiabatic Influences in Surface Chemistry and Dynamics". In: *Chem. Soc. Rev.* 45 (2016), pp. 3641–3657. DOI: `10.1039/C6CS00078A`.

[2] A. M. Wodtke, J. C. Tully, and D. J. Auerbach. "Electronically Non-Adiabatic Interactions of Molecules at Metal Surfaces: Can We Trust the Born-Oppenheimer Approximation for Surface Chemistry?" In: *Int. Rev. Phys. Chem.* 23.4 (2004), pp. 513–539.

[3] P. Hohenberg and W. Kohn. "Inhomogeneous Electron Gas". In: *Phys. Rev.* 136 (1964), B864–B871. DOI: `10.1103/PhysRev.136.B864`.

[4] W. Kohn and L. J. Sham. "Self-Consistent Equations Including Exchange and Correlation Effects". In: *Phys. Rev.* 140 (1965), A1133–A1138. DOI: `10.1103/PhysRev.140.A1133`.

[5] J. P. Perdew, K. Burke, and Y. Wang. "Generalized Gradient Approximation for the Exchange-Correlation Hole of a Many-Electron System". In: *Phys. Rev. B* 54 (1996), pp. 16533–16539. DOI: `10.1103/PhysRevB.54.16533`.

[6] J. P. Perdew, K. Burke, and M. Ernzerhof. "Erratum: Generalized Gradient Approximation Made Simple [Phys. Rev. Lett. 77, 3865 (1996)]". In: *Phys. Rev. Lett.* 78 (1997), pp. 1396–1396. DOI: `10.1103/PhysRevLett.78.1396`.

[7] B. Hammer, L. B. Hansen, and J. K. Nørskov. "Improved Adsorption Energetics within Density-Functional Theory Using Revised Perdew-Burke-Ernzerhof Functionals". In: *Phys. Rev. B* 59 (1999), pp. 7413–7421. DOI: `10.1103/PhysRevB.59.7413`.

[8]   C. Díaz, E. Pijper, R. A. Olsen, H. F. Busnengo, D. J. Auerbach, et al. "Chemically Accurate Simulation of a Prototypical Surface Reaction: H2 Dissociation on Cu(111)". In: *Science* 326 (2009), pp. 832–834. DOI: 10.1126/science.1178722.

[9]   M. Wijzenbroek and M. F. Somers. "Static Surface Temperature Effects on the Dissociation of H2 and D2 on Cu(111)". In: *J. Chem. Phys.* 137 (2012), p. 054703. DOI: 10.1063/1.4738956.

[10] P. Spiering, M. Wijzenbroek, and M. F. Somers. "An Improved Static Corrugation Model". In: *J. Chem. Phys.* 149 (2018), p. 234702. DOI: 10.1063/1.5058271.

[11] K. Shakouri, J. Behler, J. Meyer, and G.-J. Kroes. "Analysis of Energy Dissipation Channels in a Benchmark System of Activated Dissociation: N2 on Ru(0001)". In: *J. Phys. Chem. C* 122 (2018), pp. 23470–23480. DOI: 10.1021/acs.jpcc.8b06729.

[12] K. Shakouri, J. Behler, J. Meyer, and G.-J. Kroes. "Accurate Neural Network Description of Surface Phonons in Reactive Gas–Surface Dynamics: N_2 + Ru(0001)". In: *J. Phys. Chem. Lett.* 8 (2017), pp. 2131–2136. DOI: 10.1021/acs.jpclett.7b00784.

[13] J. Behler, S. Lorenz, and K. Reuter. "Representing Molecule-Surface Interactions with Symmetry-Adapted Neural Networks". In: *J. Chem. Phys.* 127 (2007), p. 014705. DOI: 10.1063/1.2746232.

[14] J. Behler and M. Parrinello. "Generalized Neural-Network Representation of High-Dimensional Potential-Energy Surfaces". In: *Phys. Rev. Lett.* 98 (2007), p. 146401. DOI: 10.1103/PhysRevLett.98.146401.

[15] C. Diaz, R. A. Olsen, H. F. Busnengo, and G.-J. Kroes. "Dynamics on Six-Dimensional Potential Energy Surfaces for H2/Cu(111): Corrugation Reducing Procedure versus Modified Shepard Interpolation Method and PW91 versus RPBE". In: *J. Phys. Chem. C* 114 (2010), pp. 11192–11201. DOI: 10.1021/jp1027096.

[16] C. C. Marston and G. G. Balint-Kurti. "The Fourier Grid Hamiltonian Method for Bound State Eigenvalues and Eigenfunctions". In: *J. Chem. Phys.* 91 (1989), pp. 3571–3576. DOI: 10.1063/1.456888.

[17] A. Mondal, M. Wijzenbroek, M. Bonfanti, C. Díaz, and G.-J. Kroes. "Thermal Lattice Expansion Effect on Reactive Scattering of H2 from Cu(111) at Ts = 925 K". In: *J. Phys. Chem. A* 117 (2013), pp. 8770–8781. DOI: 10.1021/jp4042183.

[18] F. Nattino, A. Genova, M. Guijt, A. S. Muzas, C. Díaz, et al. "Dissociation and Recombination of D_2 on Cu(111): Ab Initio Molecular Dynamics Calculations and Improved Analysis of Desorption Experiments". In: *J. Chem. Phys.* 141 (2014), p. 124705. DOI: 10.1063/1.4896058.

2

[19]   J. Stoer and R. Bulirsch. *Introduction to Numerical Analysis*. New York: Springer-Verlag, 1980.

[20]   E. G. d'Agliano, P. Kumar, W. Schaich, and H. Suhl. "Brownian Motion Model of the Interactions between Chemical Species and Metallic Electrons: Bootstrap Derivation and Parameter Evaluation". In: *Phys. Rev. B* 11 (1975), pp. 2122–2143. DOI: 10.1103/PhysRevB.11.2122.

[21]   M. Head-Gordon and J. C. Tully. "Molecular Dynamics with Electronic Frictions". In: *J Chem Phys* 103 (1995), pp. 10137–10145. DOI: 10.1063/1.469915.

[22]   D. Novko, M. Blanco-Rey, M. Alducin, and J. I. Juaristi. "Surface Electron Density Models for Accurate *Ab Initio* Molecular Dynamics with Electronic Friction". In: *Phys. Rev. B* 93 (2016), p. 245435. DOI: 10.1103/PhysRevB.93.245435.

[23]   A. C. Luntz, I. Makkonen, M. Persson, S. Holloway, D. M. Bird, et al. "Comment on "Role of Electron-Hole Pair Excitations in the Dissociative Adsorption of Diatomic Molecules on Metal Surfaces"". In: *Phys. Rev. Lett.* 102 (2009), p. 109601. DOI: 10.1103/PhysRevLett.102.109601.

[24]   J. I. Juaristi, M. Alducin, R. D. Muiño, H. F. Busnengo, and A. Salin. "Juaristi et al. Reply:" in: *Phys. Rev. Lett.* 102 (2009), p. 109602. DOI: 10.1103/PhysRevLett.102.109602.

[25]   J. I. Juaristi, M. Alducin, R. D. Muiño, H. F. Busnengo, and A. Salin. "Role of Electron-Hole Pair Excitations in the Dissociative Adsorption of Diatomic Molecules on Metal Surfaces". In: *Phys. Rev. Lett.* 100 (2008), p. 116102. DOI: 10.1103/PhysRevLett.100.116102.

[26]   D. A. Sivak, J. D. Chodera, and G. E. Crooks. "Time Step Rescaling Recovers Continuous-Time Dynamical Properties for Discrete-Time Langevin Integration of Nonequilibrium Systems". In: *J. Phys. Chem. B* 118 (2014), pp. 6466–6474. DOI: 10.1021/jp411770f.

[27]   G. E. Uhlenbeck and L. S. Ornstein. "On the Theory of the Brownian Motion". In: *Phys. Rev.* 36 (1930), pp. 823–841. DOI: 10.1103/PhysRev.36.823.

[28]   W. Dou and J. E. Subotnik. "Perspective: How to Understand Electronic Friction". In: *J. Chem. Phys.* 148 (2018), p. 230901. DOI: 10.1063/1.5035412.

[29]   W. Dou, G. Miao, and J. E. Subotnik. "Born-Oppenheimer Dynamics, Electronic Friction, and the Inclusion of Electron-Electron Interactions". In: *Phys. Rev. Lett.* 119 (2017), p. 046001. DOI: 10.1103/PhysRevLett.119.046001.

[30]   W. Dou and J. E. Subotnik. "Universality of Electronic Friction: Equivalence of von Oppen's Nonequilibrium Green's Function Approach and the Head-Gordon–Tully Model at Equilibrium". In: *Phys. Rev. B* 96 (2017), p. 104305. DOI: 10.1103/PhysRevB.96.104305.

[31] W. Dou and J. E. Subotnik. "Universality of Electronic Friction. II. Equivalence of the Quantum-Classical Liouville Equation Approach with von Oppen's Nonequilibrium Green's Function Methods out of Equilibrium". In: *Phys. Rev. B* 97 (2018), p. 064303. DOI: 10.1103/PhysRevB.97.064303.

[32] M. J. Puska and R. M. Nieminen. "Atoms Embedded in an Electron Gas: Phase Shifts and Cross Sections". In: *Phys. Rev. B* 27 (1983), p. 6121. DOI: 10.1103/PhysRevB.27.6121.

[33] B. Hellsing and M. Persson. "Electronic Damping of Atomic and Molecular Vibrations at Metal Surfaces". In: *Phys Scr* 29 (1984), p. 360. DOI: 10.1088/0031-8949/29/4/014.

[34] M. Askerka, R. J. Maurer, V. S. Batista, and J. C. Tully. "Role of Tensorial Electronic Friction in Energy Transfer at Metal Surfaces". In: *Phys. Rev. Lett.* 116 (2016), p. 217601. DOI: 10.1103/PhysRevLett.116.217601.

[35] R. J. Maurer, M. Askerka, V. S. Batista, and J. C. Tully. "Ab Initio Tensorial Electronic Friction for Molecules on Metal Surfaces: Nonadiabatic Vibrational Relaxation". In: *Phys. Rev. B* 94 (2016), p. 115432. DOI: 10.1103/PhysRevB.94.115432.

[36] M. Askerka, R. J. Maurer, V. S. Batista, and J. C. Tully. "Erratum: Role of Tensorial Electronic Friction in Energy Transfer at Metal Surfaces [Phys. Rev. Lett. 116, 217601 (2016)]". In: *Phys. Rev. Lett.* 119 (2017), p. 069901. DOI: 10.1103/PhysRevLett.119.069901.

[37] M. S. Mizielinski, D. M. Bird, M. Persson, and S. Holloway. "Electronic Nonadiabatic Effects in the Adsorption of Hydrogen Atoms on Metals". In: *J. Chem. Phys.* 122 (2005), p. 084710. DOI: 10.1063/1.1854623.

[38] J. R. Trail, M. C. Graham, and D. M. Bird. "Electronic Damping of Molecular Motion at Metal Surfaces". In: *Computer Physics Communications* 137 (2001), pp. 163–173. DOI: 10.1016/S0010-4655(01)00177-1.

[39] J. R. Trail, M. C. Graham, and D. M. Bird. "Electronic Damping of Molecular Motion at Metal Surfaces". In: *Computer Physics Communications* 137 (2001), pp. 163–173. DOI: 10.1016/S0010-4655(01)00177-1.

[40] R. J. Maurer, B. Jiang, H. Guo, and J. C. Tully. "Mode Specific Electronic Friction in Dissociative Chemisorption on Metal Surfaces: H_2 on Ag(111)". In: *Phys. Rev. Lett.* 118 (2017), p. 256001. DOI: 10.1103/PhysRevLett.118.256001. arXiv: 1705.09753 [cond-mat.mtrl-sci].

[41] Y. Zhang, R. J. Maurer, H. Guo, and B. Jiang. "Hot-Electron Effects during Reactive Scattering of H_2 from Ag(111): The Interplay between Mode-Specific Electronic Friction and the Potential Energy Landscape". In: *Chem. Sci.* 10 (2019), pp. 1089–1097. DOI: 10.1039/C8SC03955K.

2

[42]   R. J. Maurer, Y. Zhang, H. Guo, and B. Jiang. "Hot Electron Effects during Reactive Scattering of H_2 from Ag(111): Assessing the Sensitivity to Initial Conditions, Coupling Magnitude, and Electronic Temperature". In: *Faraday Discuss.* 214 (2019), pp. 105–121. DOI: 10.1039/C8FD00140E.

[43]   P. Spiering and J. Meyer. "Testing Electronic Friction Models: Vibrational De-Excitation in Scattering of H_2 and D_2 from Cu(111)". In: *J. Phys. Chem. Lett.* 9 (2018), pp. 1803–1808. DOI: 10.1021/acs.jpclett.7b03182.

[44]   P. Spiering, K. Shakouri, J. Behler, G.-J. Kroes, and J. Meyer. "Orbital-Dependent Electronic Friction Significantly Affects the Description of Reactive Scattering of N_2 from Ru(0001)". In: *J. Phys. Chem. Lett.* 10 (2019), pp. 2957–2962. DOI: 10.1021/acs.jpclett.9b00523.

[45]   D. Novko, M. Alducin, and J. I. Juaristi. "Electron-Mediated Phonon-Phonon Coupling Drives the Vibrational Relaxation of CO on Cu(100)". In: *Phys. Rev. Lett.* 120 (2018), p. 156804. DOI: 10.1103/PhysRevLett.120.156804.

[46]   Z. Jin and J. E. Subotnik. "A Practical Ansatz for Evaluating the Electronic Friction Tensor Accurately, Efficiently, and in a Nearly Black-Box Format". In: *J. Chem. Phys.* 150 (2019), p. 164105. DOI: 10.1063/1.5085683.

2

Chapter 3

An Improved Static Corrugation Model

3

Abstract

Accurately describing surface temperature effects for the dissociation of H_2 on Cu(111) remains challenging. While Ab initio Molecular Dynamics (AIMD), the current state-of-the-art method for modelling such systems, can produce accurate results, it is computationally too expensive to use for extensive testing of, for example, density functionals. A chemically accurate static corrugation model for H_2 and D_2 on Cu(111) dissociation was made by introducing effective three-body interactions as well as an H_2-bond dependence and fitting the model to density functional theory energies for 15113 different configurations. Reaction probabilities and rovibrational (in)elastic scattering probabilities were computed and compared to experiments and other calculations. Theoretical and experimental results are in good agreement, except for the reaction of (v=0, J=0) H_2 where both AIMD and the newly developed static corrugation model, both based on the same underlying density functional, predict a similar deviation from experiment.

3.1 Introduction

Heterogeneously catalysed processes such as the Haber-Bosch [2] process and the hydrogen and oxygen evolution reactions of water splitting [3] are essential for modern day industry. To gain insight into how these processes are catalysed efficiently, for example by metal interfaces, the reaction mechanism is broken down into elementary reaction steps, which are subsequently studied individually. Understanding these elementary reaction steps can then, hopefully, lead to better catalysis of chemical processes on surfaces. One such elementary reaction step is the dissociation of H_2 and D_2 on Cu(111), which has been extensively studied both experimentally [4–9] and theoretically [10–17].

For modeling such systems, the Born-Oppenheimer approximation (BOA) is often used to separate the nuclear and electron dynamics. A ground state electronic structure theory such as density functional theory (DFT) is then used to compute the energy at several nuclear configurations resulting in a potential energy surface (PES). For the dissociative chemisorption probabilities of H_2 and D_2 on Cu(111), it is known that the BOA performs well [18, 19] and the small effect that is present is discussed extensively

in Chap. 4. One way to determine the overall accuracy of the electronic structure is to calculate the probability of H_2 reacting on the Cu(111) surface at specific translational and rovibrational energies and compare the result with experiments. DFT can be used together with the specific reaction parameter (SRP) method to compute a chemically accurate PES for the H_2 on Cu(111) system [12].

In practice, chemical processes at surfaces are performed at high surface temperatures, which complicates the fundamental understanding even further. To include the effect of surface temperature on the dissociation of H_2 and D_2 on Cu(111) however, the PES must somehow take surface displacements into account. It is computationally convenient to reduce the PES to a 6D PES [15, 16] and describe the effect of surface displacements as a perturbation of the 6D PES. This was done previously with the static corrugation model (SCM) [14]. Here it was assumed that H_2 interacts with essentially a static snapshot of a thermally equilibrated Cu(111) surface. This was motivated for H_2 and D_2 on Cu(111) due to the large mass mismatch allowing no significant energy exchange due to collisions of the molecule with the surface. Furthermore, the comparatively slow velocity of thermally equilibrated Cu atoms results in no significant surface motion during the short interaction time of H_2 at the Cu(111) surface. In contrast, it is also possible to compute the electronic structure on an "as needed" basis using ab-initio molecular dynamics (AIMD) [10], circumventing the need to make any further approximations, albeit at increased computational effort. The SCM was able to reproduce experimental and AIMD molecular beam experiments [10] within chemical accuracy (1 kcal/mol), even though the results of the fitting procedure used suggested that the errors should be larger. Recently it has also become possible to use high-dimensional neural network potentials [20–22] (HD-NNP) to describe the effect of surface displacements in molecule surface reactions. This method has also been used in Chap. 5. While this seems a promising alternative to both AIMD and the SCM, I am not aware of any accurate HD-NNP for H_2 on Cu(111), using the same DFT functional as was used for AIMD [10], at the moment of writing.

Our goal is now to improve the SCM for the H_2 and D_2 on Cu(111) system to even more accurately reproduce the results of AIMD and experimental data, while

maintaining the advantage in computational effort.

3.2   Methods

3.2.1   Ab Initio Calculations for H_2 at Cu(111)

For the H_2 on Cu(111) system a chemically accurate SRP functional [11, 12] has been
created by taking a linear combination of 0.52 PBE [23] and 0.48 RPBE [24]. To be
able to compare the SCM to previous AIMD results, the underlying PES should be
reproduced as closely as possible. This was done by performing ground state DFT
calculations using the Vienna Ab-initio Simulation Package (VASP) [25–27]. Calcu-
lations were performed using the Ultra-Soft (US) pseudopotentials [25, 27] provided
by VASP, an 8 by 8 by 1 Γ-centered k-point grid, an energy cut-off of 350 eV for the
planewave basis set, a Fermi-smearing with a temperature corresponding to 0.1 eV and
a convergence criterion of 0.1 meV.

   Figure 3.1 shows a schematic overview of the H_2 on Cu(111) system. The Cu(111) slab
has a FCC bulk structure with a cut in the ⟨111⟩ direction and consists of four layers.
These layers are defined using the lattice vectors u and v with u being in the same
direction as x while v has an angle of $\frac{\pi}{3}$ with u. The different layers are shifted in u
and v of one third of both lattice vectors and the interlayer distances are optimised
for a 1 by 1 unit cell. A 3 by 3 unit cell was used in all calculations performed for
computing coupling potentials.

3.2.2   Static Corrugation Model

The Static Corrugation Model (SCM) [14] is used to describe the effect of surface
temperature due to surface atom displacements on the potential energy surface (PES)
of a surface($\overrightarrow{q}$)-adsorbate($\overrightarrow{r}$) system. This is realised by dividing the DFT PES
$V_{DFT}(\overrightarrow{q}, \overrightarrow{r})$ into three terms: $V_{DFT}(\overrightarrow{q}^{id}, \overrightarrow{r})$ associated with an ideal surface , V_{strain}
associated with distorting a clean surface and V_{coup} associated with the change in the
interaction of an adsorbate with the surface due to a surface atom displacement, as
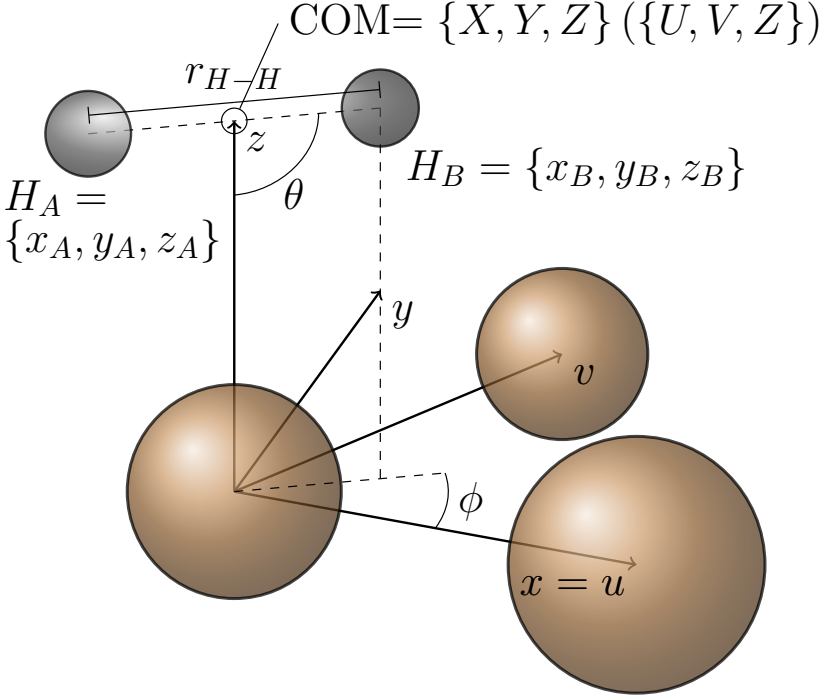
Figure 3.1: Molecular coordinate system of H_2 as well as lattice vectors for Cu(111) are shown. The first layer Cu atoms are indicated in brown while the H atoms are indicated in gray. Indicated are the z, y, $x(= u)$ and v unit vectors. H_2 is described in both an atomic coordinate system, using the position of H_A and H_B on the x, y and z axis as well as a molecular coordinate system using the position X, Y, Z (U, V, Z) of the COM on the x, y and z $(u, v$ and $z)$ axis respectively, together with bond distance r_{H-H}, polar angle θ and azimuthal angle ϕ.

given by

$$V_{DFT}(\overrightarrow{q}, \overrightarrow{r}) = V_{DFT}(\overrightarrow{q}^{id}, \overrightarrow{r}) +$$
$$V_{coup}(\overrightarrow{r}, \overrightarrow{q}^{id} \rightarrow \overrightarrow{q}) + V_{strain}(\overrightarrow{q}^{id} \rightarrow \overrightarrow{q}), \tag{3.1}$$

where $\overrightarrow{q}$ describes the Cartesian positions of all surface atoms, $\overrightarrow{q}^{id}$ describes the ideal lattice positions in the same way and $\overrightarrow{r}$ describes the Cartesian positions of

all adsorbate atoms (in this chapter only atom A and B). The strain potential $V_{strain}(\overrightarrow{q}^{id} \rightarrow \overrightarrow{q})$ can be neglected for dynamics on a static surface because it is a constant if the surface configuration does not change during the dynamics. Using equation 3.1 and neglecting V_{strain}, the SCM thus approximates the full dimensional DFT PES according to

$$V_{DFT}(\overrightarrow{q}, \overrightarrow{r}) \approx V_{SCM}(\overrightarrow{r}, \overrightarrow{q}^{id} \rightarrow \overrightarrow{q}) =$$
$$V_{DFT}(\overrightarrow{q}^{id}, \overrightarrow{r}) + V_{coup}(\overrightarrow{r}, \overrightarrow{q}^{id} \rightarrow \overrightarrow{q}). \tag{3.2}$$

To be able to perform dynamics with the static corrugation potential, a continuous representation needs to be found for the ideal lattice $V_{DFT}(\overrightarrow{q}^{id}, \overrightarrow{r})$ as well as the coupling potential $V_{coup}(\overrightarrow{r}, \overrightarrow{q}^{id} \rightarrow \overrightarrow{q})$. It should be noted that HD-NNP could be a good alternative to obtain a continuous representation of the coupling potential $V_{coup}(\overrightarrow{r}, \overrightarrow{q}^{id} \rightarrow \overrightarrow{q})$. However, the work presented in this chapter will continue along the lines of earlier work [14] to be able to make a more thorough comparison. A representation of the SCM potential can be found by interpolating the DFT energies for the ideal surface using the CRP method [15] and fitting the coupling potential with a functional form according to

$$V_{coup}(\overrightarrow{r}, \overrightarrow{q}^{id} \rightarrow \overrightarrow{q}) =$$
$$\sum_i^{\overrightarrow{r}} \sum_j^{\overrightarrow{q}} \left(V_{H-Cu}(|\overrightarrow{r}_i - \overrightarrow{q}_j|) - V_{H-Cu}(|\overrightarrow{r}_i - \overrightarrow{q}_j^{id}|) \right), \tag{3.3}$$

where $\overrightarrow{r}_i$ is the Cartesian position of adsorbate atom i, $\overrightarrow{q}_j$ is the Cartesian position of surface atom j and

$$V_{H-Cu}(r) = V_{Ryd} = (1 - \rho(r))V(r) + \rho(r)V(P_7), \tag{3.4}$$

while

$$V(r) = -e^{-P_4(r-P_5)} \cdot \left(\sum_{k=0}^{3} P_k(r - P_5)^k \right), \tag{3.5}$$

and

$$\rho(r) = \begin{cases} 0 & \text{if } r < P_6 \\ \frac{1}{2}\cos\left(\frac{\pi(r-P_7)}{P_7-P_6}\right) + \frac{1}{2} & \text{if } P_6 \leq r \leq P_7 \\ 1 & \text{if } r > P_7 \end{cases} \quad , \qquad (3.6)$$

where P_i are the fitted parameters.

The SCM for H_2 on Cu(111) from previous work [14] is extended by including an effective three-body interaction, a corrected surface stretching procedure and a fitting procedure of the coupling potential including many more relevant surface and molecule configurations. We have recalculated the reaction probabilities for the model of Ref. [14] but using an improved implementation of the force scaling due to thermal expansion of the Cu crystal via the stretching procedure.

To include surface expansion due to surface temperature, the CRP potential of the system is stretched by contracting the H_2 COM vectors along the lattice vectors, instead of the Cartesian vectors of the atoms as was done previously. In this way there are no additional small but unwanted contributions to the vibrational and rotational motion due to the stretching procedure. Hence, the full SCM potential becomes

$$V_{SCM}(\overrightarrow{r}, \overrightarrow{q}, \overrightarrow{q}^{id}) = V_{CRP}(\overrightarrow{r}^{id}(\overrightarrow{r}), \overrightarrow{q}^{id})$$
$$+ \sum_i^{\overrightarrow{r}} \sum_j^{\overrightarrow{q}} \left(V_{H-Cu}(|\overrightarrow{r}_i - \overrightarrow{q}_j|) - V_{H-Cu}(|\overrightarrow{r}_i^{id}(\overrightarrow{r}) - \overrightarrow{q}_j^{id}|) \right), \qquad (3.7)$$

where $\overrightarrow{r}^{id}(\overrightarrow{r})$ scales the expanded surface H_2 coordinates $\overrightarrow{r}$ along the COM U and V coordinates to the ideal surface in such a way that they correspond to the same relative coordinates. The reaction probabilities using the original SCM model [14] that are reported here using the improved implementation show no major differences compared to the previous results. The above methodology can be used for any 6D PES and is not limited to a CRP PES.

In order to improve upon the SCM, a H-Cu interaction is defined that is not only dependent on the distance between the H_i atom and Cu_j atom (r_{ij}) but also on the H-H bond distance (r_{H-H}). This essentially describes the different behaviour of the H-Cu interaction for H as a part of an H_2 molecule (small r_{H-H}) and for H as an

atom (large r_{H-H}). This was done by making all the parameters P_i of the previous two-body SCM linearly dependent on r_{H-H} as given by

$$P_i = \begin{cases} P_{i,a}r_{H-H}^{min} + P_{i,b} & \text{if } r_{H-H} < r_{H-H}^{min} \\ P_{i,a}r_{H-H} + P_{i,b} & \text{if } r_{H-H}^{min} \leq r_{H-H} \leq r_{H-H}^{max} \\ P_{i,a}r_{H-H}^{max} + P_{i,b} & \text{if } r_{H-H} > r_{H-H}^{max} \end{cases} , \qquad (3.8)$$

where r_{H-H}^{min} and r_{H-H}^{max} are cut-off values of the linear dependence set at the smallest and largest value of r_{H-H} used in the fitting procedure. The resulting Rydberg function is then considered an H_2-bond adapted Rydberg function.

3.2.3 Quasi-Classical Dynamics of H_2 and D_2 on Cu(111)

Using either the CRP (V_{CRP}) or SCM PES (V_{SCM}), it is possible to describe the dissociation of H_2 or D_2 on an ideal or non-ideal (with displaced Cu atoms) Cu(111) surface. The PES itself is not a directly measurable observable, so instead molecular beam simulations have been performed. These simulations were performed using the Quasi-Classical (QC) Dynamics [12, 16] method. Initial conditions are determined by using a Monte-Carlo sampling scheme, where zero point energies for the H_2 bond were taken into account only for the initial configurations. Then the system is propagated classically and the resulting trajectory is finally analyzed. We performed 20000 trajectories for each choice of incidence energy E_i, vibrational state v and rotational state J.

The initial conditions for the molecule are generated by first calculating the rovibrational energy levels of the H_2 or D_2 molecule for the used PES using the Fourier grid Hamiltonian method [28]. To get the QC distribution for the H-H bond distance r_{H-H} of the H_2 molecule, the gasphase H_2 molecule was propagated, and positions and momenta were recorded, for one complete phase in its vibration using a constant time step. The initial atomic positions and velocities were then chosen using standard Monte-Carlo methods. The ϕ and θ angles are chosen from an uniform random distribution in the range $[0, 2\pi]$ and $[0, \pi]$ respectively. Angular velocities are chosen according to the quantized angular momentum $L^2 = J(J+1)\hbar^2$ with the angle θ_L

between the angular momentum vector and the surface normal chosen randomly but constrained by $\theta_L = \pi$ if J=0 and $cos(\theta_L) = \frac{m_J}{\sqrt{J(J+1)}}$ if J$\geq$1. The Z component of the COM velocity is set to correspond to a kinetic energy of E_i. The initial COM position is then shifted 9 Å in Z away from the surface (Z=9 Å) while the COM position along the FCC(111) surface is given by X = $\widetilde{U} + \frac{1}{2}\widetilde{V}$ and Y = $\frac{1}{2}\sqrt{3}\widetilde{V}$ where $\widetilde{U}$ and $\widetilde{V}$ are chosen from an uniform random distribution in the range $[0, a]$ with a being the lattice constant. This process was identical to earlier work [10, 12, 14, 16, 17].

The SCM uses the surface atom positions of both the ideal lattice and the corrugated lattice. The ideal lattice is constructed in the same way as the DFT slab used for constructing the CRP with the exception that no periodic boundary conditions are used. Instead, for each trajectory, the initial COM position is projected onto the surface plane and only copper atoms that are from the first three layers and within a radius of 12 Å around the projected COM are considered. The corrugated lattice is constructed from this ideal lattice in three steps. First, the surface expansion along the u and v lattice vectors is introduced. The relative experimentally [29] observed expansion is applied to the lattice constant from the CRP potential. Secondly the interlayer spacings are adjusted in a similar fashion: the experimentally observed relative expansion or contraction [30] in the interlayer spacings is applied to the interlayer spacings used in the DFT slab of the respective CRP potential. Finally, for each surface atom a random direction is chosen and the magnitude of the displacement is randomly selected from an appropriate surface temperature dependent gaussian distribution based on Debye-Waller factors [31].

Once the initial conditions are defined, only the molecule is propagated according to Hamilton's equations of motion with the following hamiltonian (in atomic units):

$$H = \frac{p_A^2(t)}{2m_A} + \frac{p_B^2(t)}{2m_B} + V(R(t)). \tag{3.9}$$

where $p_A(t)$ and $p_B(t)$ are the momenta of atoms A and B respectively at time t and $V(R(t))$ is the potential energy at the Cartesian position $R(t)$ of both atom A and B. The propagation is performed using the predictor-corrector method of Bulirsch and Stoer [32]. A trajectory is considered to be reactive when the H atoms are separated

47

by more than 2.25 Å before the time cut-off of 20 ps and considered non-reactive otherwise. When a trajectory is non-reactive, the molecule is either trapped as a molecule on the surface, or has scattered to the same or a different rovibrational state which is called elastic or inelastic scattering respectively. No significant contribution of trapped molecules was found during this study and are therefore not reported. The final rovibrational state is determined by binning first to the rotational state based on angular momentum and then to the closest vibrational state in energy with the previously determined rotational state. Results have been obtained for the H_2 and D_2 on Cu(111) system with both an ideal lattice, and a displaced and expanded lattice at a finite surface temperature of T_s=925K.

3.3 Results and Discussion

3.3.1 Coupling potential

To be able to verify and improve the fit of the coupling potentials used in previous work [14] the computation of the coupling potentials is' repeated, but this time with the same DFT setup as was used for AIMD calculations [10]. A comparison with these AIMD results and the SCM results can show the importance of surface motion compared to surface displacement. To improve the old SCM model, the new SCM model is fitted to the coupling potential for 15113 configurations instead of 153.

To test the previous assumption that the coupling potential can be approximated with only two-body interactions i.e. H-Cu interactions, the coupling potential are computed at configurations $(\overrightarrow{q}_{id} \rightarrow \overrightarrow{q}_{id} + \overrightarrow{Q}_1 + \overrightarrow{Q}_2)$ where two displacements $(\overrightarrow{Q}_1$ and $\overrightarrow{Q}_2)$ were made to isolate H-Cu-Cu effective three-body interactions. To compute the H-H-Cu effective three-body interactions, the configurations with the displacements $\overrightarrow{q}_{id} \rightarrow \overrightarrow{q}_{id} + \overrightarrow{Q}$ and $\overrightarrow{r} \rightarrow \overrightarrow{r}'$ were used. This has two advantages, namely fitting these coupling potentials will result in an effective three-body interaction but at the same time it allows us to test how well the two-body approximation performs.

Coupling potentials presented here are computed exactly from DFT calculations

according to

$$V_{coup}(\overrightarrow{r}, \overrightarrow{q}_{id} \to \overrightarrow{q}_{id} + \overrightarrow{Q}) = V_{DFT}(\overrightarrow{r}, \overrightarrow{q}_{id} + \overrightarrow{Q})$$
$$-V_{DFT}(\overrightarrow{r}, \overrightarrow{q}_{id}) - V_{strain}(\overrightarrow{q}_{id} \to \overrightarrow{q}_{id} + \overrightarrow{Q}), \tag{3.10}$$

where

$$V_{strain}(\overrightarrow{q}_{id} \to \overrightarrow{q}_{id} + \overrightarrow{Q}) =$$
$$V_{DFT}(\overrightarrow{r}_{gas}, \overrightarrow{q}_{id} + \overrightarrow{Q}) - V_{DFT}(\overrightarrow{r}_{gas}, \overrightarrow{q}_{id}), \tag{3.11}$$

with $\overrightarrow{r}_{gas}$ indicating that the H_2 molecule has been moved 6 Å away from the surface such that there is essentially no interaction between H_2 and the surface. Here the displacement $\overrightarrow{r} \to \overrightarrow{r}'$ is understood as simply evaluating the coupling potential at $\overrightarrow{r}'$ instead of $\overrightarrow{r}$.

First the H-Cu-Cu three-body coupling potential is considered. For these coupling potentials, the H_2 was placed at the barrier position of either the bridge, top or HCP site. Two atoms were selected from the first two layers in the surface considering all permutations and symmetries. These were then either moved in all possible combinations of the directions $x(= u)$, y, v and z, as well as both atoms moving towards and away from the H_2 COM. The displacements have a magnitude from -0.3 Å until 0.3 Å with a step of 0.1 Å. There are too many permutations to discuss all of them but a representative selection is discussed next.

Figure 3.2 shows the coupling potentials of the surface displacements of the two surface atoms closest to the H_2 COM perpendicular to the surface and H_2 at the lowest barrier for this system(bridge site barrier). The displacements $\overrightarrow{Q}_1$ and $\overrightarrow{Q}_2$ are in this case symmetric due to the mirror plane along the H bond, meaning that the values for the displacements can be swapped without changing the coupling potential. What is interesting to note here is that the lowest coupling potential is not at the ideal lattice positions (with the displacements at 0 Å) but with the surface atoms slightly moved out of the surface, indicating a puckering [33] effect. This puckering effect can not be taken into account using the SCM (where static surface configurations are Monte-Carlo sampled randomly), however it is not expected to have a large influence
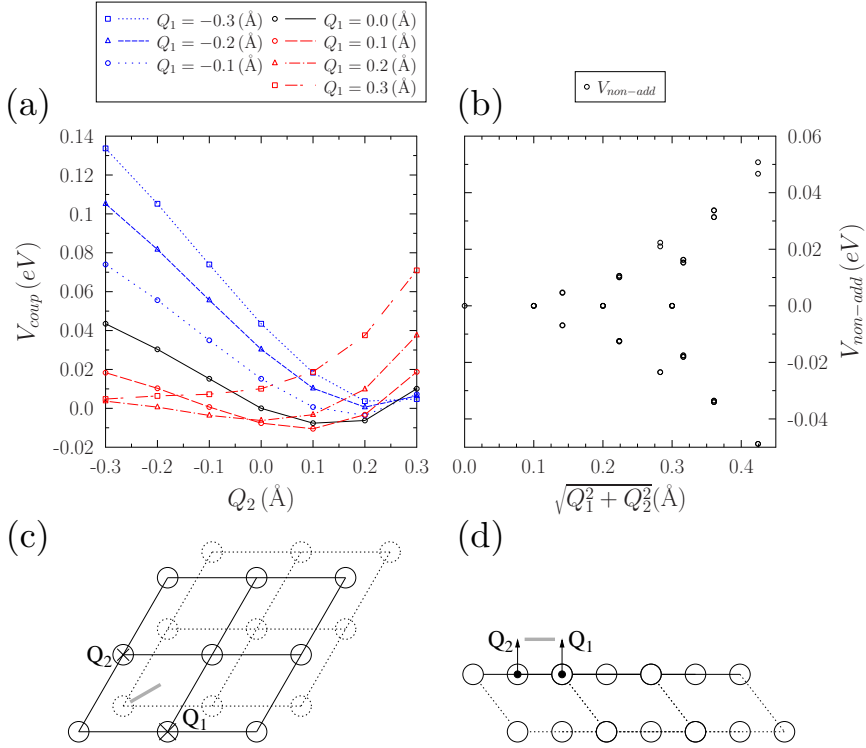
3

Figure 3.2:   (a) shows V_{coup} for displacements along $\overrightarrow{Q}_1$ and $\overrightarrow{Q}_2$ where black, red and blue show no, a positive and a negative displacement along $\overrightarrow{Q}_1$ respectively. The displacements $\overrightarrow{Q}_1$ and $\overrightarrow{Q}_2$ are defined in (c) and (d) by showing a top and front view of the system respectively, where Cu atoms are indicated using circles and H_2 by the gray bar. (b) shows the non-additivity (see eq. 3.12) of the coupling potentials presented in (a). Q_1 and Q_2 in (a) and (b) refer to the magnitudes $|\overrightarrow{Q}_1|$ and $|\overrightarrow{Q}_2|$ respectively while Q_1 and Q_2 in (c) and (d) are the vectors $\overrightarrow{Q}_1$ and $\overrightarrow{Q}_2$.

on dynamics due to the large mass difference between H_2 and D_2 with Cu as well as the high velocities and consequent short interaction time of H_2.

The configuration with the most favorable coupling potential in figure 3.2, at -10.5 meV, is when both atoms are displaced by +0.1 Å along $\overrightarrow{Q}_1$ and $\overrightarrow{Q}_2$. When only one

atom is displaced while the other is at its ideal lattice position, the coupling potential is 7.5 meV. From a perspective where only additive interactions are considered (see eq. 3.7), this cannot be explained as both surface atoms should then interact independently. This means that a three (or more)-body interaction is present, or in other words: there is non-additivity of the coupling potential due to the surface displacements of two or more Cu atoms. The non-additivity of the coupling potential (see equation 3.10) is defined as the difference between the coupling potential of displacements $\vec{Q}_1$ and $\vec{Q}_2$ with the sum of the coupling potentials of only $\vec{Q}_1$ and only $\vec{Q}_2$ as given by

$$
\begin{aligned}
V_{nonadd}(\vec{r}, \vec{q}^{\,id} &\to \vec{q}^{\,id} + \vec{Q}_1 + \vec{Q}_2) = \\
V_{coup}(\vec{r}, \vec{q}^{\,id} &\to \vec{q}^{\,id} + \vec{Q}_1 + \vec{Q}_2) \\
-V_{coup}(\vec{r}, \vec{q}^{\,id} &\to \vec{q}^{\,id} + \vec{Q}_1) \\
-V_{coup}(\vec{r}, \vec{q}^{\,id} &\to \vec{q}^{\,id} + \vec{Q}_2).
\end{aligned} \tag{3.12}
$$

While this non-additivity can never be modeled with an additive interaction there are good arguments to believe that they are not too important. First of all, the additive interaction can be fitted including the configurations with non-additivity, resulting in an effective non-additive interaction that takes into account the average non-additivity. The distribution of the non-additivity was found to have a mean of -0.5 meV and a standard deviation (SD) of 6.3 meV which means that on average the correct coupling potential should be reproduced only introducing a slightly bigger spread in the modeled coupling potentials. Furthermore, the configurations where there is a lot of non-additivity are when there are two specific surface atoms that both have a large displacement. While it is certainly true that a single displacement of such a magnitude is not extremely unlikely, having two such large displacements is even less common and therefore decreases the probability of sampling this error. Finally, in a realistic configuration of a non-ideal surface all surface atoms are displaced and combining this with the fact that the non-additivity introduces an error that is on average zero, there is an even smaller mean error under these realistic conditions. Even without these arguments, under these circumstances, the absolute mean error of this non-additivity is well within the accuracy one can expect for the underlying DFT.
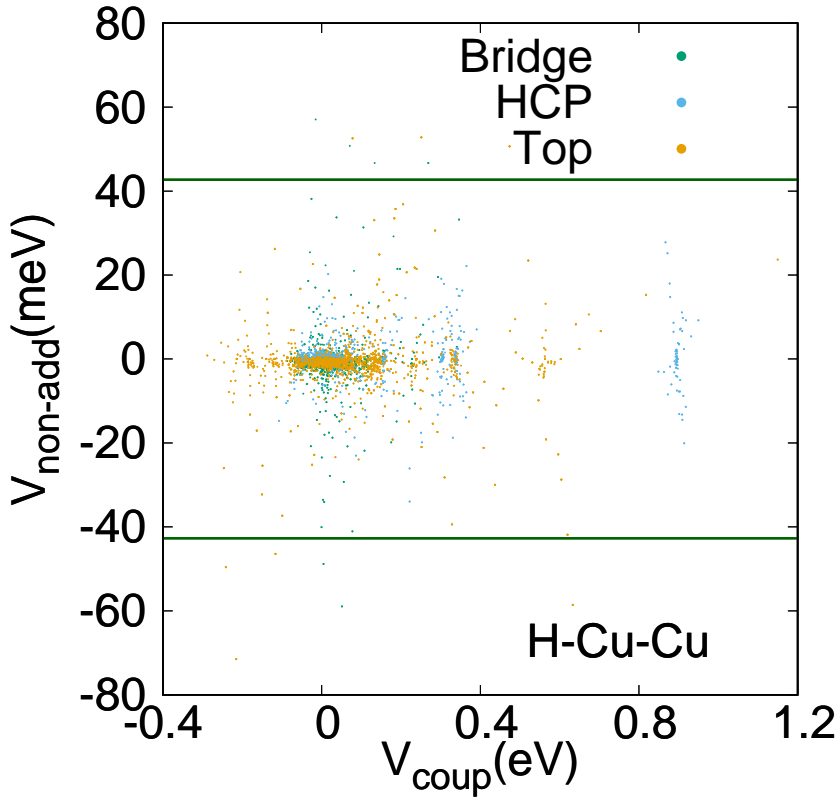
Figure 3.3: The non-additivity of V_{coup} is correlated to the value of V_{coup} for configurations with two surface atom displacements (H-Cu-Cu three-body interactions) and H_2 at the Bridge (green), HCP (blue) and Top (orange) site. The potential at which the non-additivity exceeds chemical accuracy is shown as a reference in dark green (these 43 meV lines correspond to more than 6 times the SD of the DFT data (6.3 meV))

In figure 3.3 a summary is presented of the coupling potentials and their respective non-additivity. The green lines are added as a reference to show the approximate accuracy of the underlying DFT method used. The behavior of the H-Cu-Cu non-

additivity is essentially independent of the chosen site (Bridge, HCP, Top) for H_2. Almost all coupling potentials of the H-Cu-Cu type have a non-additivity smaller than the accuracy of the DFT method, which means that any subsequent improvement of the fitting quality is not guaranteed to yield a more realistic coupling potential.

The H-H-Cu coupling potentials describe how the coupling potential changes when the H_2 bond distance changes ($\overrightarrow{r} \to \overrightarrow{r}'$) whilst also displacing a single Cu atom ($\overrightarrow{Q}$) at the same time. These coupling potentials were selected in a similar fashion as the H-Cu-Cu coupling potentials. Instead of selecting two surface atoms, only one was selected and the same displacements were used for the single atom in combinations with increasing and decreasing the H_2 bond distance from -0.3 Å until 0.3 Å with respect to the barrier position in steps of 0.1 Å. Other degrees of freedom of H_2 were sampled in the same way. Consequently, the H-H-Cu non-additivity is given by

$$
V_{nonadd}(\overrightarrow{r} \to \overrightarrow{r}', \overrightarrow{q}^{id} \to \overrightarrow{q}^{id} + \overrightarrow{Q}) =
$$
$$
V_{coup}(\overrightarrow{r}', \overrightarrow{q}^{id} \to \overrightarrow{q}^{id} + \overrightarrow{Q})
$$
$$
-V_{coup}(\overrightarrow{r}, \overrightarrow{q}^{id} \to \overrightarrow{q}^{id} + \overrightarrow{Q})
$$
$$
-V_{coup}(\overrightarrow{r}', \overrightarrow{q}^{id} \to \overrightarrow{q}^{id}), \tag{3.13}
$$

where $V_{coup}(\overrightarrow{r}', \overrightarrow{q}^{id} \to \overrightarrow{q}^{id}) = 0$ due to the lack of surface displacements. The H-H distance r_{H-H} ranges from H_2 having dissociated at very large bond distances to the bond distance being so short that almost all available energy in the system has gone into this compression. Unlike the H-Cu-Cu interactions, the H-H-Cu interactions cannot be reproduced within chemical accuracy using a two-body H-Cu interaction. Figure 3.4 shows the non-additivity of the H-H-Cu coupling potentials and there is a much broader distribution with a mean of -5.0 meV and a SD of 74.6 meV, with some non-additivities being more than ten times chemical accuracy. Generally the non-additivity and coupling potential presented in this chapter are linearly dependent on the H_2-bond distance. Such linear dependence has been seen before for the vibrational coupling of diatomics interacting with atoms and other diatomics [34, 35]. In contrast to the H-Cu-Cu non-additivity, there is a slight difference of the H-H-Cu non-addivity for H_2 at different sites. There is a larger spread of the non-additivity for H_2 at the bridge
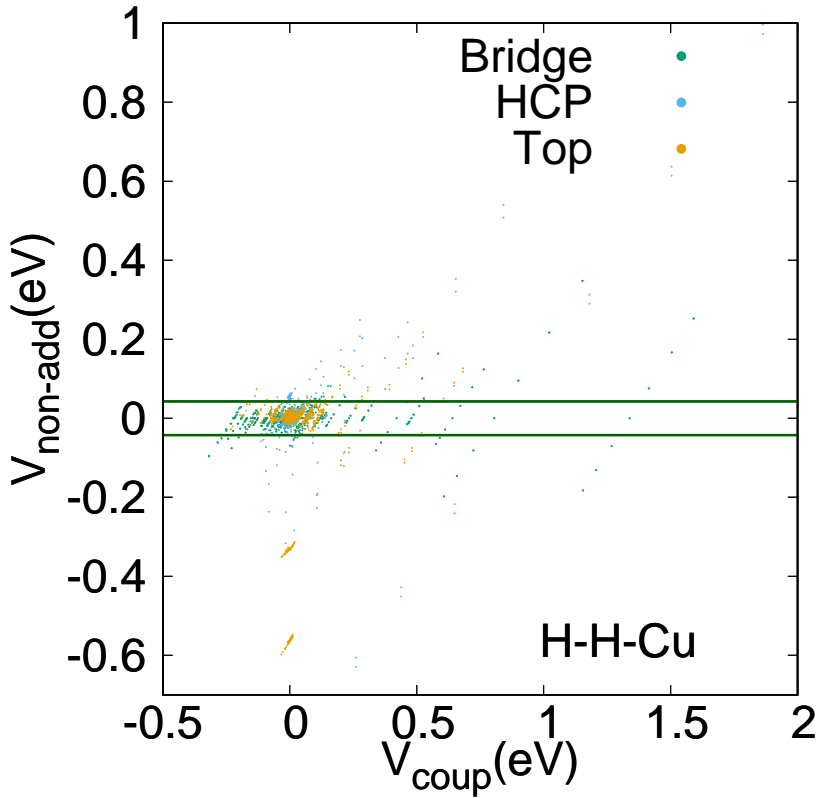
Figure 3.4: Same as Figure 3.3 but for configurations with one surface atoms displacement combined with the H-H bond not at the equilibrium distance (H-H-Cu three-body interactions).

site, while for some configurations at the top site there is a very large non-additivity, eventhough there is a small coupling potential. Due to the large non-additivity for H-H-Cu interactions, I conclude that it is necessary to make use of the H_2-bond adapted Rydberg function.

3.3.2 Parameters for the Static Corrugation Model

The coupling potential discussed in the two previous sections was fitted using the H_2-bond adapted Rydberg function using the fitting procedure described above.

All fits take the H-Cu-Cu interactions into account only effectively while the H-H-Cu interactions are taken into account through the r_{H-H} dependence of the parameters P (see equation 3.8). The fitting procedure was repeated with four different sets of constraints. First the most relaxed case where H-H-Cu three-body interactions are taken into account and two different sets of parameters were assigned, one for the first and one for the second surface layer copper atoms involved in the H-Cu interaction (3Body 2Layer). Then there is the case were a single set of parameters is used for both layers (3Body 1Layer) and the case where all non-additive interactions are taken into account only effectively (2Body 2Layer). Finally the fit was also performed constraining both the parameters to a single set and taking non-additive interactions into account only effectively (2Body 1Layer). This is thus essentially a refit of the old SCM [14] using the new and vastly extended set of DFT data set and consequent coupling potential. The best fit is for the 3Body 2Layer case with a close second place for the 3Body 1Layer case. The other two cases have a very similar RMSE as reported in literature for other methods such as the ReaxFF [36]. In the case of the H_2-bond adapted Rydberg function the plots are for several different H_2-bond distances as shown in table 3.3. An overview of the RMSE is presented in table 3.1 and the parameters for all 1Layer cases are given in table 3.2.

Table 3.1: An overview of the different fitting constraints and the corresponding names.

Fit	3 Body interactions	Different parameter sets	RMSE (meV)
3Body 2Layer	Yes	Yes	29.4
2Body 2Layer	No	Yes	62.4
3Body 1Layer	Yes	No	42.7
2Body 1Layer	No	No	66.6

Table 3.2: Fitted SCM Parameters where units of length are in Bohr and units of Energy in Hartree. Columns a and b for the 3-body interactions refer to $P_{i,a}$ and $P_{i,b}$ from equation 3.8.

	Ref. [14]	2-body	3-body	
			b	a
P_0	-0.0303	-0.0339	-0.0704	0.0166
P_1	0.1035	0.1024	0.0235	0.0287
P_2	-0.0692	-0.0802	-0.0633	-0.0072
P_3	-	0.0111	0.0272	-0.0064
P_4	2.3005	2.3023	2.2897	0.0236
P_5	1.2744	1.2929	1.2910	-0.0031
P_6	7.4442	7.4400	7.4402	0.0008
P_7	7.4636	10.4600	10.4601	0.0000

Comparing the V_{H-Cu} interaction from previous work [14] with the 2Body 1Layer fit to the new DFT data set in figure 3.5 the interaction is weaker than before but qualitatively very similar. The position of the maximum is shifted to about half a Bohr shorter H-Cu distance while the position of the well is still the same. When instead the fit is performed with different parameters for different layers, the first layer interaction is shifted to a lower energy but the barrier and equilibrium position are still very similar in position and height. The second layer interaction on the other hand becomes much more repulsive at low distance and slightly more attractive at high distances. It should be noted here that the repulsive wall is not a regime that is sampled as it is not possible for an H atom to get this close to a second layer atom. The three-body interaction is represented in figure 3.5 by showing the energy dependence of the H-Cu distance at several fixed values of the H-H distance as discussed in table 3.3 (green curves). The general shape of the interaction is the same at every H-H distance but at high H-H distances the barrier is much higher while the well is much lower in energy. There is also a slight broadening effect, such that the well is shifted to smaller H-Cu distances and the barrier to larger H-Cu distances. At very small H-H

Table 3.3: An overview of the different H-H distances used in this section

Name	H-H Distance (Å)
Bridge	1.025
HCP	1.547
Top	1.402
Lowest (r_{min})	0.725
Highest (r_{max})	1.847

distances, the V_{H-Cu} interaction becomes almost completely repulsive. Surprisingly, the bridge site, which has the lowest H-H distance and therefore the most repulsive H-Cu interaction, actually has the lowest barrier for reaction. These two statements are not contradictory because the H-Cu interaction only includes the influence of the H-H distance on V_{coup} and not the H-H interaction itself, which is included in the CRP potential (V_{CRP}). The described features suggest that the fitted potential is at least qualitatively in agreement with the properties of the PES and the RMSE suggests that there is also a quantitative agreement.

While the RMSE of the 3-body 2-layer fit suggests it is the best fit, the shape of the V_{H-Cu} interaction potential tells a different story. The problem in this case is the fit coverage: there are almost no first layer interactions in the 8 to 10 Bohr region so there is no constraint on the fitting procedure to keep the V_{H-Cu} interaction at a sensible value. Dynamical calculations using the underfitted 3-body 2-layer V_{H-Cu} yielded non-sensible results and are not presented in this work.

Henceforth in this chapter only a single set of parameters used for both the first and second layer H-Cu interaction is considered instead. Using that fitting procedure to fit the new set of coupling potentials this chapter presents a successfully fitted H_2-bond adapted Rydberg function. The resulting RMSE of the 3-body 1-layer fit is significantly improved compared to the RMSE of the SCM from previous work [14] when applied to the new DFT data set and is within the same accuracy as the DFT data used for the fitting.
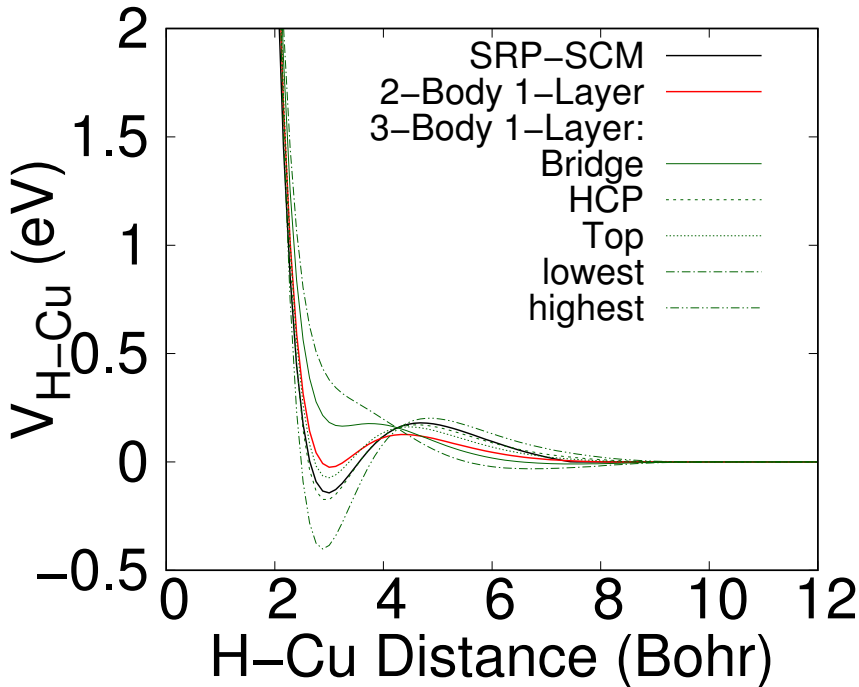
Figure 3.5: The V_{H-Cu} interaction is shown as a function of the H-Cu distance r_{H-Cu} for the SCM from Ref. [14] (black), the 2-body 1-layer fit (red) and the 3-body 1-layer fit (green) . The three-body interaction is represented by showing the potential dependence on the H-Cu distance at specific H-H distances according to table 3.3.

3.3.3 Dynamics on Different Potential Energy Surfaces

To properly compare the newly developed SCM with the previous SCM [14], which use two comparable but slightly different DFT functionals, a comparison between the results using the 6D CRP interpolations (BOSS) for the two used functionals is presented first. The previous SCM used the SRP functional by Díaz et al. [16], for which the CRP interpolation is refered to with SRP-BOSS (in red) in this chapter and the newly developed SCM uses the SRP48 functional by Nattino et al. [37] for which a CRP interpolation SRP48-BOSS (in black) was made by Mondal et al. [17]. Using these two

different PESs, dynamical scattering simulations were performed for D_2 on Cu(111). While reaction probabilities have been reported before, the rovibrationally (in)elastic scattering probabilities have not. Only the initial rovibrational states (v=0, J=0), (v=0, J=11) and (v=1, J=6) are discussed here specifically and a general overview is given for the other states computed (for which the results are available digitally).

The general trend for QC reaction probabilities of D_2 on Cu(111) is that at low incidence energies there is no reaction and as the incidence energy increases the reaction probability increases until it reaches a maximum value called the saturation value. As described previously [10], the general curve of the reaction probability can be described with a modified logistics function. When there is no reaction, there can either be elastic scattering or inelastic scattering. At low incidence energies the elastic scattering dominates as there is not yet enough energy or coupling available to cause a rovibrational excitation while at high energies the inelastic scattering dominates as there is more coupling due to the corrugation and anisotropies close to the surface. It is also possible for the H_2 molecule to change its momentum along the surface lattice vectors when scattering, which is called diffraction. The effect of diffraction was not considered in the sense that the reported observables are summed over the final diffraction states.

The differences between the reaction and (in)elastic scattering probabilities predicted by the two PESs (see black and red curves in fig. 3.6) are dependent on the rovibrational state. For the (v=0, J=0) state the reaction and (in)elastic scattering probabilities are different below 0.9 eV while for the (v=0,J=0) state the reaction and (in)elastic scattering probabilities are different above 0.5 eV and for the (v=1,J=6) state the reaction probabilities are the same for all energies whereas the (in)elastic scattering probabilities deviate below 0.5 eV.

The reaction and rovibrationally (in)elastic scattering probabilities for the (v=0, J=0) initial state are shown in figure 3.6a and discussed in detail first. For incidence energies above 0.9 eV, the probabilities are almost the same for the two PESs. The probabilities for elastic scattering are the same above 0.7 eV while the reaction probability is lower in the case of the SRP-BOSS PES and the inelastic scattering probabilities are

higher. This means that in the region of 0.7 eV to 0.9 eV there is a different preference to either react or scatter for the SRP48-BOSS PES compared to the SRP-BOSS PES. In the case of the SRP48-BOSS PES, the preference is more towards reaction, while in the case of the SRP-BOSS PES the incidence energy is converted into some rovibrational excitations and the preference is towards rovibrationally inelastic scattering. At even lower incidence energies the rovibrationally inelastic scattering probability for the SRP-BOSS PES is lower only for the lowest incidence energy, for all other incidence energies it is higher than the rovibrationally inelastic scattering probability of the SRP48-BOSS PES.

For the rotationally excited state (v=0, J=11), as shown in figure 3.6b, there is almost no difference between the two PESs except for a small broadening of the reaction probability in the case of the SRP-BOSS PES compared to the SRP48-BOSS PES. The lower reaction probability is mostly compensated by a higher inelastic scattering for the SRP-BOSS PES.

On the other hand, the two PESs yield very similar reaction probabilities for the vibrationally excited state (v=1, J=6) while the SRP-BOSS PES inelastic and elastic scattering probability curves cross earlier compared to the SRP48-BOSS PES as shown in figure 3.6c . The general trend of all computed rovibrational states is that as more vibrational energy is added, the reaction probabilities become almost identical between the SRP48-BOSS and SRP-BOSS PES while adding more rotational energy causes the elastic and inelastic scattering probabilities to be more comparable.

Here the argument is that these two effects are distinct features of the PESs based on a normal mode analysis performed along the minimum energy path (MEP) for both PESs as given Sec. 3.A. The difference between the widths of the reaction probabilities for the SRP and SRP48 are mostly determined by how much vibrational energy (in r) is added initially in H_2. If vibrational energy is added, the details of the intrinsic curvature (or how the forces along Z and r change) of the PES along the MEP towards the barrier becomes less important because there is more energy available. The (extrinsic) curvature describing the geometric shape of the reaction path is essentially identical for the two PESs. We note that both functionals yield very similar barrier

heights and locations for this system as well as near identical MEPs. Therefore, it could be argued that it is the intrinsic curvature, constrained in r and Z, that determines the different reaction probability widths for the SRP-BOSS and SRP48-BOSS. Previously it has been reported [38] that the energetic corrugation can also have an influence on the reaction probability width, but that would not directly explain the strong dependence on the initial vibrational state. If instead rotational energy is added, the intrinsic curvature, in r and Z, of the PES towards the barrier is still important. A similar argument can be made for the energy at which the rovibrationally elastic and inelastic scattering probability curves cross, where it is mostly the anisotropy in θ and ϕ that determines if the rovibrational state changes. If the molecule is rotating relatively fast, it feels an 'average' of the potential in θ and therefore the exact shape of PES becomes less important.

Both PESs were designed to reproduce molecular beam experiments, where the effective barrier height is the most important property of the PES, but if there is not enough energy available to sample the effective barrier, the shape of the PES towards the barrier is also important.

3.3.4 Comparison of Different Static Corrugation Models

In this section a comparison is made between the new SCM based on the 6D PES from Mondal et al. [17] and the newly fitted coupling potential (SRP48-SCM3B), and a SCM from previous work [14] based on the PES from Diaz et al. [16] (SRP-SCM). Both SCMs were computed for a surface temperature of 925K including both surface displacements and surface expansion as described previously in this chapter and Chap. 2.

Figure 3.6a shows the effect of using the SCM compared to the BOSS model for the rovibrational ground state (v=0, J=0). For the SRP-SCM PES, there is a large broadening [9, 14, 39] of the reaction probability at both low and high reaction probabilities while the SRP48-SCM3B PES only shows increased reaction probabilities at low incidence energies. The reaction probability of the SRP48-SCM3B PES starts to increase earlier compared to SRP-SCM, but after 0.8 eV of incidence energy, the slope

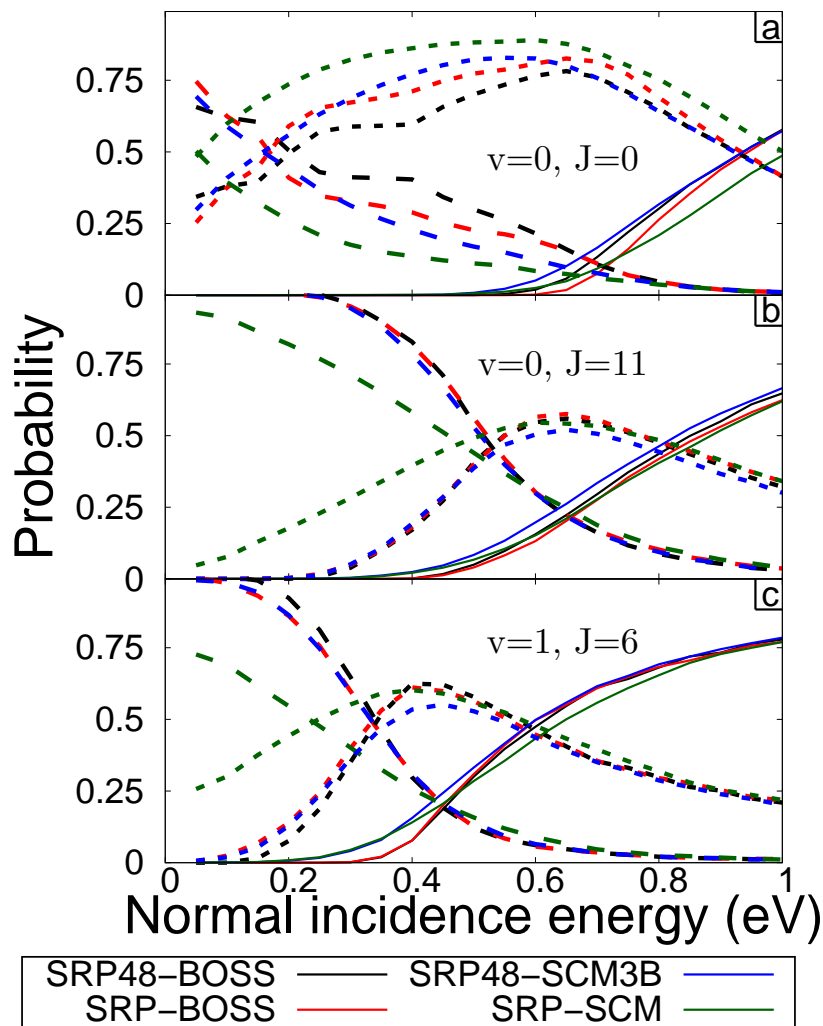Figure 3.6:   The state-specific reaction (solid), elastic scattering (long dash) and inelastic scattering (short dash) probabilities are shown as a function of the incidence energy for SRP48-BOSS (black), SRP48-SCM3B (blue), SRP-BOSS (red) and SRP-SCM (green). (a), (b) and (c) show the (v=0, J=0), (v=0,J=11) and (v=1,J=6) rovibrational state-specific reaction and (in)elastic scattering probabilities respectively.

is essentially the same as for the SRP-SCM PES. The rovibrationally elastic and in-elastic scattering probability curves for the SCM PESs are smoother and do not show sudden changes of the slope as is shown e.g. in the SRP48-BOSS results (black) at 0.4 eV. In the case of SRP-SCM, the rovibrationally inelastic scattering is significantly larger for all incidence energies.

Figure 3.6b shows the result for the rotationally excited (v=0, J=11) state. Here the crossing point of the elastic and inelastic rovibrationally scattering probabilities is the same for SRP-BOSS, SRP48-BOSS and SRP48-SCM3B while SRP-SCM is different. For the (v=1, J=6) state in figure 3.6c the same difference between the SRP-SCM and the others is observed. While the SRP48-BOSS, SRP48-SCM3B and SRP-BOSS PESs are all similar at high incidence energies, when sampling the corrugation close to the Cu(111) surface, the SRP-SCM PES is still different between an incidence energy of 0.4 and 0.9 eV. Furthermore, the rovibrationally inelastic scattering probability is orders of magnitude higher for very low incidence energies.

The general effect of adding the SCM to both the previously discussed PESs seems to be a broadening in the reaction probability, as well as a larger fraction of rovibra-tionally inelastic scattering at low energies compared to the BOSS model. The biggest difference between the SRP-SCM and new SRP48-SCM3B is that the new SRP48-SCM3B follows the same trend as the BOSS models if the initial rovibrational state is changed, while the SRP-SCM does not. The broadening effect of the SRP-SCM is in general bigger than that of the SRP48-SCM3B.

The differences between the SRP-SCM and SRP48-SCM3B PESs of the broadening behaviour are hard to attribute to differences in DFT methods used, because the SRP-BOSS PES has the same behaviour as both SRP48 PESs with respect to this behaviour. There are three possible explanations for the difference between the SCMs. First of all the SRP48-SCM3B is fitted to almost 100 times more DFT configurations and also includes displacements of two surface atoms. Secondly, the coupling potential used in the SRP-SCM had a short cut-off in the H-Cu distance that prevented almost all contributions due to second layer displacements. It is known from the work of Bonfanti et al. [40] that the second layer displacements are very important for the

barrier heights. Finally there are H-H-Cu three-body terms included in the SRP48-SCM3B which are, as argued before, not negligible and are not included in the purely additive and pair-potential based SRP-SCM.

3.3.5   Comparing with AIMD and Experimental Results

When comparing the computed reaction probabilities from the BOSS model and SCM with results from AIMD [10] in figures 3.7a, b and c, there is a very good agreement across all incidence energies. This was to be expected as the SCM accurately reproduces the DFT used directly by AIMD. Differences are attributed to statistical errors due to the small amount of trajectories in AIMD, the periodicity of the surface displacements in AIMD, the relatively large time step in AIMD, the lack of energy exchange with the lattice with the SCM, and deviation of the SCM from DFT (42.7 meV RMSE). The reaction probability curves can be considered to be equivalent, which is extremely useful because it allows to select the correct DFT functional by comparing to experiments at elevated surface temperature using the SCM method. This is orders of magnitude computationally cheaper than AIMD. Figure 8 in Ref. [10] shows that essentially no desorbed molecules with a COM kinetic energy higher than 0.7 eV are measured during the experiment. Therefore only experimental results up to an indicence energy of 0.7 eV are considered for determining the accuracy of the theoretical models. With that in mind, the rotational and vibrational excited states, shown in figure 3.7b and c respectively, are reproduced very well by the theory. The rovibrational ground state, in figure 3.7a, on the other hand is not. This can be understood due the (v=0, J=0) state being much more sensitive to the shape of the PES around and towards the barrier rather than only the dynamical barrier height as discussed before. Similar to the argument on the accuracy of the SCM fit, an argument can be made here that further improvements in the dynamical model will only lead to a better accuracy when a more accurate DFT functional is found.

3.3.6 Initial Rovibrational State Dependence of the Reaction Probability

The computed reaction probabilities have been fitted using a generalized logistics function (GLF) [10] for all available rovibrational states. There are two important parameters from this fit, the inflection point (E_0) and the width of the curve. The inflection point is where the growth of the reaction probability first starts to decrease, which would be the energy at which the reaction probability is half of its maximum, if the reaction probability would be symmetrical with respect to the inflection point. There is however, a small deviation from this symmetry. Note that there are several different definitions of E_0 in literature, depending on the chosen fitting function, and that should be considered when comparing E_0 values from this work. The width is a measure of how broad the reaction probability curve is and is known to increase when taking into account surface temperature effect [10, 14]. I was not able to compute the uncertainties in the fitted E_0 and width parameters. Comparison with AIMD and experimental results remain difficult. For AIMD, the limited number of data points in incidence energy, due to the high computational effort, limits the fitting quality of the GLF. On the other hand, the GLF fits to experiments are based on time-of-flight (ToF) measurements of desorption experiments that are subsequently converted to reaction probabilities making use of detailed balance. Here the absolute saturation values are obtained from other molecular beam experiments. The consequences of fitting experimental results in such a way and comparing with theory have recently been discussed [41]. Figure 3.8a and b show the fitted E_0 parameters for v=0 and v=1 at increasing J. For all rovibrational states, the SRP-BOSS and SRP48-BOSS are in very close agreement, even though there is a small difference between the two PESs as discussed above. While the SRP-SCM predicts the same E_0 as the two BOSS models for J larger than 6, both for v=0 and v=1, and a higher E_0 at lower J, the SRP48-SCM3B predicts lower E_0 values except for v=1 and J=0 or J=1. For v=0 the experimental and AIMD results are in reasonable agreement while for v=1 there is a discrepancy between experimental and all theoretical results for J smaller than 3. It is not clear whether

this discrepancy is due to a failure of the theoretical models or because of the way the experimental results have been fitted. On the other hand, the width parameters in figures 3.8c and d show a large dependence on which SCM was used. The width parameters for both SRP-BOSS and SRP48-BOSS are between 0.1 and 0.18 eV and very similar. Including the SCM then increases the width, by approximately 0.05 eV in the case of SRP48 and 0.1 eV in the case of SRP. The AIMD results are in agreement with the increased width of the SRP48-SCM3B while the SRP-SCM predicts a larger increase in the width. While there is a good agreement between the experimental results and the SRP-SCM for v=0, it is very unlikely that this is due to the quality of the fit, considering the fact that AIMD is not able to reproduce the large widths found in the experiment. Overall, the new SRP48-SCM3B accurately reproduces AIMD results based on the fitted E_0 and width parameters.

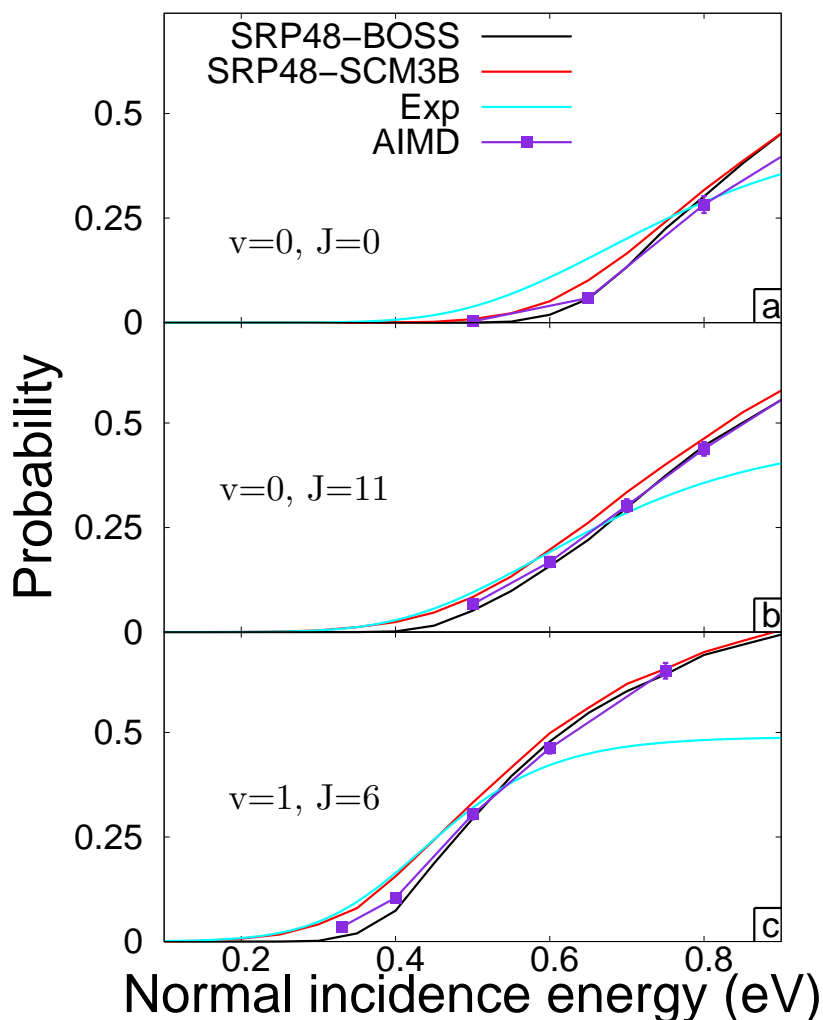Figure 3.7: State-specific reaction probabilities are shown as a function of incidence energy at normal incidence for SRP48-BOSS (black), SRP48-SCM3B (red), AIMD with SRP48 from Ref. [10] (purple) while a fit to the time-of-flight data of experimental results taken from Ref. [10] are shown in cyan. (a), (b) and (c) show the (v=0, J=0), (v=0,J=11) and (v=1,J=6) rovibrational state-specific reaction probabilities respectively.

3
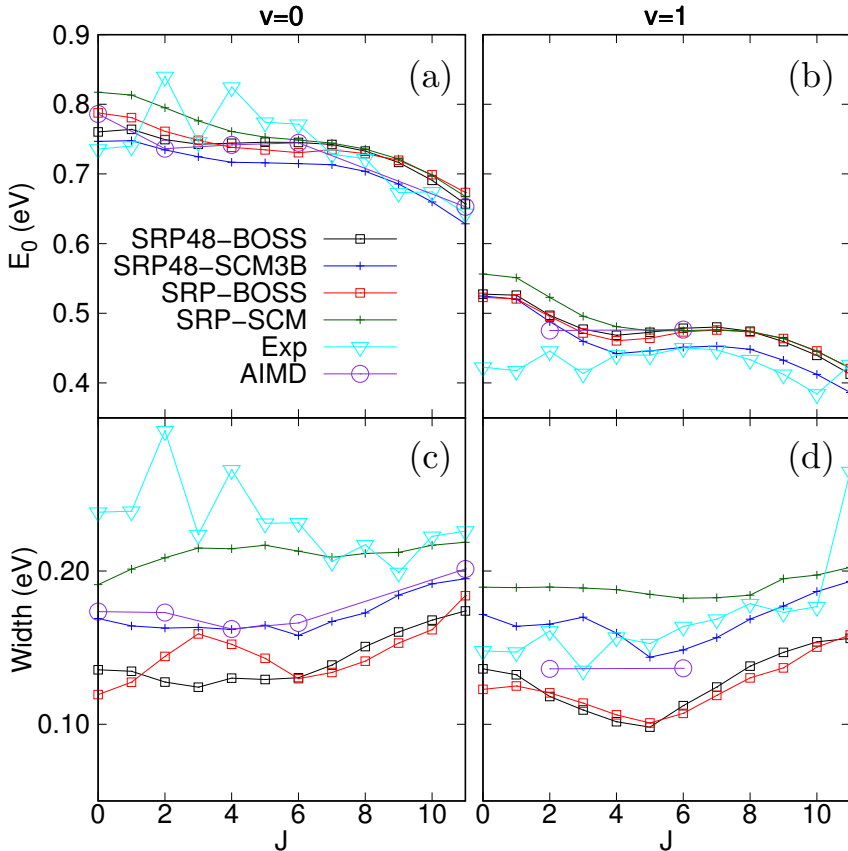
Figure 3.8: (a) and (b) show the fitted inflection point E_0 as a function of the rotational state J for vibrational state v=0 and v=1 respectively. (c) and (d) show the fitted width as a function of the rotational state J for vibrational state v=0 and v=1 respectively. The black and blue curves are obtained by fitting state-specific reaction probabilities, which were presented in this chapter, for SRP48-BOSS and SRP48-SCM3B respectively. Red and green curves are likewise obtained by refitting the data from Ref. [14] using the GLF. The cyan triangles and purple circles are obtained from Ref. [10] where the experimental (cyan triangles) results are obtained by fitting state-specific time-of-flight data and the AIMD (purple circles) results are obtained by fitting state-specific reaction probabilities.

3.4 Conclusions

A new coupling potential has been fitted for H_2 on Cu(111) within the SCM framework based on the SRP48 density functional using the same setup as AIMD calculations [10]. A large database of coupling potentials has been constructed for H_2 on Cu(111) at several high symmetry sites for a large amount of surface displacements. Included are configurations with two surface displacements, capturing the H-Cu-Cu three-body interactions which were found to have a negligible non-additivity. In contrast, configurations corresponding to one surface displacements and variable H_2 bond distance, describing the H-H-Cu three-body interactions, show a large non-additivity and can therefore not be described accurately using the two-body SCM. The functional form of the coupling potential has thus been extended to have a H_2 bond distance dependence of the Rydberg parameters, including H-H-Cu three-body interactions explicitly. Simulations of state-specific desorption experiments using the BOSS model show that the SRP and SRP48 PES are essentially identical, except for the reaction and scattering of rovibrational ground-state H_2 even though both functionals were constructed to reproduce the same molecular beam experiments. The differences between the PESs could not be accounted for by the barrier heights, extrinsic curvature of the MEP or zero point vibrational energy but are instead attributed to the intrinsic curvature of the PES along the MEP. Using the newly developed SCM based on the SRP48 AIMD and experimental results were succesfully reproduced and consequently the SCM can be a good substitute for AIMD in the case of H_2 on Cu(111). For heavier molecules on metal surfaces, where surface motion can be important and the SCM may not be suitable (due to the increased amount of expected energy exchange with the surface), it will be interesting to use a strain potential to describe the PES of a clean surface using e.g. embedded atom potentials [42–45]. Combining this strain potential with the coupling potential yields a full dimensional PES that allows energy exchange with the surface.

3.A Comparison of Minimum Energy Paths of H_2 on Cu(111) for SRP and SRP48
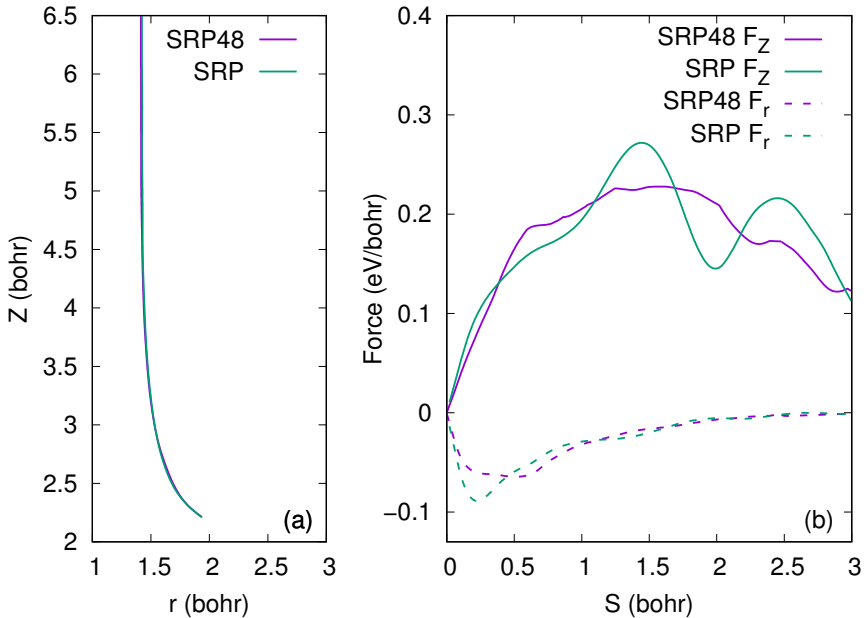
Figure 3.9: (a) shows the MEP until the barrier on the bridge site for the SRP48 and SRP PES in purple and green respectively. (b) shows the forces in Z (solid) and r (dashed) along the same MEP for SRP48 (purple) and SRP (green). S=0 bohr corresponds the barrier position.

In figure 3.9a, the minimum energy paths of both the SRP48 and SRP functional are shown to be essentially identical. In contrast, the forces along Z and r are slightly different in figure 3.9b. The difference in the force along Z between SRP and SRP48 for large S (far away from the transition state) are not important for the dynamics because there is only a small force along r and thus very little coupling between the two. On the other hand, the small differences at low S (below 1.5 Å) show that there indeed is a difference in intrinsic curvature around the minimum energy path even though the

minimum energy paths are essentially identical.

References

[1] P. Spiering, M. Wijzenbroek, and M. F. Somers. "An Improved Static Corrugation Model". In: *J. Chem. Phys.* 149 (2018), p. 234702. DOI: 10.1063/1.5058271.

[2] G. Ertl. "Reactions at Surfaces: From Atoms to Complexity (Nobel Lecture)". In: *Angew. Chem. Int. Edit.* 47 (2008), pp. 3524–3535. DOI: 10.1002/anie.200800480.

[3] T. Zambelli, J. V. Barth, J. Wintterlin, and G. Ertl. "Complex Pathways in Dissociative Adsorption of Oxygen on Platinum". In: *Nature* 390 (1997), pp. 495–497. DOI: 10.1038/37329.

[4] H. A. Michelsen, C. T. Rettner, and D. J. Auerbach. "On the Influence of Surface Temperature on Adsorption and Desorption in the D_2/Cu(111) System". In: *Surf. Sci.* 272 (1992), pp. 65–72. DOI: 10.1016/0039-6028(92)91422-8.

[5] H. A. Michelsen, C. T. Rettner, and D. J. Auerbach. "State-Specific Dynamics of D_2 Desorption from Cu(111): The Role of Molecular Rotational Motion in Activated Adsorption-Desorption Dynamics". In: *Phys. Rev. Lett.* 69 (1992), pp. 2678–2681. DOI: 10.1103/PhysRevLett.69.2678.

[6] C. T. Rettner, D. J. Auerbach, and H. A. Michelsen. "Observation of Direct Vibrational Excitation in Collisions of H_2 and D_2 with a Cu(111) Surface". In: *Phys. Rev. Lett.* 68 (1992), pp. 2547–2550. DOI: 10.1103/PhysRevLett.68.2547.

[7] C. T. Rettner, H. A. Michelsen, and D. J. Auerbach. "Determination of Quantum-State-Specific Gas—Surface Energy Transfer and Adsorption Probabilities as a Function of Kinetic Energy". In: *Chem. Phys.* 175 (1993), pp. 157–169. DOI: 10.1016/0301-0104(93)80235-2.

[8] C. T. Rettner, H. A. Michelsen, and D. J. Auerbach. "Quantum-State-Specific Dynamics of the Dissociative Adsorption and Associative Desorption of H_2 at a Cu(111) Surface". In: *J. Chem. Phys.* 102 (1995), pp. 4625–4641. DOI: 10.1063/1.469511.

[9] M. J. Murphy and A. Hodgson. "Adsorption and Desorption Dynamics of H2 and D2 on Cu(111): The Role of Surface Temperature and Evidence for Corrugation of the Dissociation Barrier". In: *J. Chem. Phys.* 108 (1998), pp. 4199–4211. DOI: 10.1063/1.475818.

3

[10]   F. Nattino, A. Genova, M. Guijt, A. S. Muzas, C. Díaz, et al. "Dissociation and Recombination of D_2 on Cu(111): Ab Initio Molecular Dynamics Calculations and Improved Analysis of Desorption Experiments". In: *J. Chem. Phys.* 141 (2014), p. 124705. DOI: 10.1063/1.4896058.

[11]   G.-J. Kroes. "Towards Chemically Accurate Simulation of Molecule-Surface Reactions". In: *Phys. Chem. Chem. Phys.* 14 (2012), pp. 14966–14981. DOI: 10.1039/C2CP42471A.

[12]   C. Díaz, E. Pijper, R. A. Olsen, H. F. Busnengo, D. J. Auerbach, et al. "Chemically Accurate Simulation of a Prototypical Surface Reaction: H2 Dissociation on Cu(111)". In: *Science* 326 (2009), pp. 832–834. DOI: 10.1126/science.1178722.

[13]   D. A. McCormack, G.-J. Kroes, E.-J. Baerends, and R. C. Mowrey. "Six-Dimensional Quantum Dynamics of Dissociation of Rotationally Excited H_2 on Cu(100)". In: *Faraday Discuss.* 110 (1998), pp. 267–285. DOI: 10.1039/A804213F.

[14]   M. Wijzenbroek and M. F. Somers. "Static Surface Temperature Effects on the Dissociation of H2 and D2 on Cu(111)". In: *J. Chem. Phys.* 137 (2012), p. 054703. DOI: 10.1063/1.4738956.

[15]   R. A. Olsen, H. F. Busnengo, A. Salin, M. F. Somers, G.-J. Kroes, et al. "Constructing Accurate Potential Energy Surfaces for a Diatomic Molecule Interacting with a Solid Surface: H_2+Pt(111) and H_2+Cu(100)". In: *J. Chem. Phys.* 116 (2002), pp. 3841–3855. DOI: 10.1063/1.1446852.

[16]   C. Díaz, R. A. Olsen, D. J. Auerbach, and G.-J. Kroes. "Six-Dimensional Dynamics Study of Reactive and Non Reactive Scattering of H2 from Cu(111) Using a Chemically Accurate Potential Energy Surface". In: *Phys. Chem. Chem. Phys.* 12 (2010), pp. 6499–6519. DOI: 10.1039/C001956A.

[17]   A. Mondal, M. Wijzenbroek, M. Bonfanti, C. Díaz, and G.-J. Kroes. "Thermal Lattice Expansion Effect on Reactive Scattering of H2 from Cu(111) at Ts = 925 K". In: *J. Phys. Chem. A* 117 (2013), pp. 8770–8781. DOI: 10.1021/jp4042183.

[18]   P. Spiering and J. Meyer. "Testing Electronic Friction Models: Vibrational De-Excitation in Scattering of H_2 and D_2 from Cu(111)". In: *J. Phys. Chem. Lett.* 9 (2018), pp. 1803–1808. DOI: 10.1021/acs.jpclett.7b03182.

[19]   A. C. Luntz and M. Persson. "How Adiabatic Is Activated Adsorption/Associative Desorption?" In: *J. Chem. Phys.* 123 (2005), p. 074704. DOI: 10.1063/1.2000249.

[20]   K. Shakouri, J. Behler, J. Meyer, and G.-J. Kroes. "Accurate Neural Network Description of Surface Phonons in Reactive Gas–Surface Dynamics: N_2 + Ru(0001)". In: *J. Phys. Chem. Lett.* 8 (2017), pp. 2131–2136. DOI: 10.1021/acs.jpclett.7b00784.

[21] J. Behler, S. Lorenz, and K. Reuter. "Representing Molecule-Surface Interactions with Symmetry-Adapted Neural Networks". In: *J. Chem. Phys.* 127 (2007), p. 014705. DOI: 10.1063/1.2746232.

[22] B. Kolb, X. Luo, X. Zhou, B. Jiang, and H. Guo. "High-Dimensional Atomistic Neural Network Potentials for Molecule–Surface Interactions: HCl Scattering from Au(111)". In: *J. Phys. Chem. Lett.* 8 (2017), pp. 666–672. DOI: 10.1021/acs.jpclett.6b02994.

[23] Y. Zhang and W. Yang. "Comment on "Generalized Gradient Approximation Made Simple"". In: *Phys. Rev. Lett.* 80 (1998), pp. 890–890. DOI: 10.1103/PhysRevLett.80.890.

[24] B. Hammer, L. B. Hansen, and J. K. Nørskov. "Improved Adsorption Energetics within Density-Functional Theory Using Revised Perdew-Burke-Ernzerhof Functionals". In: *Phys. Rev. B* 59 (1999), pp. 7413–7421. DOI: 10.1103/PhysRevB.59.7413.

[25] G. Kresse and J. Hafner. "*Ab Initio* Molecular-Dynamics Simulation of the Liquid-Meta— Amorphous-Semiconductor Transition in Germanium". In: *Phys. Rev. B* 49 (1994), pp. 14251–14269. DOI: 10.1103/PhysRevB.49.14251.

[26] G. Kresse and J. Furthmüller. "Efficient Iterative Schemes for Ab Initio Total-Energy Calculations Using a Plane-Wave Basis Set". In: *Phys. Rev. B* 54 (1996), pp. 11169–11186. DOI: 10.1103/PhysRevB.54.11169.

[27] D. Vanderbilt. "Soft Self-Consistent Pseudopotentials in a Generalized Eigenvalue Formalism". In: *Phys. Rev. B* 41 (1990), pp. 7892–7895. DOI: 10.1103/PhysRevB.41.7892.

[28] C. C. Marston and G. G. Balint-Kurti. "The Fourier Grid Hamiltonian Method for Bound State Eigenvalues and Eigenfunctions". In: *J. Chem. Phys.* 91 (1989), pp. 3571–3576. DOI: 10.1063/1.456888.

[29] F. R. Kroeger and C. A. Swenson. "Absolute Linear Thermal-Expansion Measurements on Copper and Aluminum from 5 to 320 K". In: *J. Appl. Phys.* 48 (1977), pp. 853–864. DOI: 10.1063/1.323746.

[30] K. H. Chae, H. C. Lu, and T. Gustafsson. "Medium-Energy Ion-Scattering Study of the Temperature Dependence of the Structure of Cu(111)". In: *Phys. Rev. B* 54 (1996), pp. 14082–14086. DOI: 10.1103/PhysRevB.54.14082.

[31] V. F. Sears and S. A. Shelley. "DebyeFactor for Elemental Crystals". In: *Acta. Cryst. A* 47 (1991), pp. 441–446. DOI: 10.1107/S0108767391002970.

[32] J. Stoer and R. Bulirsch. *Introduction to Numerical Analysis.* New York: Springer-Verlag, 1980.

3

[33] S. Nave and B. Jackson. "Methane Dissociation on Ni(111): The Effects of Lattice Motion and Relaxation on Reactivity". In: *J. Chem. Phys.* 127 (2007), p. 224702. DOI: 10.1063/1.2800661.

[34] F. Battaglia and F. A. Gianturco. "Vibrational Relaxation of HF Colliding with Helium. A Coupled Quantum Treatment". In: *Chem. Phys.* 55 (1981), pp. 283–291. DOI: 10.1016/0301-0104(81)80264-9.

[35] M. C. van Hemert. "Potential Energy Surface for the Study of Inelastic Collisions between Nonrigid CO and H2". In: *J. Chem. Phys.* 78 (1983), pp. 2345–2354. DOI: 10.1063/1.445034.

[36] Y. Xiao, W. Dong, and H. F. Busnengo. "Reactive Force Fields for Surface Chemical Reactions: A Case Study with Hydrogen Dissociation on Pd Surfaces". In: *J. Chem. Phys.* 132 (2010), p. 014704. DOI: 10.1063/1.3265854.

[37] F. Nattino, C. Díaz, B. Jackson, and G.-J. Kroes. "Effect of Surface Motion on the Rotational Quadrupole Alignment Parameter of D_2 Reacting on Cu(111)". In: *Phys. Rev. Lett.* 108 (2012), p. 236104. DOI: 10.1103/PhysRevLett.108.236104.

[38] M. Wijzenbroek and G.-J. Kroes. "The Effect of the Exchange-Correlation Functional on H2 Dissociation on Ru(0001)". In: *J. Chem. Phys.* 140 (2014), p. 084702. DOI: 10.1063/1.4865946.

[39] R. D. Muino and H. F. Busnengo. *Dynamics of Gas-Surface Interactions: Atomic-Level Understanding of Scattering Processes at Surfaces*. Springer Series in Surface Sciences. Berlin Heidelberg: Springer-Verlag, 2013.

[40] M. Bonfanti, C. Díaz, M. F. Somers, and G.-J. Kroes. "Hydrogen Dissociation on Cu(111): The Influence of Lattice Motion. Part I". In: *Phys. Chem. Chem. Phys.* 13 (2011), pp. 4552–4561. DOI: 10.1039/C0CP01746A.

[41] S. Kaufmann, Q. Shuai, D. J. Auerbach, D. Schwarzer, and A. M. Wodtke. "Associative Desorption of Hydrogen Isotopologues from Copper Surfaces: Characterization of Two Reaction Mechanisms". In: *J. Chem. Phys.* 148 (2018), p. 194703. DOI: 10.1063/1.5025666.

[42] S. M. Foiles, M. I. Baskes, and M. S. Daw. "Embedded-Atom-Method Functions for the Fcc Metals Cu, Ag, Au, Ni, Pd, Pt, and Their Alloys". In: *Phys. Rev. B* 33 (1986), pp. 7983–7991. DOI: 10.1103/PhysRevB.33.7983.

[43] Y. Mishin, M. J. Mehl, D. A. Papaconstantopoulos, A. F. Voter, and J. D. Kress. "Structural Stability and Lattice Defects in Copper: Ab Initio, Tight-Binding, and Embedded-Atom Calculations". In: *Phys. Rev. B* 63 (2001), p. 224106. DOI: 10.1103/PhysRevB.63.224106.

[44]   B.-J. Lee, J.-H. Shim, and M. I. Baskes. "Semiempirical Atomic Potentials for the Fcc Metals Cu, Ag, Au, Ni, Pd, Pt, Al, and Pb Based on First and Second Nearest-Neighbor Modified Embedded Atom Method". In: *Phys. Rev. B* 68 (2003), p. 144112. DOI: 10.1103/PhysRevB.68.144112.

[45]   H. W. Sheng, M. J. Kramer, A. Cadien, T. Fujita, and M. W. Chen. "Highly Optimized Embedded-Atom-Method Potentials for Fourteen Fcc Metals". In: *Phys. Rev. B* 83 (2011), p. 134118. DOI: 10.1103/PhysRevB.83.134118.

3

Chapter 4

Testing Electronic Friction Models: Vibrational De-excitation in Scattering of H_2 and D_2 on Cu(111)

Abstract

At present, molecular dynamics with electronic friction (MDEF) is *the* workhorse model to go beyond the Born-Oppenheimer approximation in modeling dynamics of molecules at metal surfaces. Concomitant friction coefficients can be calculated with either the local density friction approximation (LDFA) or orbital-dependent friction (ODF) which – unlike LDFA – accounts for anisotropy while relying on other approximations. Due to the computational cost of ODF, extensive high-dimensional MDEF trajectory calculations of experimentally measurable observables have hitherto only been performed based on LDFA. In order to overcome this limitation a continuous neural-network-based representation has been constructed for the scattering of vibrationally excited H_2 and D_2 from Cu(111). An up to three times higher vibrational de-excitation probabilities is predicted with ODF compared to LDFA. These results indicate that anisotropic electronic friction can be important for specific molecular observables. Future experiments can test for this "fingerprint" of different approximations underlying state-of-the-art MDEF.

4.1   Introduction

The motion of atomic and molecular adsorbates on metal surfaces underlies every elementary reaction steps in heterogeneous catalysis. Due to the absence of an energy gap between valence and conduction band electrons, these motions can result in the excitation of electron-hole pairs (ehps) and thus violate the Born-Oppenheimer approximation [2–4]. A growing number of experiments points to the importance of this non-adiabatic energy loss channel [5]. On the other hand, the development of suitable theoretical models to account for these non-adiabatic effects is still an ongoing process [6–10]. For systems with weak non-adiabatic coupling, molecular dynamics with electronic friction (MDEF)[11] is currently the most popular approach [12]. MDEF relies on a potential energy surface (PES) nowadays typically obtained from density functional theory (DFT)[4], and accounts for the effects of the ehps on the motion of the nuclei by electronic friction coefficients [11]. One state-of-the-art technique for cal-

culating these coefficients as functions of the adsorbate positions relies on mapping to an atom-in-jellium model for which only the surface electron density is considered (local density friction approximation, LDFA[13, 14]). Alternatively, the electronic states of the molecule-surface system can be taken into account (orbital-dependent friction, ODF[11, 15]). For the inelastic scattering of H atoms from Au(111), millions of MDEF trajectories based on a high-dimensional PES[16] and local density friction approximation (LDFA) have recently been demonstrated to yield accurate scattering probabilities in excellent agreement with experimental data [17].

The situation is quite different for molecules. Due to its combination with the independent atom approximation, the LDFA completely neglects any molecular effects [13]. Orbital-dependent friction (ODF) on the other hand accounts for the anisotropic tensorial character of friction coefficients on corrugated metal surfaces and along adsorbate-internal bonds [18–20], which is why ODF has been argued to be "theoretically" more accurate for (diatomic) molecules [21]. However, this discussion [13, 21, 22] has still remained inconclusive, because an evaluation of ODF comes at very high computational costs. Consequently, extensive MDEF trajectory calculations for molecules including all relevant degrees of freedom (DOF) can be easily performed with LDFA[12, 13], whereas only two molecular DOF have so far been included for ODF[23]. The very recent on-the-fly evaluation of ODF within *ab initio* molecular dynamics by [20] is an important step, but the less than 20 calculated trajectories make direct validation via molecular beam experiments impossible. Modeling the non-adiabatic contribution to vibrational lifetimes of molecules adsorbed on metal surfaces on the other hand does not require such extensive statistical averaging [24, 25]. The most recent implementations of LDFA and ODF both yield results that agree with experimental data within the error bars [26, 27]. Furthermore, Novko *et al.* have shown recently in this context [28] that the numerical evaluation of friction tensors within ODF [20, 27] effectively includes potentially spurious electronic memory effects with unclear consequences for MDEF[29]. Given this situation, theoretical understanding and modeling relying on MDEF faces an important question: Is the molecular anisotropy as described by ODF important for any observables that can be validated by high-precision molecular beam

experiments like for atoms [17]?

The work in this chapter provides an answer to this question using H_2 and D_2 on Cu(111). For this system, the weak non-adiabatic coupling as well as static surface approximation are well justified [30–32], and an accurate DFT-based PES relying on the semi-empirically constructed specific reaction parameter (SRP) exchange-correlation functional is available [33, 34]. A six-dimensional neural-network-based continuous representation of ODF has been constructed that allows for extensive MDEF trajectory calculations on equal footing with LDFA. While dissociative sticking probabilities are hardly affected in general and by the type of electronic friction coefficients used, vibrational de-excitation probabilities are argued to be a "fingerprint", which can be used to distinguish and validate LDFA and ODF in future experiments, in this chapter.

4.2 Methods

In this section an extension of Chap. 2 is given for the methods used specifically in this chapter.

4.2.1 Molecular Dynamics with Electronic Friction and the Potential Energy Surface

Quasi-classical trajectory calculations [33] within MDEF rely on a generalized Langevin equation [11]

$$m_i \frac{d^2 R_{i\alpha}}{dt^2} = -\frac{\partial V(\mathbf{R})}{\partial R_{i\alpha}} - \underbrace{\sum_{j=1}^{N} \sum_{\beta=1}^{3} \eta_{i\alpha j\beta} \dot{R}_{j\beta}(\mathbf{R})}_{F_{i\alpha}^{\text{fric}}(\mathbf{R})} + \mathcal{F}_{i\alpha}(t), \qquad (4.1)$$

where i, j indicate atoms and α, β Cartesian coordinates. Atomic masses and positions are denoted by m_i and $\mathbf{R}_i$, respectively. For a H_2 or D_2 molecule on a static surface, the total number of moving atoms N is two resulting in six DOF. In addition to the forces from the PES $-\frac{\partial V(\mathbf{R})}{\partial R_{i\alpha}}$, which yield the adiabatic dynamics, non-adiabatic effects on the nuclear dynamics originate from electronic friction forces $F_{i\alpha}^{\text{fric}}(\mathbf{R})$ and thermal
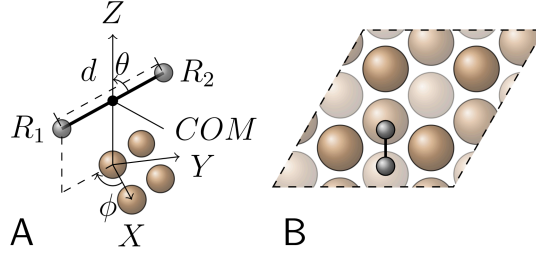
Figure 4.1: A) Molecular coordinate system denoting the center of mass positions (X, Y, Z), bond length d as well as spherical orientation (θ, ϕ). B) Top view of a reference configuration with $X = \frac{1}{2}a$, $Y = 0$ and $\theta_0 = \phi_0 = 90°$ from the minimum energy reaction path for dissociative chemisorption over the bridge site [35], where a denotes the surface lattice constant. Cu atoms in the first, second and third layer are depicted by increasing transparence. Note that $X, Y, Z = 0$ corresponds to the position of a Cu atom in the surface plane (top site).

white noise $\mathcal{F}_{i\alpha}(t)$, respectively. In this work, $V(\mathbf{R})$ is mainly taken to be the static surface PES based on the SRP48 exchange-correlation functional from Ref. [34], but dynamics calculations have also been performed and compared with the PW91-PES from earlier work [35]. The friction forces are linear in nuclear velocities $\dot{R}_{j\beta}$ and are in general given by a symmetric 6×6 friction tensor $\eta_{i\alpha j\beta}(\mathbf{R})$, which consists of 21 independent elements each depending on six nuclear coordinates. These coordinates can be Cartesian $\mathbf{R} = (\mathbf{R}_1, \mathbf{R}_2)$ or expressed in the center-of-mass-centered spherical coordinate system $\mathbf{R} = (X, Y, Zd, \theta, \phi)$, which is commonly used for diatomics and described by Fig. 4.1 A.

4.2.2 Orbital-Dependent Friction and Density Functional Theory

Within ODF these 21 friction coefficients are obtained according to a Fermi-golden-rule-like expression resulting from time-dependent perturbation theory, which can be written in the quasi-static limit as [11, 25, 27, 36]

$$\eta_{i\alpha j\beta}^{\mathrm{ODF}}(\mathbf{R}) = 2\pi\hbar \sum_{\mathbf{k}ab} g_{\mathbf{k}ab}^{i\alpha}(\mathbf{R})^* \cdot g_{\mathbf{k}ab}^{j\beta}(\mathbf{R})\, \delta(\epsilon_{\mathbf{k}a} - \epsilon_{\mathrm{F}})\delta(\epsilon_{\mathbf{k}b} - \epsilon_{\mathrm{F}}) \,. \tag{4.2}$$

The electron phonon matrix elements $g_{\mathbf{k}ab}^{i\alpha}$ describe the non-adiabatic coupling between two electronic states of the molecule at the metal surface with band indices a and b at wave vector $\mathbf{k}$, due to the motion of (adsorbate) atom i along direction α. In general, the ODF tensor can have different diagonal elements even for the same atom. This anisotropy yields very different friction forces when the atoms move (with the same velocity) in different directions. Its generally non-zero off-diagonal elements are responsible for coupling the motion in different directions and between both atoms in a way that is not accounted for by the PES. In particular, this can lead to a strong damping of the molecular stretch vibration of a diatomic molecule and thus a pronounced molecular anisotropy [20, 21, 23].

4.2.3 Neural Network Interpolation

In order to use the so-calculated $\eta_{i\alpha j\beta}^{\mathrm{ODF}}(\mathbf{R})$ in MDEF trajectory calculations of generic experimentally measurable observables, a continuous representation of this 6×6 tensor is required that can be evaluated at low computational cost. We have designed such a representation based on a symmetry-adapted neural network fit that is described briefly in Sec. 4.B and extensively in Chap. 6.

4.2.4 Local Density Friction Approximation

Within LDFA friction coefficients for hydrogen atoms $\eta^{\mathrm{H}}(\rho)$ are obtained from a spherical atom-in-jellium model with background density ρ, which is solved via density functional theory at the level of the local density [37] or generalized gradient approximation [38]. Mapping of the actual surface problem is accomplished by taking the electron density of the bare surface (without the molecule) at each atom's position $\rho(\mathbf{R}_i)$ as background density of the jellium [13]. This independent-atom approximation (IAA) results in electronic friction coefficients that are isotropic for each atom and depend on its own three coordinates alone. In Cartesian coordinates only diagonal elements of the friction tensor are non-zero,

$$\eta_{i\alpha j\beta}^{\mathrm{LDFA}}(\mathbf{R}) = \eta^{\mathrm{H}}(\rho(\mathbf{R}_i))\delta_{\alpha\beta}\delta_{ij} \tag{4.3}$$

A continuous representation of $\eta^{\mathrm{LDFA}}_{i\alpha j\beta}(\mathbf{R})$ for extensive MDEF trajectory calculations can be easily constructed [13, 39].

4.2.5 Isotropicalized Electronic Friction Tensor

Going beyond the IAA within LDFA is possible for example by determining the background electron density using an atoms-in-molecules technique (LDFA-AIM) [26]. However, this approach does not lift the isotropy, and as detailed in Sec. 4.A, cannot be applied to H_2 and D_2 molecules. The other way round, isotropic friction can be constructed from ODF, by neglecting the coupling between different directions and atoms plus averaging the remaining (generally anisotropic) friction over different directions

$$\eta^{\mathrm{ODF-iso}}_{i\alpha j\beta}(\mathbf{R}) = \frac{1}{3}\sum_{\gamma} \eta^{\mathrm{ODF}}_{i\gamma j\gamma}(\mathbf{R})\delta_{ij}\delta_{\alpha\beta}\,. \tag{4.4}$$

This ODF-iso allows disentangling the influence of anisotropy from the very different electronic structure inherent to ODF and LDFA.

4.3 Results

4.3.1 Friction Coefficients

Fig. 4.2 A-C shows η_{Zd}, η_{dd} and η_{ZZ}, respectively, as obtained from equations 4.2-4.4 along the minimum energy reaction path for dissociative chemisorption over the bridge site as depicted in Fig. 4.2 D and Fig. 4.1 B. In particular the focus here is on these three particular friction coefficients, in order to compare with the earlier two-dimensional ODF calculations [21, 23]. The agreement is quite good except for some differences close to the transition state for η^{ODF}_{ZZ}. As the molecule approaches the surface, each model yields increasing friction for the six diagonal elements of the friction tensor, and the absolute values of the off-diagonal elements increase likewise in case of ODF. Furthermore, ODF directly reflects the strong rearrangement of (Kohn-Sham) orbitals when approaching the dissociation barrier by significantly higher friction along the molecular bond (and thus reaction) coordinate, resulting in $\eta^{\mathrm{ODF}}_{dd} \approx 3\eta^{\mathrm{LDFA}}_{dd}$ at

4

the transition state – in agreement with earlier work [21]. For the observables calculated below, friction beyond the dissociation barrier is not relevant. Quite remarkably, $\eta_{dd}^{\mathrm{ODF-iso}}$ ($\eta_{ZZ}^{\mathrm{ODF-iso}}$) and $\eta_{dd}^{\mathrm{LDFA}}$ ($\eta_{ZZ}^{\mathrm{LDFA}}$) are almost identical up to the transition state – and thus much more alike than what has originally been found for the diffusion of H atoms on Pd(100) [18, 40].

4.3.2 Dynamics

In order to study the effect of the different friction models on actual experimental observables, MDEF calculations are performed according to the quasi-classical trajectory method [29]. In view of the short interaction time of the molecules with the Cu(111) surface during all simulated trajectories, the fluctuating forces in Equation 4.1 are neglected.

4.3.3 Dissociative Chemisorption Probability

Fig. 4.3 shows the results for the dissociative chemisorption probability S_0 for both H_2 and D_2 molecular beams based on the SRP48-PES. Due to the construction of the latter [33, 34], already the adiabatic calculations yield good agreement with the experimental data [41, 42]. Inclusion of electronic friction reduces S_0, leading to even better agreement with the experimental data, in particular at high incidence energies. The reduction is strongest for ODF and weaker for LDFA and ODF-iso, which are very similar to each other. It can be rationalized by the differences of the friction models for the friction η_{dd} along reaction coordinate close to the dissociation barrier (see Fig. 4.2 B). This effect of η_{dd}^{ODF} on S_0 for H_2 and D_2 on Cu(111) has not been reported for two-dimensional ODF calculations [23]. Consequently, a high-dimensional treatment of ODF in MDEF, on an equal footing with LDFA [22], is important. However, the overall small effect of electronic friction on S_0 makes this not an optimal observable for experimental validation of the different friction models.
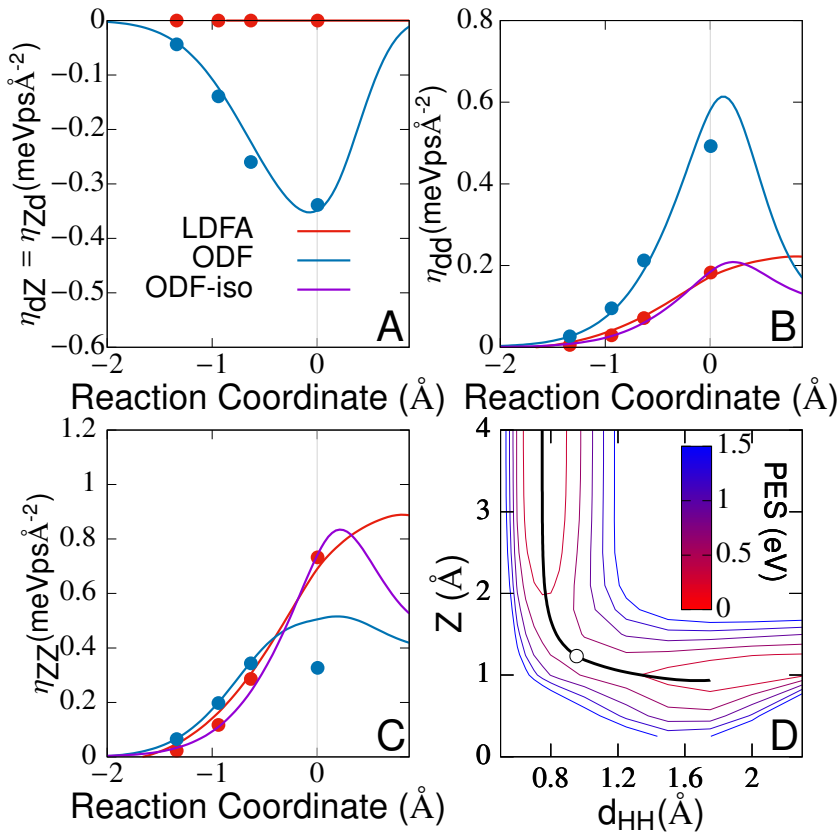
Figure 4.2: A-C show η_{dZ}, η_{dd} and η_{ZZ} in the molecular coordinate system (see Fig. 4.1 A), respectively, along the minimum energy reaction path for dissociative chemisorption over the bridge site (see Fig. 4.1 B) as depicted in D together with the corresponding two-dimensional PES cut. The blue, red and purple lines indicate the continuous representation from this chapter for ODF, LDFA and ODF-iso, respectively, as obtained from equations 4.2-4.4. Blue (red) dots show the ODF (LDFA) results from previous work of Luntz *et al.* [21, 23], and the reaction coordinate is defined in the same way as in that work. The barrier and thus the transition state for dissociation is located at the vertical gray line in A-C (0 Å) and indicated by the empty circle in D. Negative numbers up to transition state denote the approach from the gas-phase (i.e. decreasing heights Z above the surface).
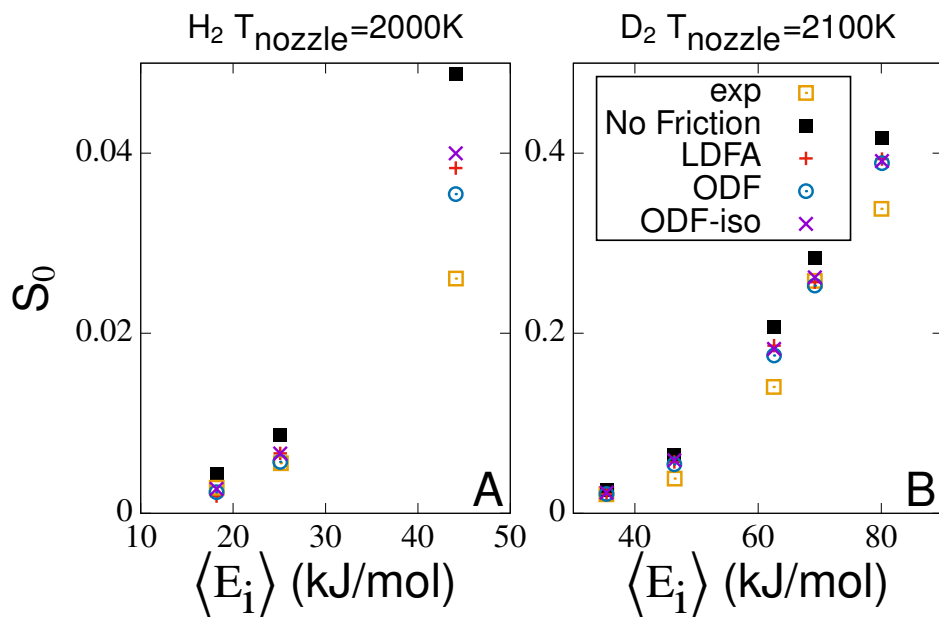
Figure 4.3: A(B) Calculated reaction probabilities S_0 based on the SRP48-PES for dissociative chemisorption of H_2 (D_2) molecular beams as a function of average normal incidence energy $\langle E_i \rangle$ for the indicated nozzle temperatures T_{nozzle} in comparison to experimental data (brown unfilled squares) from Ref. [41] (Ref. [42]). The calculations are adiabatic (filled black squares) or employ the LDFA (red plusses), ODF (blue circles) and ODF-iso (purple crosses) model for the electronic friction coefficients.

4.3.4 Vibrational De-Excitation

In contrast to the dissociative chemisorption probabilities, the vibrational de-excitation probabilities $P_{\text{transition}}$ clearly yield a distinguishable difference between LDFA and ODF. $P_{\text{transition}}$ is calculated as functions of incidence energy E_{i} from the scattered trajectories by a conventional binning procedure based on 50000 MDEF trajectories.. The concomitant average gain in translational energy $\langle \Delta E_{\text{trans}} \rangle$ is calculated from the final center-of-mass velocities. As detailed in the supporting information, the error bars reflect the error due to statistical sampling of the initial conditions. Only by employing the newly developped continuous representation to compute a large amount of trajectories was it possible to reduce these errors so that the different electronic friction models can be distinguished. The discussion henceforth is focussed on de-excitation from vibrational state $\nu = 2, J = 1(2)$ to $\nu = 1, J = 1(2)$ for H$_2$ (D$_2$), respectively, as shown in Fig. 4.4. Unlike for other vibrational transitions [43], for this transition the results are not only qualitatively but even almost quantitatively identical to corresponding results obtained with the PW91-PES (see Sec. 4.D).

At low incidence energies, with increasing E_{i} more and more molecules come close enough to the surface so that the curvature of the PES and electronic friction lead to an increase of $P_{\text{transition}}$. Both effects are additive and result in de-excitation probabilities that are up to 6(2) times larger for H$_2$ (Fig. 4.4C) and up to 3(2) times larger for D$_2$ with ODF(LDFA), respectively (Fig. 4.4D). At high incidence energies, the dissociation channel (see Fig. 4.3) becomes more effective, which is why $P_{\text{transition}}$ decreases again in all cases. For the adiabatic simulations on the static surface, $\langle \Delta E_{\text{trans}} \rangle$ is equal to the rovibrational energy loss of one vibrational quantum and thus by about $\sqrt{(2)}$ larger for H$_2$ than for D$_2$(Fig. 4.4A and B). Electronic friction reduces the energy gain. The reduction is almost twice as large for ODF compared to LDFA. The fact that it does not not very strongly depend on E_{i} for the energy range considered here suggests that it is dominated by η_{dd} and thus directly reflects the differences observed along the minimum energy path depicted in Fig. 4.2. Consequently, when comparing MDEF with other non-adiabatic models [44–46] for vibrational de-excitation, the new MDEF results suggest that it is crucial to also take into account whether the friction
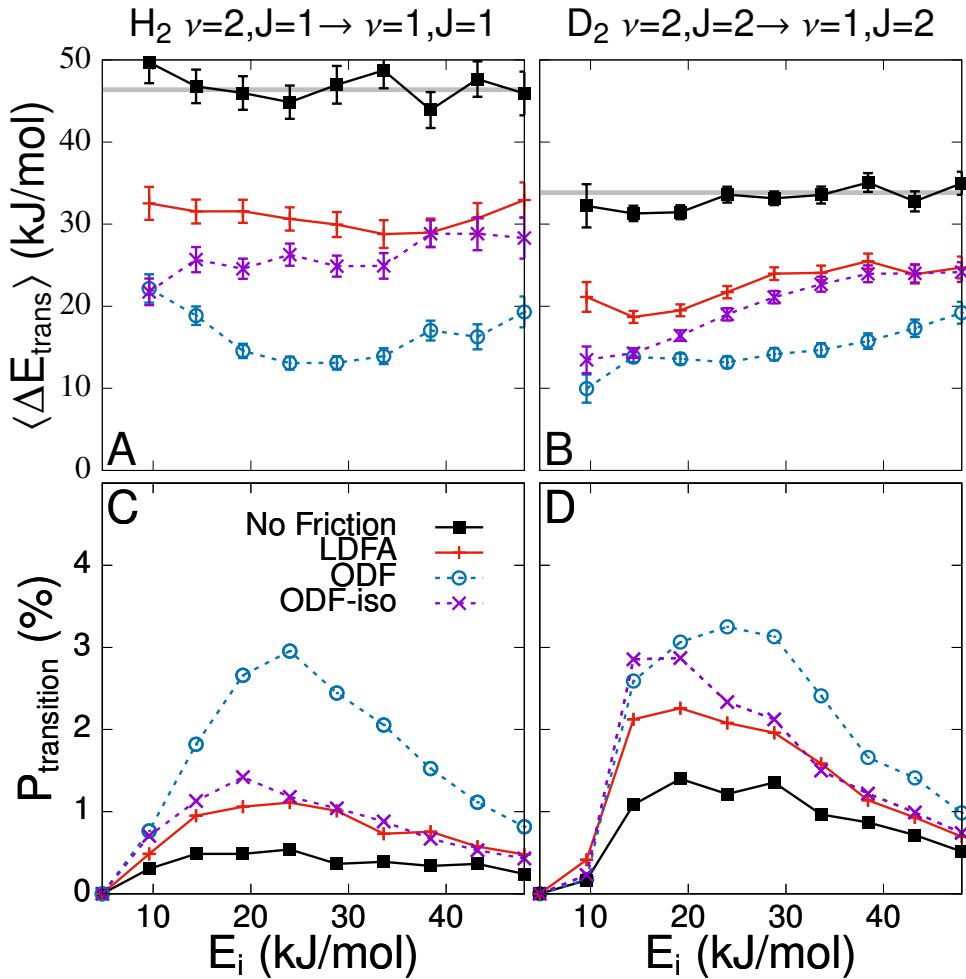
Figure 4.4: Vibrational de-excitation probabilities $P_{\text{transition}}$ (lower row) and concomitant average gain in translational energy $\langle \Delta E_{\text{trans}} \rangle$ (upper row) as a function of normal incidence energy E_i for state-to-state scattering using the SRP48-PES. Panels A,C (B,D) are for the transition from the rovibrational state $\nu = 2, J = 1(2)$ to $\nu = 1, J = 1(2)$ for H_2 (D_2). Shown are results from adiabatic calculations (filled black squares), as well as those including electronic friction according to the LDFA (red plusses), ODF (blue circles) or ODF-iso (purple crosses) models. The error bars indicate the error due to statistical sampling as described in detail in Sec. 4.C.

coefficients include any molecular anisotropy. Unfortunately, since molecular beam experiments for this system have hitherto focused on rovibrational excitation rather than de-excitation [47–49], experimental verification of this effect is still pending.

Although ODF-iso inherits the spurious memory effects as well as going beyond the independent atom approximation from ODF, quite remarkably, for $E_i > 15(20)$ kJ/mol for H_2 (D_2), results obtained with ODF-iso are almost identical to LDFA. That means that (at least in this energy range) these do not affect the dynamics and the molecular anisotropy is the most important difference. [50] If this can be experimentally validated, it would greatly encourage future theoretical work to develop extensions to LDFA that can account for this anisotropy.

4.4   Conclusions & Outlook

In summary, I have obtained different observables for H_2 and D_2 on Cu(111) from extensive MDEF trajectory calculations for the first time using full-dimensional friction tensors based on both LDFA *and* ODF. The molecular anisotropy as described by ODF and absent from LDFA leads to strongly enhanced friction for motion along the molecular axis when the molecules are close to the surface. The dissociative sticking probability is almost negligibly reduced compared to adiabatic simulations. The effect is slightly stronger for ODF compared to LDFA and improves the agreement with experimental data in both cases. For the state-to-state scattering of vibrationally excited molecules (from $\nu = 2, J = 1(2)$ to $\nu = 1, J = 1(2)$ for H_2 (D_2)), the newly developed MDEF model predicts up to six (two) times larger vibrational de-excitation probabilities with ODF (LDFA) compared to adiabatic simulations. Remarkably, isotropicalization of ODF yields results almost identical to LDFA for incidence energies larger than $15(20)$ kJ/mol for H_2 (D_2). The predicted differences between the vibrational de-excitation probabilities are a "fingerprint" of the molecular anisotropy as described by ODF. Recently suggested techniques to prepare H_2 molecular beams with $1 \leq \nu \leq 4$ [51] should allow testing for this "fingerprint". This would provide unprecedented insights into the accuracy of state-of-the-art electronic friction models for molecules and

allow analyzing the importance of concomitant approximations.

4.5 Computational Details

The electron phonon matrix elements $g_{\mathbf{k}ab}^{i\alpha} = \langle \phi_{\mathbf{k}a} | \frac{\partial v_{\mathrm{KS}}}{\partial \mathbf{R}_{i\alpha}} | \phi_{\mathbf{k}b} \rangle$ in Equation 4.2 are obtained from the change of Kohn-Sham potential $\frac{\partial v_{\mathrm{KS}}}{\partial \mathbf{R}_{i\alpha}}$ with respect to nuclear coordinate $\mathbf{R}_{i\alpha}$, which is obtained from density functional perturbation theory (DFPT) [52] employing the PW91 [53] exchange-correlation functional as implemented in the QUANTUM ESPRESSO package[54]. Surfaces are modeled by 2×2 Cu(111) slabs with 4 layers and 10 Å of vacuum. A planewave cut-off energy of 816 eV is used, together with ONCV pseudopotentials [55] from the SG15 [56] library and an 18x18 $\mathbf{k}$-point grid. These settings reproduce the PW91-PES from Ref. [35] up to a few meV. They also enable an accurate evaluation of the sum over electronic states in Equation 4.2 at the Fermi level using an equivalent Gaussian envelope technique to broaden the δ-function with a width of 0.6 eV as suggested in Ref. [27]. It should be noted here that this implies the possible presence of spurious electronic memory effects as argued in Ref. [28] and that care should be taken as this broadening can be system specific.

The neural network fits for the 21 independent elements of $\eta_{i\alpha j\beta}^{\mathrm{ODF}}(\mathbf{R})$ are based on ≈ 30000 ODF coefficients obtained from DFT calculations on the same 7 lateral sites that have been used to construct the SRP48-PES [34]. LDFA coefficients are obtained by extracting the background electron density $\rho(\mathbf{R}_i)$ from a DFT calculation with same the computational setup as described above. Employing the functional form for $\eta^{\mathrm{H}}(\rho)$ suggested in Ref. [39] a grid (in $\mathbf{R}_i$) of friction coefficients is obtained and used to construct a three-dimensional neural network interpolations for $\eta^{\mathrm{H}}(\rho(\mathbf{R}_i))$ based on the symmetry-adapted coordinates [57, 58] in order to obtain a continuous representation of $\eta_{i\alpha j\beta}^{\mathrm{LDFA}}(\mathbf{R})$.

4.A   LDFA "Atoms in Molecules" for H_2 and D_2

Rittmeyer *et al.* have suggested an extension of the local density friction approximation (LDFA) going beyond the independent atom approximation [26], accounting for molecular properties by means of the atoms-in-molecules (AIM) technique according to Hirshfeld [59]. The authors have used this LDFA-AIM scheme very successfully to model the non-adiabatic vibrational damping of CO adsorbed on Cu(100) and Pt(111). However, this scheme cannot be applied to the adsorption or scattering dynamics of H_2 or D_2 on any metal surface, because it yields unrealistic non-zero friction coefficients for these two molecules in the gas phase as illustrated in Fig. 4.5 (an extension of Fig. 4.2).

This can be understood by having a closer look at how the embedding density $\rho_{\mathrm{emb},i}^{\mathrm{AIM}}$ for an atom at positions $\mathbf{R}_i$ (i.e. background density for the atoms-in-jellium model underlying the LDFA [13]) is constructed [26]:

$$\rho_{\mathrm{emb},i}^{\mathrm{AIM}} = \left[1 - w_i^{\mathrm{Hirshfeld}}(\mathbf{R}_i)\right] \cdot \rho^{\mathrm{SCF}}(\mathbf{R}_i) \ . \tag{4.5}$$

Here ρ^{SCF} is the self-consistent density from the DFT calculation of the surface including the molecule. The Hirshfeld weight is defined based on electron densities of N isolated atoms ρ_i^{atom} at the same positions $\mathbf{R}_i$ [59]

$$w_i^{\mathrm{Hirshfeld}}(\mathbf{R}_i) = \frac{\rho_i^{\mathrm{atom}}(\mathbf{R}_i)}{\sum_{j=1}^{N} \rho_j^{\mathrm{atom}}(\mathbf{R}_i)} \ . \tag{4.6}$$

Since the density rearrangement in a H_2 (or equivalently D_2) molecule in the gas phase hardly affects the electron density at the nucleus, the superposition of electron densities of two non-interacting H (or equivalently D) atoms

$$\rho^{\mathrm{SCF}}(\mathbf{R}_i) \approx \rho_1^{\mathrm{H-atom}}(\mathbf{R}_i) + \rho_2^{\mathrm{H-atom}}(\mathbf{R}_i) \tag{4.7}$$

is a good approximation. Equation 4.6 then simplifies to

$$\rho_{\mathrm{emb},1(2)}^{\mathrm{AIM}} \approx \rho_{2(1)}^{\mathrm{H-atom}}(\mathbf{R}_{1(2)}) = \rho^{\mathrm{H-atom}}(d_{\mathrm{H-H}}). \tag{4.8}$$

Fig. 4.6 shows that this density is still quite seizable and the corresponding H-atom-in-jellium model with this background density results in a significant friction coefficient

4

$\eta^{\mathrm{H}}(\rho^{\mathrm{H-atom}}(d_{\mathrm{H-H}}))$. Transformation into the molecular coordinate system then yields approximately half of this value for $\eta_{dd}^{\mathrm{LDFA-AIM}}$ (twice for $\eta_{ZZ}^{\mathrm{LDFA-AIM}}$) in the gas phase as denoted by the reaction coordinate value -2 in Fig. 4.5B(C), respectively.

We emphasize that H_2 and D_2 are exceptional due to their short bond lengths. According to testing procedure explained in the previous paragraph, LDFA-AIM should still be applicable to other homo-nuclear diatomics.
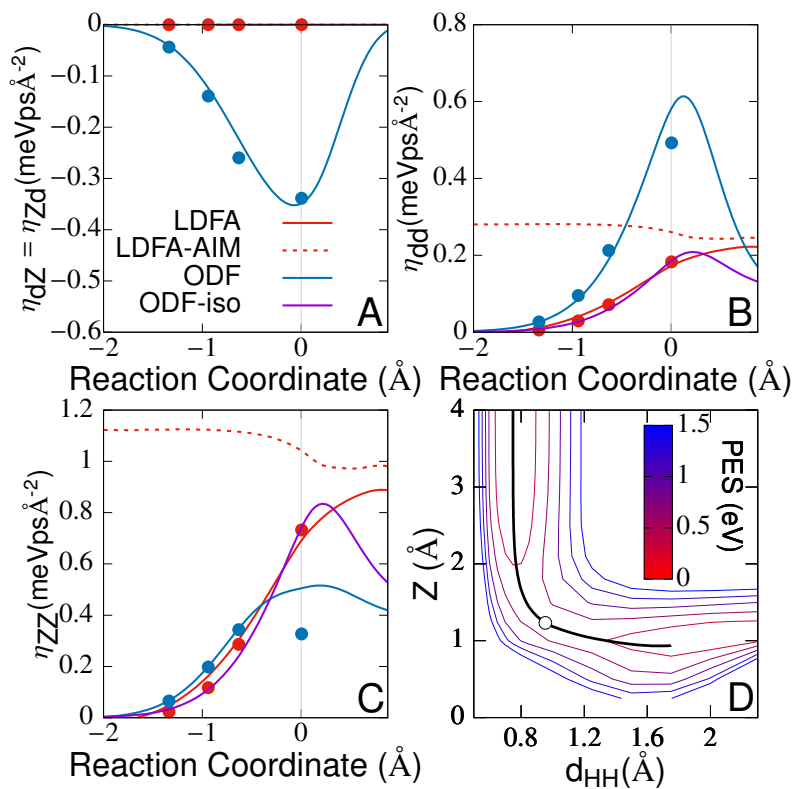
Figure 4.5: Same as Fig. 4.2, but additionally includes friction coefficients as resulting from the LDFA-AIM scheme [26] (dashed red line). Note that $\eta_{dZ}^{\mathrm{LDFA-AIM}} = 0$ since LDFA-AIM yields isotropic friction like LDFA relying on the independent atom approximation.[13]
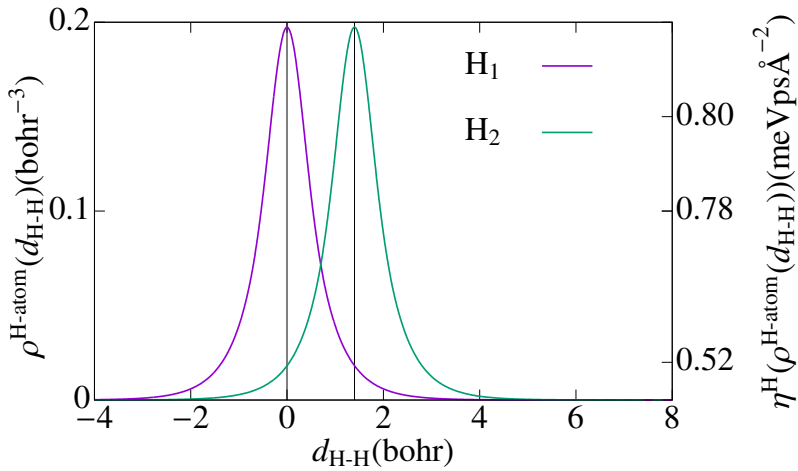
Figure 4.6: One-dimensional cut through electron densities of non-interacting hydrogen atoms ρ^{H-atom} located at the origin (purple curve) and at the experimental bond distance $d_{H-H} \approx 1.4$ bohr (green curve). ρ^{H-atom} has been obtained from a DFT calculation with the PW91 exchange correlation functional [53], i.e. using the same computational setup as the other DFT calculations in this chapter. The second y-axis shows the electronic friction coefficient $\eta^{H}(\rho^{H-atom}(d_{H-H}))$ as calculated based on the corresponding H-atom-in-jellium model for the background electron density $\rho^{H-atom}(d_{H-H})$.

4.B Continuous Representation of 6×6 Friction Tensors

4.B.1 Symmetry-Adapted Neural Network Representation

In principal, computationally efficient neural-network-based techniques as developed for potential energy surfaces in gas-surface dynamics can be adapted [57, 58, 60–62] – promising to accurately describe the 21 different elements of the symmetric 6×6 friction tensor as functions of the six molecular degrees of freedom, thus avoiding low-dimensional analytic forms [23, 44]. However, these 21 tensor elements are intertwined by symmetry of the static surface. This is not accounted for by the aforementioned techniques. To ensure that the friction tensor also represents the correct combination of translational and orientational symmetry and can account for molecular anisotropy, a molecular coordinate system is first introduced that denotes the center of mass positions (X, Y, Z), bond length d and spherical orientation (θ, ϕ), as depicted in Fig. 4.1A. For every molecular configuration a transformation $T(\theta, \phi)$ that transforms to the reference orientation $\theta_0 = \phi_0 = 90°$ is constructed, which characterizes the majority of dissociation paths with the lowest barriers [35]. The 6D electronic friction tensor is then defines as

$$\eta^{\mathrm{ODF}}(\mathbf{R}) \approx T(\theta, \phi) \, \tilde{\eta}^{\mathrm{ODF}}(X, Y, Z, d) \, T^{-1}(\theta, \phi) \tag{4.9}$$

because the 21 independent friction coefficients $\tilde{\eta}^{\mathrm{ODF}}_{i\alpha j\beta}(X, Y, Z, d)$ can now be fitted with 21 independent neural networks using the symmetry-adapted coordinates for fcc(111) surfaces as described by Meyer *et al.* [57, 58]. Sec. 4.B.2 provides a verification that $\tilde{\eta}^{\mathrm{ODF}}$ is rather independent of the choice of the reference orientation and the fitting accuracy of the neural network is discussed in Sec. 4.B.3.

4.B.2 Choice of Reference Angles ϕ_0 and θ_0

Fig. 4.7 shows the influence of the reference angle ϕ_0 and θ_0 as defined in the context of Eq. 4.9 on ODF coefficients obtained from DFT calculations. η_{dZ}, η_{dd} and η_{ZZ} do not depend significantly on the choice of ϕ_0, whereas θ_0 has a slightly bigger effect. However, since $\theta_0 = \phi_0 = 90°$ characterizes the majority of dissociation paths with
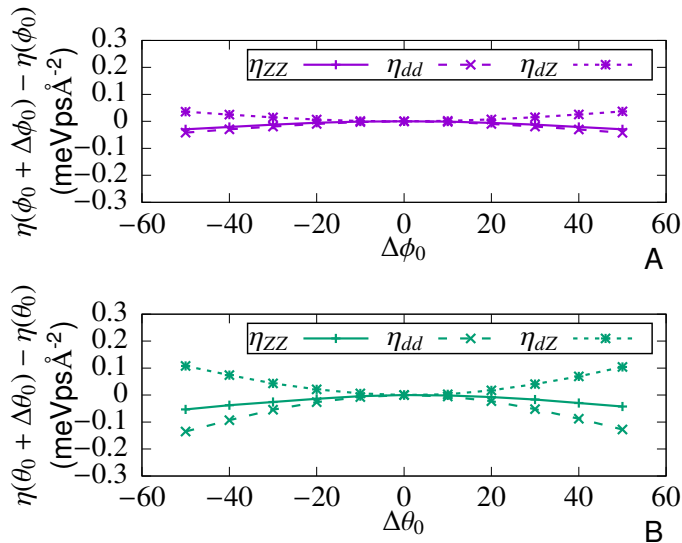
Figure 4.7: A (B) shows the influence of the reference angle ϕ_0 (θ_0) as defined in the context of Eq. 4.9 on ODF coefficients obtained from DFT calculations. The molecule is located at the transition state over the bridge site. Solid, long-dashed and short-dashed lines indicate η_{dZ}, η_{dd} and η_{ZZ}, respectively.

the lowest barriers [35] and due to the overall small effects of electronic friction on the dynamics, I am confident that these effects are not significant. Future work on other systems might require to explicitly include the angular orientation in the neural network fits.

4.B.3 Fitting Accuracy

This section details the fitting quality for the neural networks used to obtain continuous representations of the friction coefficients for the MDEF trajectory calculations. Since a very accurate such representation can be easily obtained for the local density friction approximation (LDFA) [39], only details for orbital-dependent friction (ODF) scheme are reported here.

Fig. 4.8 shows the root-mean-square errors (RMSEs) of the neural network (NN)
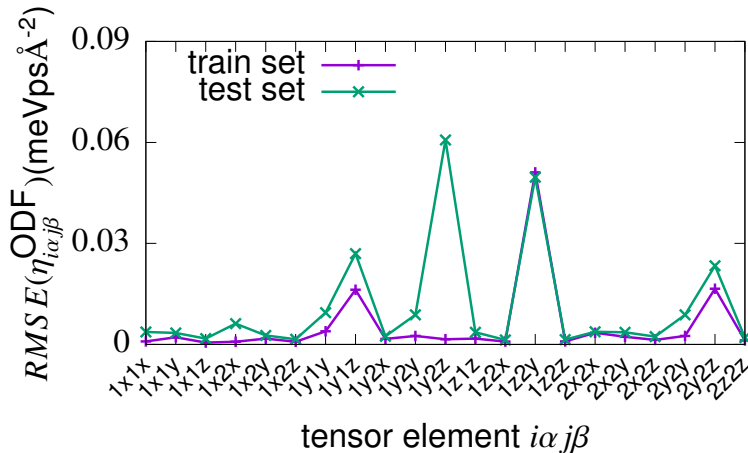
Figure 4.8: Root-mean-square errors (RMSEs) of the neural network fits for each of the 21 different elements $i\alpha j\beta$ of the symmetric 6×6 orbital-dependent friction (ODF) tensor $\eta_{i\alpha j\beta}^{\mathrm{ODF}}$. $i, j \in \{1, 2\}$ indicate the two hydrogen atoms and $\alpha, \beta \in \{x, y, z\}$ denote Cartesian coordinates.

fits for each of the 21 different elements of the symmetric 6×6 ODF tensor $\eta_{i\alpha j\beta}^{\mathrm{ODF}}$, where $i, j \in \{1, 2\}$ indicate the two hydrogen atoms and $\alpha, \beta \in \{x, y, z\}$ denote Cartesian coordinates. These fits are based on ≈ 30000 data points obtained from DFT calculations on the same 7 lateral sites that have been used to construct the SRP48-PES [34]. The training sets for the NN fits also contain some configurations of H_2 and D_2 at distances from the surfaces larger than 4 Å. At these distances, both the PW91-[35] and SRP48-PES[34] yield negligible molecule-surface interaction and hence, consistently, also the corresponding ODF coefficients are essentially zero. Since this "gas-phase region" is easily fitted by the NNs, those configurations are not included in the error analysis in order to avoid a bias of the RMSE.

The RMSEs are largest for the NN fits for the off-diagonal elements that describe the coupling between the z and y directions, both for the the same ($1y1z$, $2y2z$) and even more for different ($1y2z$, $1z2y$) hydrogen atoms. Using very similar convergence criteria in the DFT calculations for electron phonon matrix elements as well as for the Gaussian broadening of the δ-function for the sum over states, a very similar

convergence of the ODF coefficients of ± 10 % as reported by Maurer *et al.* in Refs [20, 27] is expected. This systematic error in the input data that forms the training and test sets for our NN fits is comparable to the aforementioned worst RMSEs, while the fits for all other 17 different tensor elements are up to an order of magnitude more accurate. Consequently, the fitting accuracy achieved here is considered more than sufficient for the present study.

A representative overview of the accuracy of the fits in this chapter is given in Fig. 4.9 by comparing their values for η_{dZ}, η_{dd} and η_{ZZ} along the minimum energy reaction path for dissociative chemisorption over the bridge site as obtained directly from our DFT calculations. These calculations were done separately on a dense grid of points along the reaction path and not included in the NN fits. For all of these three elements of the friction tensor, which are most important for the MDEF trajectory calculations presented, the agreement is excellent.

4
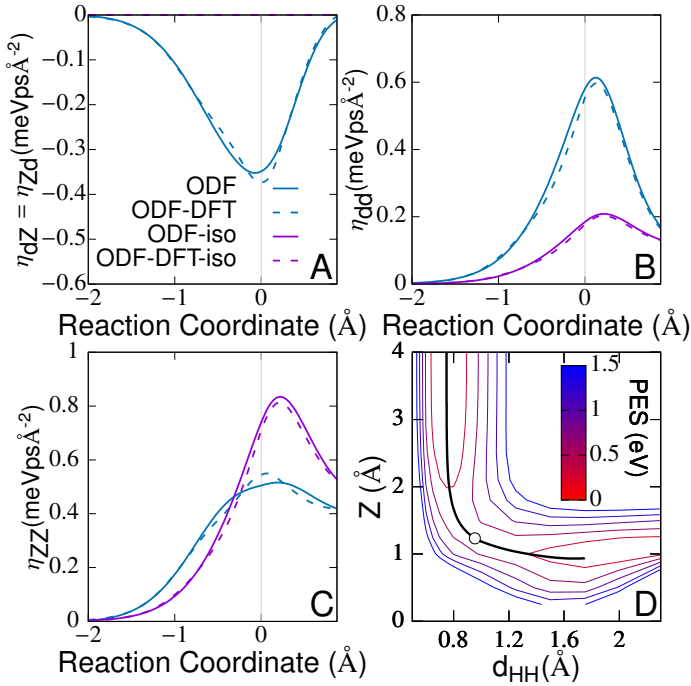
Figure 4.9: Similar to Fig. 4.2. A-C show η_{dZ}, η_{dd} and η_{ZZ} in the molecular coordinate system, respectively, along the minimum energy reaction path for dissociative chemisorption over the bridge site as depicted in D together with the corresponding two-dimensional PES cut. See Fig. 4.1 for the coordinate system. Blue (purple) show tensor elements for the ODF (ODF-iso) scheme. Dashed lines are for values obtained directly from our DFT calculations on a dense grid of points along the reaction path and not included in the NN fits. Solid lines are from the NN fits evaluated on the same grid.

4.C Errors Due to Statistical Sampling

In this section the errors of the quantities shown in Fig. 4.4 are discussed. These errors arise from the statistical sampling of the initial conditions (angular orientation of the molecule, lateral impact site, bond distance and corresponding velocity according to the classical equivalent of the vibrational state) with a finite number of molecular dynamics trajectories N [30, 35].

4.C.1 Inelastic Scattering Probabilities $P_{\text{transition}}$

The standard error of the state-to-state-specific inelastic scattering probabilities $P_{\text{transition}}$ shown in Figures 4 C and D are given by

$$\sigma^{\text{SE}}_{P_{\text{transition}}}(N) = \sqrt{\frac{P_{\text{transition}}\left(1 - P_{\text{transition}}\right)}{N}}. \tag{4.10}$$

Since $\sigma^{\text{SE}}_{P_{\text{transition}}}(N) \leq \frac{0.5}{\sqrt{N}}$, the errors of $P_{\text{transition}}$ due to statistical sampling are completely negligible on the scale of the plots for the large amount of trajectories simulated here ($N = 50000$). Consequently, no error bars have been included. The same argument holds for the dissociative sticking probabilities S_0 shown in Fig. 4.2 as well.

4.C.2 Average Translational Energy Gain $\langle \Delta E_{\text{trans}} \rangle$

Concerning the average translational energy gain $\langle \Delta E_{\text{trans}} \rangle$ for vibrationally inelastic scattering from vibrational state $\nu = 2, J = 1(2)$ to $\nu = 1, J = 1(2)$ for H_2 (D_2) presented in Figures 4 A and B, the standard deviation

$$\sigma_{\langle \Delta E_{\text{trans}} \rangle} = \sqrt{\frac{1}{N_{\text{scatt}}} \sum_{i}^{N_{\text{scatt}}} \left(\Delta E^i_{\text{trans}} - \langle \Delta E_{\text{trans}} \rangle\right)^2} \quad . \tag{4.11}$$

is calculated first. $\Delta E^i_{\text{trans}}$ is the change in translational energy corresponding to scattered trajectory i. N_{scatt} denotes the amount of scattered trajectories that undergo the specific aforementioned transition, i.e.

$$N_{\text{scatt}} = P_{\text{transition}} \cdot N \quad . \tag{4.12}$$

For the results in this chapter the standard deviation is considered to be an estimator for the error of a single trajectory i, indicating the spread of $\Delta E_{\text{trans}}^i$ around the average $\langle \Delta E_{\text{trans}} \rangle$. Then, according to the "law of large numbers", the standard error

$$\sigma_{\langle \Delta E_{\text{trans}} \rangle}^{\text{SE}} \;=\; \frac{\sigma_{\langle \Delta E_{\text{trans}} \rangle}}{\sqrt{N_{\text{scatt}}}} \;=\; \frac{1}{N_{\text{scatt}}} \sqrt{\sum_{i}^{N_{\text{scatt}}} \left(\Delta E_{\text{trans}}^i - \langle \Delta E_{\text{trans}} \rangle \right)^2} \tag{4.13}$$

is an estimator for the error of $\langle \Delta E_{\text{trans}} \rangle$ with respect to the statistical sampling. Assuming a 95% confidence interval for a normal distribution, the error bars in Figures 4 A and B are obtained from $1.96 \cdot \sigma_{\langle \Delta E_{\text{trans}} \rangle}^{\text{SE}}$. Since the corresponding scattering probabilities $P_{\text{transition}}$ can be less than 1 % (see Figures 4 C and D), at least 10^4 trajectories are required for those errors to become sufficiently small so that the predictions of the different electronic friction models are clearly distinguishable.

4.D Vibrational De-Excitation for PW91-PES
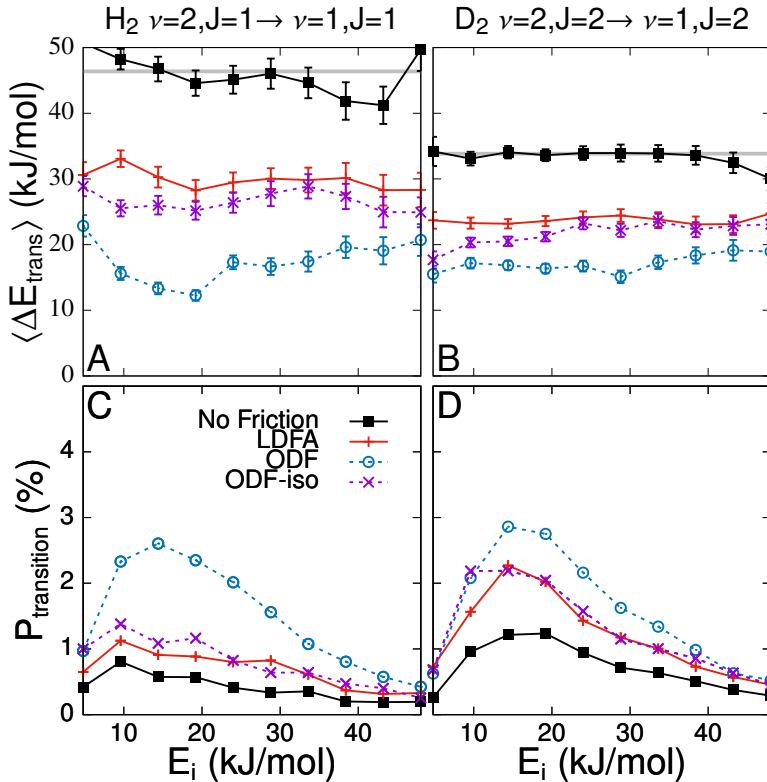
Figure 4.10: Same as Fig. 4.4, but trajectories calculated using a PW91 [35] instead of a SRP48 PES [34]. Vibrational de-excitation probabilities $P_{\text{transition}}$ (lower row) and concomitant average gain in translational energy $\langle \Delta E_{\text{trans}} \rangle$ (upper row) as a function of normal incidence energy E_i for state-to-state scattering. Panels A,C (B,D) are for the transition from the rovibrational state $\nu = 2, J = 1(2)$ to $\nu = 1, J = 1(2)$ for H_2 (D_2). Shown are results from adiabatic calculations (filled black squares), as well as those including electronic friction according to the LDFA (red plusses), ODF (blue circles) or ODF-iso (purple crosses) models. The error bars indicate the error due to statistical sampling as described in Section 4.C.

References

[1] P. Spiering and J. Meyer. "Testing Electronic Friction Models: Vibrational De-Excitation in Scattering of H_2 and D_2 from Cu(111)". In: *J. Phys. Chem. Lett.* 9 (2018), pp. 1803–1808. DOI: `10.1021/acs.jpclett.7b03182`.

[2] A. M. Wodtke, J. C. Tully, and D. J. Auerbach. "Electronically Non-Adiabatic Interactions of Molecules at Metal Surfaces: Can We Trust the Born-Oppenheimer Approximation for Surface Chemistry?" In: *Int. Rev. Phys. Chem.* 23.4 (2004), pp. 513–539.

[3] G.-J. Kroes. "Frontiers in Surface Scattering Simulations". In: *Science* 321 (2008), pp. 794–797. DOI: `10.1126/science.1157717`.

[4] K. Golibrzuch, N. Bartels, D. J. Auerbach, and A. M. Wodtke. "The Dynamics of Molecular Interactions and Chemical Reactions at Metal Surfaces: Testing the Foundations of Theory". In: *Annu. Rev. Phys. Chem.* 66 (2015), pp. 399–425. DOI: `10.1146/annurev-physchem-040214-121958`.

[5] A. M. Wodtke. "Electronically Non-Adiabatic Influences in Surface Chemistry and Dynamics". In: *Chem. Soc. Rev.* 45 (2016), pp. 3641–3657. DOI: `10.1039/C6CS00078A`.

[6] N. Shenvi, S. Roy, and J. C. Tully. "Nonadiabatic Dynamics at Metal Surfaces: Independent-Electron Surface Hopping". In: *J. Chem. Phys.* 130 (2009), p. 174107. DOI: `10.1063/1.3125436`.

[7] J. Meyer and K. Reuter. "Electron–Hole Pairs during the Adsorption Dynamics of O_2 on Pd(100): Exciting or Not?" In: *New J. Phys.* 13 (2011), p. 085010. DOI: `10.1088/1367-2630/13/8/085010`.

[8] I. G. Ryabinkin and A. F. Izmaylov. "Mixed Quantum-Classical Dynamics Using Collective Electronic Variables: A Better Alternative to Electronic Friction Theories". In: *J. Phys. Chem. Lett.* 8 (2017), pp. 440–444. DOI: `10.1021/acs.jpclett.6b02712`.

[9] W. Dou, G. Miao, and J. E. Subotnik. "Born-Oppenheimer Dynamics, Electronic Friction, and the Inclusion of Electron-Electron Interactions". In: *Phys. Rev. Lett.* 119 (2017), p. 046001. DOI: `10.1103/PhysRevLett.119.046001`.

[10] S. P. Rittmeyer, J. Meyer, and K. Reuter. "Nonadiabatic Vibrational Damping of Molecular Adsorbates: Insights into Electronic Friction and the Role of Electronic Coherence". In: *Phys. Rev. Lett.* 119 (2017), p. 176808. DOI: `10.1103/PhysRevLett.119.176808`.

[11] M. Head-Gordon and J. C. Tully. "Molecular Dynamics with Electronic Frictions". In: *J Chem Phys* 103 (1995), pp. 10137–10145. DOI: `10.1063/1.469915`.

4

[12] M. Alducin, R. Díez Muiño, and J. I. Juaristi. "Non-Adiabatic Effects in Elementary Reaction Processes at Metal Surfaces". In: *Prog. Surf. Sci.* 92 (2017), pp. 317–340. DOI: 10.1016/j.progsurf.2017.09.002.

[13] J. I. Juaristi, M. Alducin, R. D. Muiño, H. F. Busnengo, and A. Salin. "Role of Electron-Hole Pair Excitations in the Dissociative Adsorption of Diatomic Molecules on Metal Surfaces". In: *Phys. Rev. Lett.* 100 (2008), p. 116102. DOI: 10.1103/PhysRevLett.100.116102.

[14] D. Novko, M. Blanco-Rey, M. Alducin, and J. I. Juaristi. "Surface Electron Density Models for Accurate *Ab Initio* Molecular Dynamics with Electronic Friction". In: *Phys. Rev. B* 93 (2016), p. 245435. DOI: 10.1103/PhysRevB.93.245435.

[15] B. Hellsing and M. Persson. "Electronic Damping of Atomic and Molecular Vibrations at Metal Surfaces". In: *Phys Scr* 29 (1984), p. 360. DOI: 10.1088/0031-8949/29/4/014.

[16] S. M. Janke, D. J. Auerbach, A. M. Wodtke, and A. Kandratsenka. "An Accurate Full-Dimensional Potential Energy Surface for h(111): Importance of Nonadiabatic Electronic Excitation in Energy tTansfer and Adsorption". In: *J. Chem. Phys.* 143 (2015), p. 124708. DOI: 10.1063/1.4931669.

[17] O. Bünermann, H. Jiang, Y. Dorenkamp, A. Kandratsenka, S. M. Janke, et al. "Electron-Hole Pair Excitation Determines the Mechanism of Hydrogen Atom Adsorption". In: *Science* 350 (2015), pp. 1346–1349. DOI: 10.1126/science.aad4972.

[18] M. Askerka, R. J. Maurer, V. S. Batista, and J. C. Tully. "Role of Tensorial Electronic Friction in Energy Transfer at Metal Surfaces". In: *Phys. Rev. Lett.* 116 (2016), p. 217601. DOI: 10.1103/PhysRevLett.116.217601.

[19] K.-i. Inoue, K. Watanabe, T. Sugimoto, Y. Matsumoto, and T. Yasuike. "Disentangling Multidimensional Nonequilibrium Dynamics of Adsorbates: CO Desorption from Cu(100)". In: *Phys. Rev. Lett.* 117 (2016), p. 186101. DOI: 10.1103/PhysRevLett.117.186101.

[20] R. J. Maurer, B. Jiang, H. Guo, and J. C. Tully. "Mode Specific Electronic Friction in Dissociative Chemisorption on Metal Surfaces: H_2 on Ag(111)". In: *Phys. Rev. Lett.* 118 (2017), p. 256001. DOI: 10.1103/PhysRevLett.118.256001. arXiv: 1705.09753 [cond-mat.mtrl-sci].

[21] A. C. Luntz, I. Makkonen, M. Persson, S. Holloway, D. M. Bird, et al. "Comment on "Role of Electron-Hole Pair Excitations in the Dissociative Adsorption of Diatomic Molecules on Metal Surfaces"". In: *Phys. Rev. Lett.* 102 (2009), p. 109601. DOI: 10.1103/PhysRevLett.102.109601.

4

[22] J. I. Juaristi, M. Alducin, R. D. Muiño, H. F. Busnengo, and A. Salin. "Juaristi et al. Reply:" in: *Phys. Rev. Lett.* 102 (2009), p. 109602. DOI: 10.1103/PhysRevLett.102.109602.

[23] A. C. Luntz and M. Persson. "How Adiabatic Is Activated Adsorption/Associative Desorption?" In: *J. Chem. Phys.* 123 (2005), p. 074704. DOI: 10.1063/1.2000249.

[24] V. Krishna and J. C. Tully. "Vibrational Lifetimes of Molecular Adsorbates on Metal Surfaces". In: *J. Chem. Phys.* 125 (2006), p. 054706. DOI: 10.1063/1.2227383.

[25] M. Forsblom and M. Persson. "Vibrational Lifetimes of Cyanide and Carbon Monoxide on Noble and Transition Metal Surfaces". In: *J. Chem. Phys.* 127 (2007), p. 154303. DOI: 10.1063/1.2794744.

[26] S. P. Rittmeyer, J. Meyer, J. I. Juaristi, and K. Reuter. "Electronic Friction-Based Vibrational Lifetimes of Molecular Adsorbates: Beyond the Independent-Atom Approximation". In: *Phys. Rev. Lett.* 115 (2015), p. 046102. DOI: 10.1103/PhysRevLett.115.046102.

[27] R. J. Maurer, M. Askerka, V. S. Batista, and J. C. Tully. "Ab Initio Tensorial Electronic Friction for Molecules on Metal Surfaces: Nonadiabatic Vibrational Relaxation". In: *Phys. Rev. B* 94 (2016), p. 115432. DOI: 10.1103/PhysRevB.94.115432.

[28] D. Novko, M. Alducin, M. Blanco-Rey, and J. I. Juaristi. "Effects of Electronic Relaxation Processes on Vibrational Linewidths of Adsorbates on Surfaces: The Case of CO/Cu(100)". In: *Phys. Rev. B* 94 (2016). DOI: 10.1103/PhysRevB.94.224306.

[29] G.-J. Kroes, J. I. Juaristi, and M. Alducin. "Vibrational Excitation of H2 Scattering from Cu(111): Effects of Surface Temperature and of Allowing Energy Exchange with the Surface". In: *J. Phys. Chem. C* 121 (2017), pp. 13617–13633. DOI: 10.1021/acs.jpcc.7b01096.

[30] C. Díaz, E. Pijper, R. A. Olsen, H. F. Busnengo, D. J. Auerbach, et al. "Chemically Accurate Simulation of a Prototypical Surface Reaction: H2 Dissociation on Cu(111)". In: *Science* 326 (2009), pp. 832–834. DOI: 10.1126/science.1178722.

[31] F. Nattino, A. Genova, M. Guijt, A. S. Muzas, C. Díaz, et al. "Dissociation and Recombination of D_2 on Cu(111): Ab Initio Molecular Dynamics Calculations and Improved Analysis of Desorption Experiments". In: *J. Chem. Phys.* 141 (2014), p. 124705. DOI: 10.1063/1.4896058.

[32] G.-J. Kroes and C. Díaz. "Quantum and Classical Dynamics of Reactive Scattering of H2 from Metal Surfaces". In: *Chem. Soc. Rev.* 45 (2016), pp. 3658–3700. DOI: 10.1039/C5CS00336A.

4

[33] C. Díaz, R. A. Olsen, D. J. Auerbach, and G.-J. Kroes. "Six-Dimensional Dynamics Study of Reactive and Non Reactive Scattering of H2 from Cu(111) Using a Chemically Accurate Potential Energy Surface". In: *Phys. Chem. Chem. Phys.* 12 (2010), pp. 6499–6519. DOI: 10.1039/C001956A.

[34] A. Mondal, M. Wijzenbroek, M. Bonfanti, C. Díaz, and G.-J. Kroes. "Thermal Lattice Expansion Effect on Reactive Scattering of H2 from Cu(111) at Ts = 925 K". In: *J. Phys. Chem. A* 117 (2013), pp. 8770–8781. DOI: 10.1021/jp4042183.

[35] C. Diaz, R. A. Olsen, H. F. Busnengo, and G.-J. Kroes. "Dynamics on Six-Dimensional Potential Energy Surfaces for H2/Cu(111): Corrugation Reducing Procedure versus Modified Shepard Interpolation Method and PW91 versus RPBE". In: *J. Phys. Chem. C* 114 (2010), pp. 11192–11201. DOI: 10.1021/jp1027096.

[36] W. H. Butler, F. J. Pinski, and P. B. Allen. "Phonon Linewidths and Electron-Phonon Interaction in Nb". In: *Phys. Rev. B* 19.7 (1979), pp. 3708–3721.

[37] M. J. Puska and R. M. Nieminen. "Atoms Embedded in an Electron Gas: Phase Shifts and Cross Sections". In: *Phys. Rev. B* 27 (1983), p. 6121. DOI: 10.1103/PhysRevB.27.6121.

[38] N. Gerrits, J. I. Juaristi, and J. Meyer. "Atoms in Jellium Revisited - Implications for the Local Density Friction Approximation?" In: *Prep.* (2017).

[39] P. Saalfrank, J. I. Juaristi, M. Alducin, M. Blanco-Rey, and R. D. Muiño. "Vibrational Lifetimes of Hydrogen on Lead Films: An Ab Initio Molecular Dynamics with Electronic Friction (AIMDEF) Study". In: *J. Chem. Phys.* 141 (2014), p. 234702. DOI: 10.1063/1.4903309.

[40] M. Askerka, R. J. Maurer, V. S. Batista, and J. C. Tully. "Erratum: Role of Tensorial Electronic Friction in Energy Transfer at Metal Surfaces [Phys. Rev. Lett. 116, 217601 (2016)]". In: *Phys. Rev. Lett.* 119 (2017), p. 069901. DOI: 10.1103/PhysRevLett.119.069901.

[41] C. T. Rettner, H. A. Michelsen, and D. J. Auerbach. "Quantum-State-Specific Dynamics of the Dissociative Adsorption and Associative Desorption of H_2 at a Cu(111) Surface". In: *J. Chem. Phys.* 102 (1995), pp. 4625–4641. DOI: 10.1063/1.469511.

[42] H. A. Michelsen, C. T. Rettner, D. J. Auerbach, and R. N. Zare. "Effect of Rotation on the Translational and Vibrational Energy Dependence of the Dissociative Adsorption of D_2 on Cu(111)". In: *J. Chem. Phys.* 98 (1993), pp. 8294–8307. DOI: 10.1063/1.464535.

[43] A. S. Muzas, J. I. Juaristi, M. Alducin, R. D. Muiño, G. J. Kroes, et al. "Vibrational Deexcitation and Rotational Excitation of H2 and D2 Scattered from Cu(111): Adiabatic versus Non-Adiabatic Dynamics". In: *J. Chem. Phys.* 137 (2012), p. 064707. DOI: 10.1063/1.4742907.

[44] A. C. Luntz, M. Persson, and G. O. Sitz. "Theoretical Evidence for Nonadiabatic Vibrational Deexcitation in H2(D2) State-to-State Scattering from Cu(100)". In: *J. Chem. Phys.* 124 (2006), p. 091101. DOI: 10.1063/1.2177664.

[45] K. Golibrzuch, P. R. Shirhatti, I. Rahinov, A. Kandratsenka, D. J. Auerbach, et al. "The Importance of Accurate Adiabatic Interaction Potentials for the Correct Description of Electronically Nonadiabatic Vibrational Energy Transfer: A Combined Experimental and Theoretical Study of NO($v = 3$) Collisions with a Au(111) Surface". In: *J. Chem. Phys.* 140 (2014), p. 044701. DOI: 10.1063/1.4861660.

[46] B. C. Krüger, N. Bartels, C. Bartels, A. Kandratsenka, J. C. Tully, et al. "NO Vibrational Energy Transfer on a Metal Surface: Still a Challenge to First-Principles Theory". In: *J. Phys. Chem. C* 119 (2015), pp. 3268–3272. DOI: 10.1021/acs.jpcc.5b00388.

[47] A. Hodgson, J. Moryl, P. Traversaro, and H. Zhao. "Energy Transfer and Vibrational Effects in the Dissociation and Scattering of D2 from Cu (111)". In: *Nature* 356 (1992), p. 501. DOI: 10.1038/356501a0.

[48] C. T. Rettner, D. J. Auerbach, and H. A. Michelsen. "Observation of Direct Vibrational Excitation in Collisions of H_2 and D_2 with a Cu(111) Surface". In: *Phys. Rev. Lett.* 68 (1992), pp. 2547–2550. DOI: 10.1103/PhysRevLett.68.2547.

[49] A. Hodgson, P. Samson, A. Wight, and C. Cottrell. "Rotational Excitation and Vibrational Relaxation of H 2 (Υ= 1, J= 0) Scattered from Cu (111)". In: *Phys. Rev. Lett.* 78.5 (1997), p. 963.

[50] For lower incidence energies, scattering over the top site has been found to dominate vibrational de-excitation from $\nu = 1$ in adiabatic calculations [43]. Indeed, for top sites, $\eta_{dd}^{\mathrm{ODF-iso}}$ is rather different from $\eta_{dd}^{\mathrm{LDFA}}$ so that the difference in electronic structure inherent to LDFA and ODF also becomes visible in the dynamics in this case.

[51] W. E. Perreault, N. Mukherjee, and R. N. Zare. "Preparation of a Selected High Vibrational Energy Level of Isolated Molecules". In: *J. Chem. Phys.* 145 (2016), p. 154203. DOI: 10.1063/1.4964938.

[52] S. Baroni, S. de Gironcoli, A. Dal Corso, and P. Giannozzi. "Phonons and Related Crystal Properties from Density-Functional Perturbation Theory". In: *Rev. Mod. Phys.* 73 (2001), pp. 515–562. DOI: 10.1103/RevModPhys.73.515.

4

[53] J. P. Perdew, J. A. Chevary, S. H. Vosko, K. A. Jackson, M. R. Pederson, et al. "Atoms, Molecules, Solids, and Surfaces: Applications of the Generalized Gradient Approximation for Exchange and Correlation". In: *Phys. Rev. B* 46 (1992), pp. 6671–6687. DOI: 10.1103/PhysRevB.46.6671.

[54] P. Giannozzi, S. Baroni, N. Bonini, M. Calandra, R. Car, et al. "QUANTUM ESPRESSO: A Modular and Open-Source Software Project for Quantum Simulations of Materials". In: *J Phys Condens Matter* 21 (2009), p. 395502. DOI: 10.1088/0953-8984/21/39/395502.

[55] D. R. Hamann. "Optimized Norm-Conserving Vanderbilt Pseudopotentials". In: *Phys. Rev. B* 88 (2013), p. 085117. DOI: 10.1103/PhysRevB.88.085117.

[56] M. Schlipf and F. Gygi. "Optimization Algorithm for the Generation of ONCV Pseudopotentials". In: *Comput. Phys. Commun.* 196 (2015), pp. 36–44. DOI: 10.1016/j.cpc.2015.05.011.

[57] J. Meyer. "Ab Initio Modeling of Energy Dissipation during Chemical Reactions at Transition Metal Surfaces". PhD thesis. Freie Universität Berlin, Freie Universität Berlin, Germany, 2012.

[58] I. Goikoetxea, J. Beltrán, J. Meyer, J. I. Juaristi, M. Alducin, et al. "Non-Adiabatic Effects during the Dissociative Adsorption of O_2 at Ag(111)? A First-Principles Divide and Conquer Study". In: *New J. Phys.* 14 (2012), p. 013050. DOI: 10.1088/1367-2630/14/1/013050.

[59] F. L. Hirshfeld. "Bonded-Atom Fragments for Describing Molecular Charge Densities". In: *Theoret. Chem. Acta* 44 (1977), pp. 129–138. DOI: 10.1007/BF00549096.

[60] J. Behler, S. Lorenz, and K. Reuter. "Representing Molecule-Surface Interactions with Symmetry-Adapted Neural Networks". In: *J. Chem. Phys.* 127 (2007), p. 014705. DOI: 10.1063/1.2746232.

[61] B. Jiang and H. Guo. "Permutation Invariant Polynomial Neural Network Approach to Fitting Potential Energy Surfaces. III. Molecule-Surface Interactions". In: *J. Chem. Phys.* 141 (2014), p. 034109. DOI: 10.1063/1.4887363.

[62] K. Shakouri, J. Behler, J. Meyer, and G.-J. Kroes. "Accurate Neural Network Description of Surface Phonons in Reactive Gas–Surface Dynamics: N_2 + Ru(0001)". In: *J. Phys. Chem. Lett.* 8 (2017), pp. 2131–2136. DOI: 10.1021/acs.jpclett.7b00784.

4

Chapter 5

Orbital-Dependent Electronic Friction Significantly Affects the Description of Reactive Scattering of N$_2$ from Ru(0001)

5

Abstract

Electron-hole pair (ehp) excitation is thought to substantially affect the dynamics of molecules on metal surfaces, but it is not clear whether this can be better addressed by orbital dependent friction (ODF) or the local density friction approximation (LDFA). This chapter discusses the effect of ehp excitation on the dissociative chemisorption of N_2 on and its inelastic scattering from Ru(0001), which is the benchmark system of highly activated dissociation, with these two rivaling models. ODF yields results for sticking, energy transfer to the surface and vibrational excitation of N_2 that are in significantly better agreement with existing experimental data than the LDFA results. N_2 on Ru(0001) is thus the first system for which the ODF and LDFA approaches are shown to yield substantially different results for easily accessible experimental observables including reaction probabilities, making it a good test system for modeling ehp excitation for reactive scattering.

5.1   Introduction

In the dawning age of sustainability, chemical reactions on metal surfaces play a crucial role in heterogeneously catalysed processes that feed and fuel our modern societies. The corresponding reaction rates are usually obtained based on the Born-Oppenheimer (BO) approximation and concomitant (adiabatic) potential energy surfaces (PESs) [2, 3]. It has been suggested that non-adiabatic effects in the form of ehp excitations, which are not captured within the BO approximation, may significantly affect the underlying dynamics of molecules on metal surfaces [4–10]. However, non-adiabatic effects cannot be quantified by experimental data alone. Instead, state-of-the-art first-principles based computer simulations are mandatory, in combination with measurements from well-defined molecular beam experiments under clean ultra-high vacuum conditions.

The current workhorse model for including non-adiabatic effects in simulations of molecular beam experiments is molecular dynamics with electronic friction (MDEF) [11, 12], with two rivaling theoretical approaches for obtaining the electronic friction coefficients: The local density friction approximation (LDFA) determines the latter

based on the surface electron density [13] according to the computationally inexpensive atoms-in-jellium model [14].

The LDFA enables the inclusion of all degrees of freedom of a molecule in dynamical simulations[13, 15], but at the same time implies the independent atom approximation (IAA) in most practical applications, thus neglecting any potential molecular effects [16, 17]. This is no problem for atomic projectiles, and the LDFA yields accurate results for atoms scattering from metal surfaces [18]. Orbital-dependent friction (ODF) invokes first order time-dependent perturbation theory for the Kohn-Sham orbitals resulting from density functional theory calculations of an atom or molecule interacting with the surface [11, 12, 19], so that the effects of molecular electronic structure are taken into account (no IAA). ODF is thus expected to be important for reactive scattering of molecules from metal surfaces [16, 20–22]. However, recently, the pragmatic use of broadening techniques for the calculation of ODF coefficients, which is currently without any alternative [19, 20, 22–24], has been criticized to affect the values obtained for these coefficients in an undefined fashion [25]. In summary, the LDFA and ODF as now implemented both have advantages and disadvantages, and a clear verification is still pending for which of the two methods best describes dissociative chemisorption. Due to the very high computational cost of ODF it has only recently been used for the simulation of reactive scattering in two systems, i.e., H_2 and D_2 from Ag(111) [22, 24] and Cu(111) [23], including all six molecular degrees of freedom. For these two system no significant differences were found between reaction probabilities computed with ODF and the LDFA.

Given this situation, other systems are required that offer the possibility to distinguish LDFA and ODF, ideally by benchmarking against data from molecular beam experiments. Luntz and coworkers have suggested that N_2 on Ru(0001) could be such a system after extensive experimental and pioneering low-dimensional computational studies [26–28]. This prototypical case of highly activated diatomic molecule dissociation has received much attention due to the relevance of N_2 dissociation as rate-limiting step for ammonia production via the Haber-Bosch process[29]. Recent results from LDFA calculations indicate that electronic friction is not important for the dissocia-

tive chemisorption probability [30], whereas experiments have demonstrated that N_2 molecules associatively desorbing from Ru(0001) experience a large amount of vibrational quenching[31, 32] that cannot be explained using BO-based theory[26, 33].

This chapter shows that the high-dimensional ODF model [23] already presented in Chap. 4 but now applied to N_2 on Ru(0001), which includes frictional couplings and the motion in all six molecular degrees of freedom, reduces the dissociative chemisorption probability by about 50% compared to both adiabatic calculations and the LDFA. Furthermore, the results in this chapter demonstrate that ODF improves the description of energy transfer during scattering and provides the best agreement with the corresponding experimental data. N_2 on Ru(0001) is thus the first system for which the ODF and LDFA approaches are shown to yield substantially different results for easily accessible experimental observables including reaction probabilities. The error bars of the experimental data still prevent an unequivocal verification of the quantitative performance of ODF. Nevertheless, our results pave the way for subsequent improved experimental and theoretical studies which will clearly show whether ODF indeed better describes the non-adiabatic reaction in this benchmark system, as our present calculations suggest.

5.2 Methods

MDEF [11, 12] calculations are performed according to the generalized Langevin equation (GLE)

$$m_i \frac{d^2 \mathbf{r}}{dt} = -\nabla V \left(\mathbf{r}^{N_2}, \mathbf{r}^{Ru} \right) \ - \ \sum \boldsymbol{\eta}^{N_2} \left(\mathbf{r}^{N_2} \right) \frac{d\mathbf{r}^{N_2}}{dt} \ + \ \mathcal{F}^{N_2} \left(\boldsymbol{\eta}, T_s \right) \quad , \qquad (5.1)$$

where $V \left(\mathbf{r}^{N_2}, \mathbf{r}^{Ru} \right)$ is the potential energy surface that describes the (electronically adiabatic) interaction between a N_2 molecule and the Ru(0001) surface consisting of mobile surface atoms described by coordinates $\mathbf{r}^{N_2}$ and $\mathbf{r}^{Ru}$, respectively. The high-dimensional neural network (HD-NNP) PES from Shakouri et al. [34], which has been fitted to a DFT reference dataset based on the RPBE functional [35] using the Behler-Parinello method [36], is used for the potential energy surface and concomitant forces.
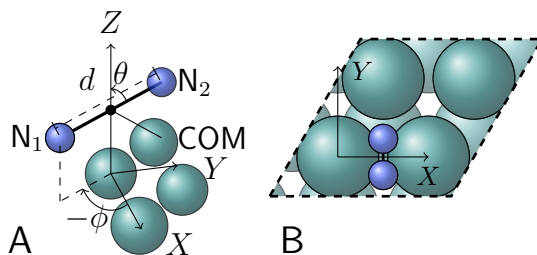
Figure 5.1: (A) Six-dimensional coordinate system for the description of N_2 molecules on Ru(0001), consisting of the center of mass (COM) coordinates (X,Y,Z) and the N_2 bond distance d as well as the polar angle θ and azimuthal angle ϕ. X,Y,Z = 0 corresponds to the position of a Ru atom in the surface plane (top site). (B) Top view of a N_2 molecule with its molecular axis parallel to the surface over a bridge site in a bridge-to-hollow orientation $(X = \frac{1}{2}a, Y = 0, \theta = 90°, \phi = 90°)$. a denotes the surface lattice constant. First (second) layer Ru atoms are shown in (transparent) green. Dashed black lines show the periodic boundary conditions of a 2x2 super cell.

The friction tensor $\boldsymbol{\eta}^{N_2}$ and the random forces $\mathcal{F}^{N_2}(\boldsymbol{\eta}, T_s)$ describe the non-adiabatic coupling of the N_2 molecules with electron-hole pair excitations in the surface at the surface temperature T_s. The ODF tensor [23] is calculated in the same way as in Chap. 4 from Density Functional Perturbation Theory. This 6×6 tensor depends on the six coordinates of the two nitrogen atoms, which are most conveniently described in the coordinate system shown in Figure 5.1. Subsequently, we have constructed an accurate continuous representation using a neural network approach as detailed in the supporting information, which – together with the HD-NNP PES – allows calculating a large enough number of trajectories to obtain sticking probabilities that can be compared to experimental data [34, 37]. Previous work has shown that surface atom displacements hardly affect the results of ab initio MDEF calculations based on the LDFA for N_2 on Fe(110) [38]. Therefore, the influence of surface atom displacements on the friction tensor is neglected for the results in this chapter.

In order to numerically integrate equation 5.1, I have adapted a recently suggested Liouville operator technique, denoted by OVRVO in ref [39], which simplifies to the

conventional velocity-Verlet algorithm[40] in the absence of friction. This technique allows defining a conserved total energy [41], which has enabled us to monitor and thus ensure the accuracy of the numerical integration of the trajectories. It has also greatly simplified the analysis of the energy exchange with the surface – in particular for the non-adiabatic energy which is dissipated into the electron-hole pair excitations in the surface.

First a comparison is made between the results obtained with the new ODF model and previous results using LDFA and adiabatic simulations for a mobile surface (BOMS) without electronic friction (i.e. without the last two terms in Eq. 5.1), focusing on a surface temperature $T_s = 575$ K, which is comparable to the experimental conditions for which data has been obtained [26, 27, 42] and relevant for catalytic conditions of the Haber-Bosch cycle. In more approximate calculations all the Ruthenium atoms are frozen at their equilibrium positions, resulting in the so-called Born-Oppenheimer static surface (BOSS) model, which does not allow for any energy exchange with the surface [37, 43].

5.3 Results

Figure 5.2 shows the initial sticking probabilities for the dissociative chemisorption of N_2 on Ru(0001). Except for the lowest incidence energy (1.50 eV) the BOSS model does not reproduce the experimental results [42]. Including surface motion (BOMS) reproduces the experiment within error bars as has already previously been shown [30, 34]. The LDFA does not yield any significant changes compared to the BOMS model. The closest agreement is found with experimental data when the ODF model is used to describe the electronic friction. The effect of the ODF is quantified on a linear scale in the inset of Figure 5.2, which shows the decrease of the reaction probability of both electronic friction models relative to the BOMS results. Also on this scale, the results from the LDFA and BOMS model are hardly distinguishable. ODF on the other hand decreases the sticking probability, relative to BOMS, from lower to higher incidence energies by 61% to 41%.
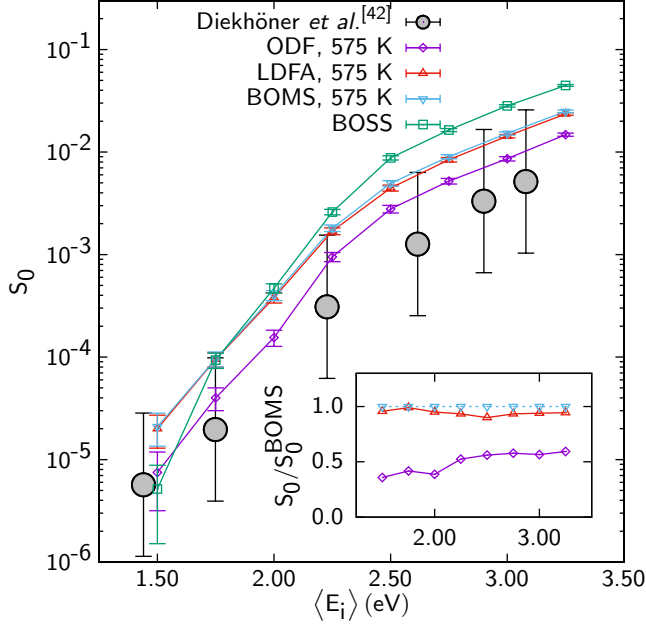
Figure 5.2: Reaction probability S_0 as a function of the average incidence energy $\langle E_i \rangle$ calculated with the ODF model from this work in combination with the HD-NNP potential energy surface [34] for a surface temperature $T_s = 575$ K (purple diamonds). Corresponding results from Shakouri et al. [30] based on the LDFA ($T_s = 575$ K, red triangles), adiabatic calculations for a mobile surface ($T_s = 575$ K) and a frozen surface, i.e. the BOMS (blue triangles) and the BOSS model (green squares). Experimental data from Diekhöner et al. [42] are shown for comparison (gray circles). The inset shows the ratio of reaction probabilities calculated with both electronic friction models relative to the corresponding adiabatic BOMS results.
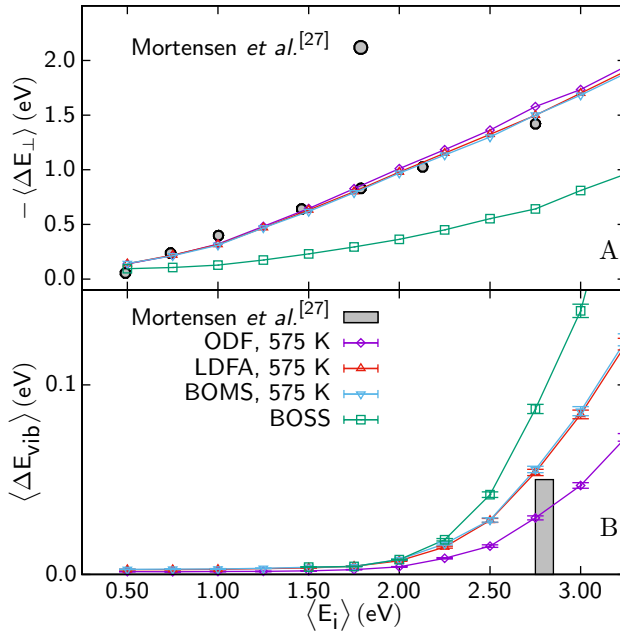
Figure 5.3: (A) Average energy uptake of the surface $\langle \Delta E_{\text{surface}} \rangle$ and (B) average change of the vibrational energy $\langle \Delta E_{\text{vib}} \rangle$ as a function of the average incidence energy $\langle E_i \rangle$ for molecules scattered from the surface. Using the HD-NNP PES from Ref. [34], results from adiabatic calculations according to the BOSS model (green squares), which does not account for energy dissipation by the surface, and a moving surface (blue triangles) as well as LDFA (red triangles) and ODF (purple diamonds) for a surface temperature $T_s = 575$ K are plotted. Experimental data from Mortensen et al. [27] (gray circles) are shown for comparison in (A). In (B), the maximum vibrational energy change of 0.05 eV at $\langle E_i \rangle = 2.8$ eV estimated in the same study [27] is indicated (gray bar).

Analyzing the energy exchange for N_2 scattering from Ru(0001) provides further insights into the strong effect of ODF. Figure 5.3A shows the average energy uptake $\Delta E_{\mathrm{surface}}$ of the Ru(0001) surface for N_2 scattering at different incidence energies. The BOMS model already yields semi-quantitative agreement with the experimental data, with the non-adiabatic energy dissipation channel as described by LDFA only resulting in a minor increase of $\Delta E_{\mathrm{surface}}$ by 3-4%.[30] ODF on the other hand increases $\Delta E_{\mathrm{surface}}$ by 15-20%, such that the energy losses are significantly closer to the experimental data from Mortensen et al. [27] at high incidence energies. In the same experiments, an upper bound of 0.05 eV has been obtained for the amount of vibrational excitation during N_2 scattering from Ru(0001) at $\langle E_{\mathrm{i}} \rangle = 2.8$ eV. Earlier calculations within the BOSS model [43] using a different RPBE-based PES[37] have significantly overestimated this energy transfer $\langle \Delta E_{\mathrm{vib}} \rangle$. As shown in Figure 5.3B, the new results reproduce this finding for BOSS-model-based simulations with the HD-NNP PES . Including surface mobility (BOMS) reduces the average vibrational excitation up to 50% at the highest incidence energies, but the results are not yet compatible with the upper bound estimated from the experiments. LDFA does not yield any further improvement. Quite in contrast, ODF leads to a further reduction of 50-60% for all incidence energies, such that only this electronic friction model is compatible with the experimental upper bound.

The big effect of ODF on the S_0 and the energy exchange of scattered molecules with the surface is due to the extremely large electronic friction acting on the motion towards the surface, along the N_2 bond axis as well as the strong coupling between the two, the latter of which is absent with the LDFA. Figures 5.4A-C show the corresponding friction elements η_{ZZ}, η_{dd} and η_{dZ}, respectively, along the minimum energy path q obtained by Shakouri et al. [30] for the HD-NNP PES used in this chapter. The ODF tensor elements for N_2 on Ru(0001) are more than five times larger than for H_2 on Cu(111) [23]. Furthermore, as has been observed before [16, 22, 23, 28], ODF predicts an increased friction along η_{dd} compared to LDFA, i.e. $\eta^{\mathrm{ODF}}_{dd} > 10\,\eta^{\mathrm{LDFA}}_{dd}$ in contrast to $\eta^{\mathrm{ODF}}_{ZZ} \approx 4\,\eta^{\mathrm{LDFA}}_{ZZ}$ at the transition state. Hence it is not surprising that any dynamics that involves N_2 bond activation, like dissociation on and inelastic scattering from the Ru(0001) surface, experiences a significantly larger concomitant
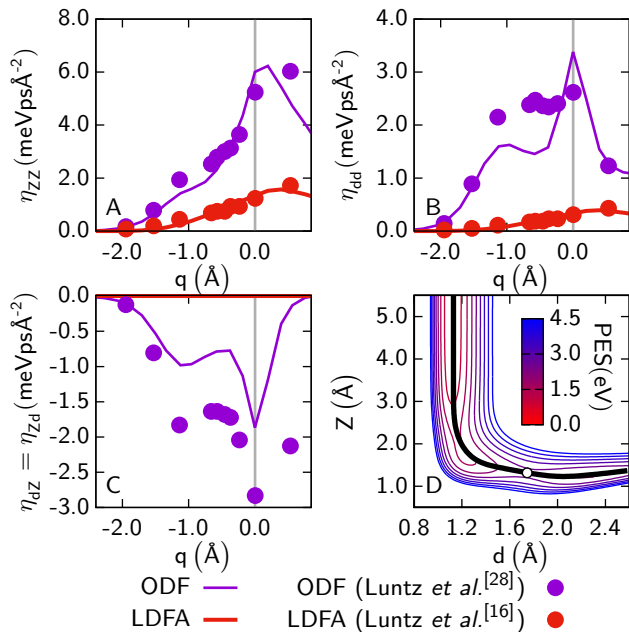
Figure 5.4: (A-C) Friction tensor elements related to the center of mass distance to the surface (η_{ZZ}), the bond length (η_{dd}) and the friction-induced coupling between these two (η_{dZ}), respectively, along the minimum energy path q for dissociative chemisorption over the bridge site in the bridge-to-hollow orientation with the molecular axis slightly tilted off parallel from the surface ($\theta = 84°$, see Figure 5.1 for the molecular coordinate system). This path is depicted in (D) together with the corresponding two-dimensional PES cut. The purple (red) lines indicate the electronic friction obtained for ODF (LDFA). Purple (red) dots show the ODF (LDFA) results from previous work of Luntz and Persson [16, 28]. The transition state for dissociation is located at the vertical gray line in (A-C) ($q = 0$ Å) and indicated by the empty circle in (D). Negative numbers up to transition state denote the approach from the gas-phase (i.e. decreasing Z above the surface). It should be noted that in Ref. [28] q is defined for the strictly parallel approach of the N_2 molecule towards the surface ($\theta = 90°$), but this does not correspond to the minimum energy path in our HD-NNP PES [30].

non-adiabatic energy loss with ODF than with LDFA. Luntz and Persson have already pointed out large differences between ODF and LDFA [16], but the dynamical model in their pioneering work only included two degrees of freedom of the N_2 molecule (Z and d). Our results for η_{ZZ}, η_{dd} and η_{dZ} slightly differ from theirs, but still maintain the same essential features that distinguish LDFA from ODF. In Sec. 5.C it is shown that these differences are related to a slightly different minimum energy path and the use of a different exchange-correlation functional.

5.4   Conclusion

In conclusion, for N_2 on Ru(0001), the new ODF approach, which includes non-adiabatic coupling of the motion in all six N_2 molecular degrees of freedom due to ehp excitations, yields a reduction of the dissociative chemisorption probability by about 50%. Such a large effect on a reaction probability has never been observed for MDEF calculations before, most of which have been based on the rivaling LDFA model. ODF agrees best with the best experimental estimates of S_0, but ODF and LDFA both agree within current error bars. ODF yields results for the energy transfer to the surface and vibrational excitation that are in significantly better agreement with the aforementioned experiments than the LDFA. Consequently, more accurate measurements of the reaction probabilities would allow to further develop theoretical modeling of non-adiabatic dynamics at metal surfaces – for example by including higher order perturbation terms (electron-mediated phonon-phonon coupling), which Novko et al. demonstrated to play a crucial role for the non-adiabatic vibrational damping of CO on Cu(100) [25, 44, 45]. Likewise, improvements of the exchange-correlation functional defining the PES might be required in order to achieve quantitative agreement [46, 47] with the more accurate experimental data to be measured. Given the importance of this system as a prototypical case of highly activated dissociative chemisorption, this would be an important step towards understanding whether and how non-adiabatic effects need to be accounted for in heterogeneous catalysis.

5.5 Computational Details

The orbital dependent electronic friction tensors have been obtained from density functional perturbation theory (DFPT)[48] results based on a computational setup similar to that in Chap. 4, which was used for H_2 on Cu(111) [23]. Briefly, DFPT calculations are performed as implemented in the Quantum Espresso package[49] for a 2x2 Ru(0001) slab with 5 layers employing the RPBE functional[35] as implemented in LibXC[50]. Using ONCV[51] pseudopotentials from the SG15[52] library together with a plane-wave cutoff of 816eV, a 18x18x1 k-point grid and a Gaussian envelope technique with a width of 0.6 eV for the sum over electronic states [19, 25] yields converged results for the friction tensor elements. A continuous representation of the 6x6 frozen-surface friction tensor was obtained using neural networks constructed with the help of the TensorFlow package[53]. Improving our previous approach[23], special care has been taken in order to ensure positive definiteness of the friction tensor and to keep the amount of neural network weight parameters as small as possible (3 hidden layers with 20 nodes each) by fitting all 21 independent friction tensor elements simultaneously.

Quasi-classical trajectory calculations with a time step of 0.3 fs were performed using the LAMMPS package [54], into which I have implemented an adaptation of the OVRVO algorithm [39]. At every time step, the OVRVO is applied by rotating to the six-dimensional coordinate system in which the ODF tensor is diagonal. The diagonal LDFA friction tensor is the same as in Ref. [30] and this new OVRVO implementation perfectly reproduces the results from that work. Likewise, the same equilibration procedure of the surface slab for generating initial conditions at $T_s > 0$ K is used.

5.A Additional Details on Dynamical Simulations

In the quasi-classical trajectory calculations, the incident velocity is Monte Carlo sampled from a flux-weighted velocity distribution describing the beams used in the experiments of Diekhöner et al. [42] as described in refs [30, 34]. Likewise, the other initial conditions are Monte Carlo sampled as described in ref [30]. Initial sticking probabilities S_0 are obtained by counting the number of trajectories that ended with

a N-N distance larger than 2.7 Å (i.e. more than 2.5 times the equilibrium distance in gas phase) and dividing it by the total number of trajectories. Trajectories are stopped and counted as scattered when N_2 molecules are reflected to distances more than 6 Å away from the surface. Like in Chap. 4, they are assigned a final rovibratioan state by binning first to the closest allowed angular momentum J while observing a $\Delta J =$ even selection rule, and second to the closest rovibrational energy with the previously obtained angular momentum, which is based on solving the 1-dimensional Schrödinger equation of the molecule in gas phase including rotational effects [23].

Consistent with previous calculations [43] and the analysis of the experiments [27], the average vibrational energy change is computed within the quasi-classical trajectory simulations according to

$$\langle \Delta E_{\mathrm{vib}} \rangle (E_{\mathrm{i}}) = \sum_{\nu_{\mathrm{f}}} P_{\nu_{\mathrm{f}}}(E_{\mathrm{i}}) \cdot (E_{\nu_{\mathrm{f}}} - E_0) \tag{5.2}$$

where $P_{\nu_{\mathrm{f}}}(E_{\mathrm{i}})$ is the probability of finding a scattered N_2 molecule with the initial vibrational state $\nu_{\mathrm{i}} = 0$ in the final rovibrational state $\nu_{\mathrm{f}} > 0$ and $J_{\mathrm{f}} \leq 13$ at incidence energy E_{i}. In order to disentangle rotational and vibrational energy, the vibrational excitation energy of a non-rotating N_2 molecule $E_{\nu_{\mathrm{f}}} - E_0$ is used, resulting from the quantum mechanical solution of the effectively one-dimensional part of the HD-NNP PES at molecule surface distance larger than 10 Å.

5.B Continuous Representation of the Orbital-Dependent Friction Tensor

5.B.1 Choice of Reference Angles θ_0 and ϕ_0

The same 4D+2D model [23] was used as in Chap. 4, with the same reference angles $\theta_0 = 90°$ and $\phi_0 = 90°$. Here the continuous representation of the 6x6 cartesian friction tensor depending on all 6 N_2 coordinates (see Fig.5.1), is constructed according to

$$\eta^{N_2}(\mathbf{R}) \approx T(\theta, \phi)\eta^{N_2}(X, Y, Z, d)T^{-1}(\theta, \phi), \tag{5.3}$$

where $T(\theta, \phi)$ is the appropriate rotation matrix and $\eta^{N_2}(X, Y, Z, d)$ is a 4D continuous neural network representation based on the center of mass coordinates of N_2 together with the bond distance using symmetry adapted coordinates [55, 56]. This ensures that our neural network representation yields a symmetry-compliant friction tensor.

Reactive trajectories

The angular distributions for reacted molecules (Figures 6a and 6b from Ref. [30]) show that the majority of the reactive trajectories follow the $\theta \approx 90°$ (or symmetrically equivalent orientation) and $\phi \approx 90°$ bridge reaction path. This is not surprising as this reaction path has by far the lowest barrier. Since the reaction probability is dominated by N_2 molecules approaching the surface at the chosen reference θ and ϕ, it is expected that this model works well for computing the reaction probabilities. Even though the argument here is that most reacted trajectories are at $\theta \approx 90°$ and $\phi \approx 90°$, for those that do not, the same argument as for the scattered trajectories, which are presented in the next section, can be used.

Scattered trajectories

Scattered trajectories are not limited to a $\theta \approx 90°$ and $\phi \approx 90°$ approach, however, the 4D+2D model is still appropriate using the following arguments. First of all, the difference in the magnitude between LDFA friction and ODF along the reaction path q as presented in Figure 5.4 is much larger than the differences between ODF at different orientations along q. We thus conclude that the large difference between LDFA and our isotropic ODF model will remain at least qualitatively.

In order to estimate the effect of the 4D+2D model on the dynamics, the friction element η_{dd} direction is considered for different orientations of N_2 along the reaction path in Figure 5.5 and 5.6 for rotated θ and ϕ respectively. Figure 5.5b shows the potential along the reaction path for different orientations along θ. Only at $\theta = 90°$ is a surmountable barrier present at q=0 Å while at other orientations the potential is essentially a repulsive wall. This means that N_2 molecules scattering from the surface at orientations different from $\theta = 90°$ do not approach the surface as closely and at

the same distance from the surface they will generally have a smaller velocity because of a repulsive force created by the potential. Since the energy dissipation rate, while neglecting the contribution from random forces, $\dot{E}_{\text{diss}}^{\text{N}_2}$ of N_2 at time t during a trajectory is proportional with the square of the velocity $\mathbf{v}^{\text{N}_2}$ according to

$$\dot{E}_{\text{diss}} = \mathbf{v}^{\text{N}_2}(t)\boldsymbol{\eta}^{\text{N}_2}(t)\mathbf{v}^{\text{N}_2}(t), \tag{5.4}$$

the energy loss for trajectories at different orientations than $\theta = 90°$ must be smaller and thus non-adiabatic effects are less important for those trajectories. When considering the friction tensor itself in Figure 5.5a, it can be seen that at orientations different from $\theta = 90°$ (using dashed lines) the friction tensor itself is smaller at least until the closest possible approach, for the largest incidence energy considered here, indicated by the gray dashed line.

For the anisotropy of η_{dd} for rotations along ϕ (Figure 5.6) essentially the same result as for Fig. 5.5 is found. At $\phi = 45°$ and $135°$, which are essentially identical, there is a barrier at $\mathsf{q}=0.25$ Å, although it is not dynamically accessible. The closest approach for orientations different from $\phi = 90°$ is closer to the transition state compared to θ and is 0.1 Å before the $\phi = 90°$ barrier. While at very close approaches the friction tensor in Figure 5.6 is higher for the $\phi = 90°$ orientation, the overall energy loss will still be an underestimation due to the friction being much lower for $\mathsf{q} < -0.3$ Å. Consequently, the 4D+2D model, which uses slightly smaller values for both $\theta = 90°$ and $\phi = 90°$ in all cases, underestimates the amount of friction and dissipated energy. Since the current model already reports a much larger effect of friction for ODF compared to LDFA, this underestimation would not change any of the conclusions and in fact, the non-adiabatic effects on the observables may be even (slightly) larger for this system than predicted.

5.B.2 Neural Network Fitting Accuracy

In this section the neural network (NN) fitting accuracy of the orbital dependent friction (ODF) elements is assessed. In contrast to the fitting procedure in Chap. 4 and the work by Jiang and coworkers [24], the friction elements independently [23] are not fitted
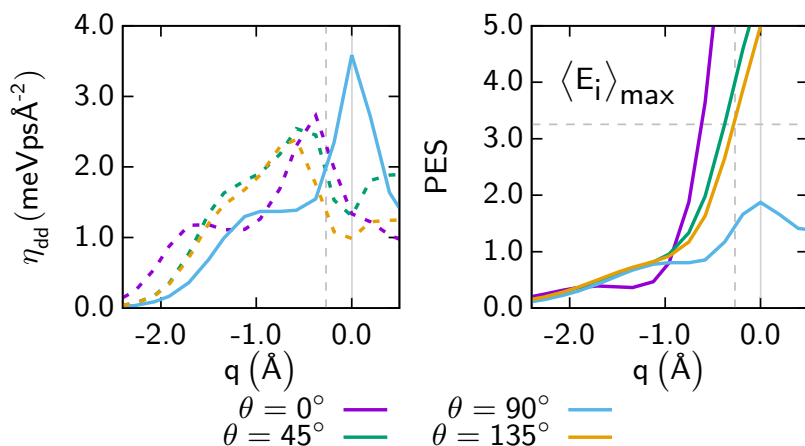
Figure 5.5: a) ODF along the reaction path for $\phi = 90°$, $X = \frac{1}{2}a$, $Y = 0$, and $\theta = 0°$ (purple), $45°$ (green), $90°$ (blue), $135°$ (orange). Orientations different from the reference rotation $\theta = 90°$ are shown using dashed lines since they are not included in the 4D+2D model. See Fig. 5.1 for the coordinate system. b) The potential energy is shown along the same reaction paths as in a). The vertical solid gray line is positioned at the barrier. The horizontal and vertical dashed gray lines indicate the largest $\langle E_i \rangle$ used in molecular dynamics simulations and the corresponding closest approach to the barrier, respectively, when $\theta \neq 90°$.
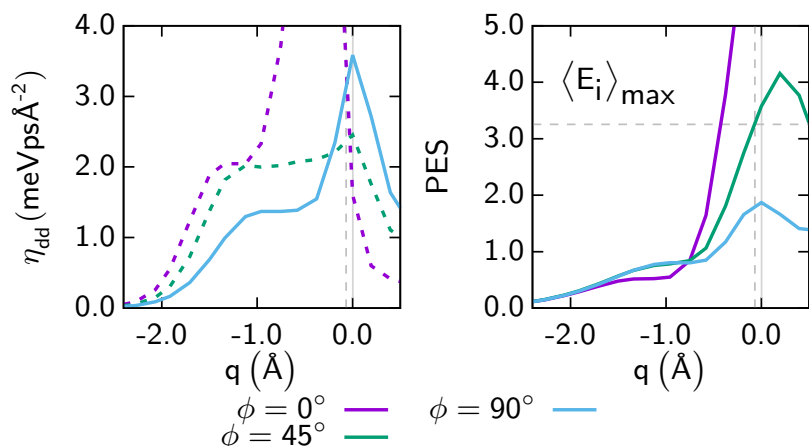
Figure 5.6: ODF along the reaction path for $\theta = 90°$, $X = \frac{1}{2}a$, $Y = 0$, and $\phi = 0°$ (purple), $45°$ (green), $90°$ (blue). Orientations away from the reference rotation $\phi = 90°$ are shown using dashed lines since they are not included in our isotropic friction model. See Fig.5.1 for the coordinate system. b) The potential energy is shown along the same reaction paths as in a). The vertical solid gray line is positioned at the barrier. The horizontal and vertical dashed gray lines indicate the largest $\langle E_i \rangle$ used in molecular dynamics simulations and the corresponding closest approach to the barrier, respectively, when $\phi \neq 90°$.

independently. Instead a single NN is used to fit all 21 independent friction elements simultaneously. To do this, 3 hidden layers ($N_{HL} = 3$) and 20 nodes ($N_{HN_i} = 20$) are used for each layer i together with an output layer of 21 nodes (N_{ON}). Subsequently, these 21 output nodes are arranged in the form of a lower triangular matrix. This ensures that a positive definite matrix is obtained as is required for finite temperature Langevin dynamics. A detailed discussion of the advantages of this approach will be the subject of a forthcoming publication. This construct is fitted using TensorFlow [53] to the friction elements obtained from DFPT.

By fitting only a single NN instead of 21 NNs the amount of free parameters (weights and biases) to be optimized is greatly reduced. The number of free parameters is determined according to

$$N_{IN} \cdot N_{HN_1} + N_{HN_1} + \sum_{i=1}^{N_{HL}-1} \left(N_{HN_i} \cdot N_{HN_{i+1}} + N_{HN_{i+1}} \right) + N_{HN_{N_{HL}}} \cdot N_{ON} + N_{ON}, \quad (5.5)$$

where N_{IN} is the number of (symmetry) input coordinates. Using 21 independent NNs with 2 hidden layers and 20 nodes a total of 21·961=20181 free parameters are obtained. Instead, when using a single NN with an additional hidden layer and 21 output nodes, only 1381 free parameters are required. Note that for each configuration of the molecule, 21 independent friction elements are obtained. It should be emphasized here that the additional third hidden layer is needed in order to fit all elements with a single NN. This method works because while the elements are indeed independent, their behavior with respect to the molecules degrees of freedom is similar.

Several NN fits (1 through 5) have been obtained for the ODF elements in order to assess possible under or overfitting, where the only difference is the random initialization of the free parameters. This is sometimes referred to as a NN committee [57, 58].

Fitting error In Figure 5.7 the fitting error is shown for all NN fits for both the test and train set. With friction tensors, however, it is not directly clear how to interpret the error. For example, when the fitted friction tensor is slightly rotated with respect to the DFPT friction tensor, the cartesian representation of the friction tensor may be

different by either a large or a small amount depending on the starting rotation and specific values of the friction elements. The error of the train set is for all fits similar, while there are some slight differences in the error of the test set, which suggests a slight overfitting. For fit 1 in Figure 5.7A there are some larger test errors from 0.5 to 4.0 meVpsÅ^{-2}. On the other hand, fit 2 in Figure 5.7B has larger test errors above the diagonal at negative friction and below the diagonal at positive friction. The other fits are very similar and have errors distributed approximately symmetrically around the diagonal.

Fitting error along the reaction path   In Fig. 5.8 a comparison is made for NN fits 1 and 5. Fig. 5.8 is the same as Fig. 5.4 and shows the result of two different fits in long and short dashed. For the friction elements η_{ZZ} and η_{dZ}, both neural networks predict the same result and are very close to the DFPT data. There is, however, a small discrepancy between both fits and the DFPT data 1Å before the barrier. Note that the points along the reaction path have not explicitly been included in the fitting data.

Dynamics for different neural network fits   Performing molecular dynamics with electronic friction using different NN fits for ODF exposes the actual error introduced to observables due to the above mentioned fitting errors. Figure 5.9 shows that dynamics performed for both fit 1 and fit 5 are within one standard error of each other for all computed incidence energies. Fit 1 (long dash) was used for all other presented dynamics of ODF.

Concluding remarks   From the dynamics performed on different fits in Figure 5.9 it is known that the errors reported here are small enough to obtain accurate dynamical observables for the N_2 on Ru(0001) system. Considering the different behavior of the test errors and the small influence on the dynamics, this amount of overfitting is negligible.
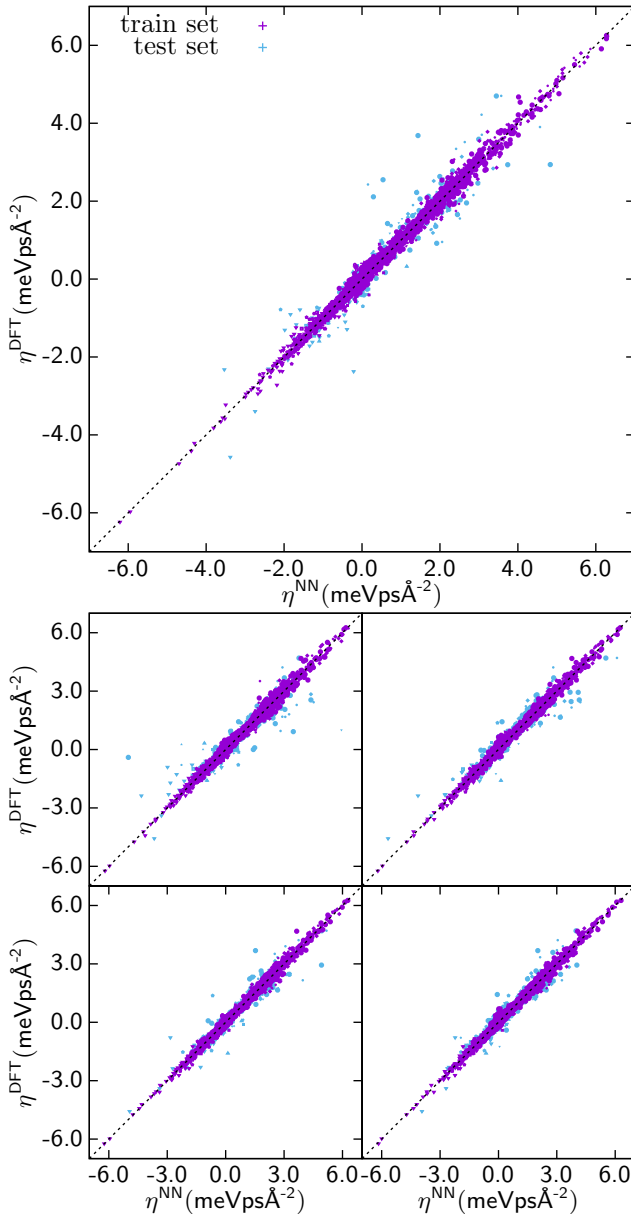
Figure 5.7: A-E show the correlation between the cartesian friction elements as calculated from DFPT (η^{DFT}) and NN fit 1 through 5, where the only difference between the fits is a different random initialization for the weights and biases.
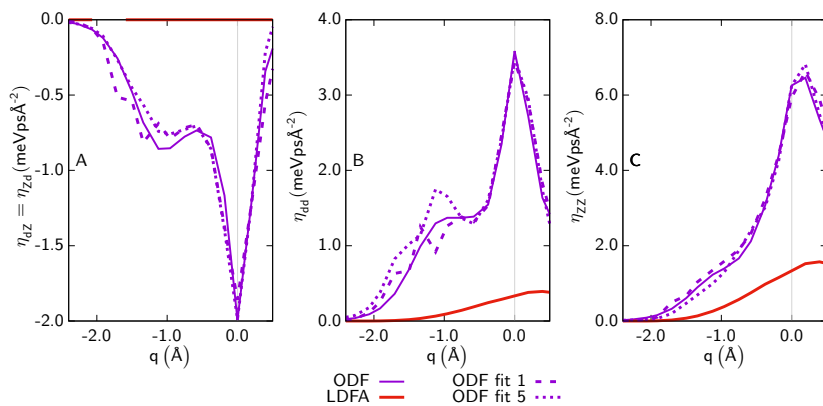
Figure 5.8: Same as Fig. 5.4. (A-C) show η_{dZ}, η_{dd} and η_{ZZ} in the molecular coordinate system, respectively, along the lowest minimum energy path for dissociative chemisorption over the bridge site (see Figure 5.1) for $\theta \approx 90°$ and $\phi \approx 90°$. ODF (solid-purple) and LDFA (solid-red) are from DFPT and DFT calculations respectively and are compared with fit 1 (long-dashed-purple) and fit 5 (short-dashed purple).

5
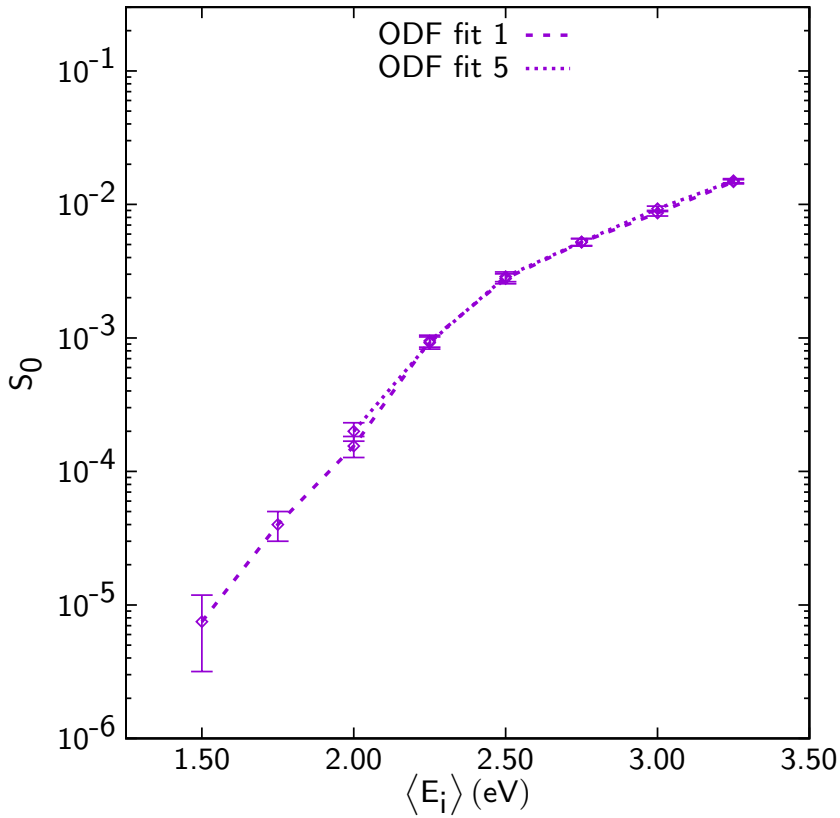
Figure 5.9: Same as Fig. 5.2. All calculated sticking probabilities are for surface atoms at a temperature of 575K. Results for fit 1 and 5 (see Figure 5.7) are in purple long dashed and short dashed respectively.

5.C   Comparison with Previous Work

5.C.1   Low-Dimensional Orbital-Dependent Friction

In Fig. 5.4A it is illustrated that the results obtained for η_{ZZ} from Luntz et al. are very similar to the results presented earlier in this chapter along the reaction path. For η_{dd} in Figure 5.4B the same trend is seen in both cases; a peak is found at $q = 0$ together with a smaller peak at lower q. However, the friction from Luntz et al. is higher in front of the transition state while lower at the transition state. In section 5.B.1 it is found that for molecules that are rotated at the transition state that the peak at the transition state is lower. This may explain why Luntz et al. find a lower peak at the transition state as their minimum energy path is apparently not the lowest minimum energy path. The increased friction at lower q can also be due to differences in the treatment of the electronic structure.

Figure 5.4C shows a large difference in the magnitude of η_{dZ}, however, the shape is very similar. To obtain η_{dZ}, Luntz and Persson [28] have computed the friction along a different direction and applied a rotation to obtain the off-diagonal element. However, for the new results in this chapter η_{dZ} is obtained directly, which together with the different treatment of the electronic structure as well as the different reaction path may explain the difference in magnitude.

It seems that Luntz et al. [16] have obtained a different minimum energy path as they argue that the ratio of $\eta_{dd} : \eta_{ZZ}$ is 1:4 in the case of LDFA, which is not necessarily true if the polar angle $\theta \neq 90°$. Instead, Shakouri et al. [34] have found that the lowest minimum energy path is tilted by 6° with respect to the surface for which the elbow plot is shown in Fig. 5.4D together with the obtained lowest minimum energy path and transition state. Differences in the minimum energy path may further be explained due to a different treatment of the electronic structure.

Considering the comparison above, the argument is that at worst the new implementation has slightly underestimated the ODF, which would result in a smaller effect of electron-hole pairs and does not at all influence any of the conclusions drawn henceforth. The new LDFA coefficients are almost identical to those from Luntz et al. As

5

has been observed before, ODF predicts an increased friction along η_{dd} compared to LDFA since $\eta_{ZZ}^{\text{ODF}} \approx 4\eta_{ZZ}^{\text{LDFA}}$ while $\eta_{dd}^{ODF} > 10\eta_{dd}^{LDFA}$ at the transition state.

5.C.2   Ehrenfest Dynamics on Ruthenium Nanoclusters

It is interesting to also compare the new MDEF with ODF results with Ehrenfest dynamics of N_2 on Ruthenium nanoclusters by Montemore et al. [9]. They computed an effective increase of the barrier height by 70 meV due to non-adiabatic energy dissipation for a single trajectory on a Ru_{147}, starting with approximately 1.4 eV kinetic energy along the reaction path towards the transition state for dissociation. Despite all the differences between the initial conditions, the PESs for N_2 on a Ru_{147} cluster and the Ru(0001) surface as well as the underlying non-adiabatic dynamical propagation techniques and statistical averaging, the aforementioned 70 meV is in good agreement with the non-adiabatic contribution to $\langle \Delta E_{\text{surface}} \rangle$ at $E_i \approx 1.4$ eV in Fig. 5.3A for the ODF simulations.

5

5.D   Electronic Temperature Effects

Next the effect of the electronic temperature by performing calculations with (T_{el}=575K) and without (T_{el}=0K) random forces is discussed. In Fig. 5.10, the corresponding results are shown for the initial sticking probability. There is no qualitative difference in the resulting reaction probability, however, when random forces are neglected, the sticking probability is further reduced compared to simulations without electronic friction between an incidence energy of 2.0 and 3.25 eV. Neglecting random forces at lower incidence energies seem to increase this difference but I have not calculated a sufficient amount of trajectories in order to substantiate it beyond the statistical error bars.

In Fig. 5.11 a) and b) the same trend is observed that electronic friction at T_{el}=0K further increases the differences compared to simulations without electronic friction: the energy exchange with the surface in Figure 5.11 a) is slightly larger for T_{el}=0K. Surprisingly, the absolute difference with T_{el}=575K is independent from the incidence energy E_i between 1.5 eV and 3.25 eV and the shift is constant although small enough to not consider the random forces important for the energy exchange with the surface. The vibrational energy, however, is half at 2.25 eV and thus the random forces play an important role in the description of the vibrational quenching.

5
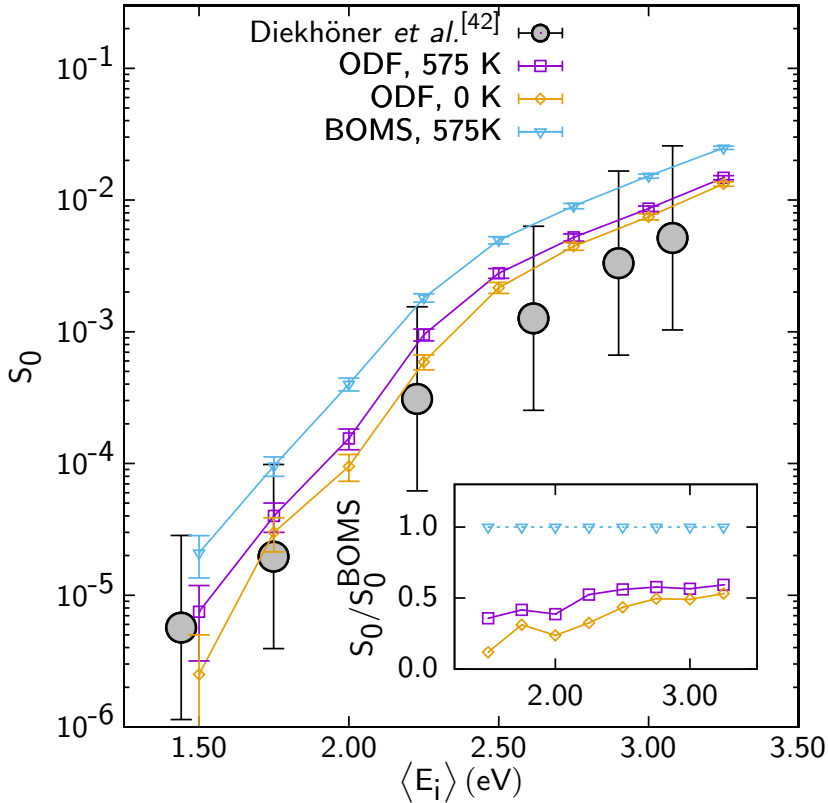
Figure 5.10: Same as Fig. 5.2. All calculated sticking probabilities are for surface atoms at a temperature of 575K. The "no friction" results (blue, BOMS previously in this chapter) is compared with ODF at an electronic temperature of 575K (purple, ODF previously in this chapter) and ODF at an electronic temperature of 0K (orange, neglecting random forces). Experimental sticking probabilities are the same as previously presented in this chapter. The inset shows the ratio of sticking probabilities with electronic friction turned on at T_{el} =0K and 575K with respect to the S_0 without friction
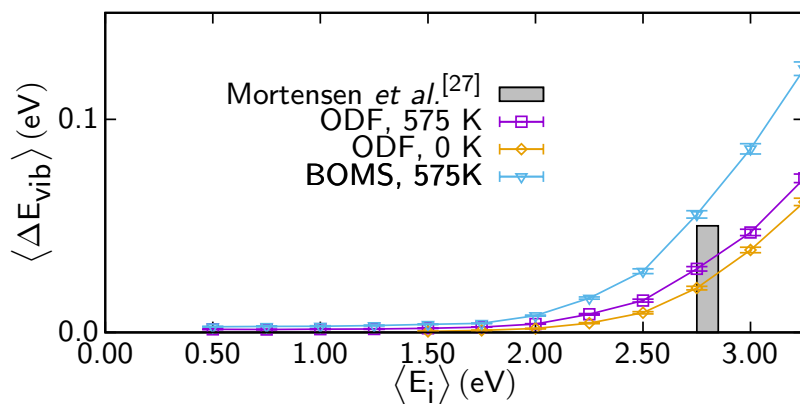
Figure 5.11: Same as Fig. 5.3. Both the energy exchange with the surface ($\langle \Delta E_{\mathsf{surface}} \rangle$) and the vibrational excitation energy ($\langle \Delta E_{\mathsf{vib}} \rangle$) have been obtained at a surface temperature of 575K The no friction results (blue, HD-NNP earlier in this chapter) is compared with HD-NNP+ODF at an electronic temperature of 575K (purple, HD-NNP+ODF earlier in this chapter) and HD-NNP+ODF at an electronic temperature of 0K (orange, neglecting random forces). Experimental energy exchanges and vibrational excitation energies are the same as earlier in this chapter.

5

References

[1] P. Spiering, K. Shakouri, J. Behler, G.-J. Kroes, and J. Meyer. "Orbital-Dependent Electronic Friction Significantly Affects the Description of Reactive Scattering of N_2 from Ru(0001)". In: *J. Phys. Chem. Lett.* 10 (2019), pp. 2957–2962. DOI: `10.1021/acs.jpclett.9b00523`.

[2] K. Reuter. "First-Principles Kinetic Monte Carlo Simulations for Heterogeneous Catalysis: Concepts, Status, and Frontiers". In: *Modeling and Simulation of Heterogeneous Catalytic Reactions*. John Wiley & Sons, Ltd, 2011, pp. 71–111. DOI: `10.1002/9783527639878.ch3`.

[3] K. Reuter. "Ab Initio Thermodynamics and First-Principles Microkinetics for Surface Catalysis". In: *Catal. Lett.* 146 (2016), pp. 541–563. DOI: `10.1007/s10562-015-1684-3`.

[4] J. D. White, J. Chen, D. Matsiev, D. J. Auerbach, and A. M. Wodtke. "Conversion of Large-Amplitude Vibration to Electron Excitation at a Metal Surface". In: *Nature* 433 (2005), pp. 503–505. DOI: `10.1038/nature03213`.

[5] M. Dell'Angela, T. Anniyev, M. Beye, R. Coffee, A. Föhlisch, et al. "Real-Time Observation of Surface Bond Breaking with an X-Ray Laser". In: *Science* 339 (2013), pp. 1302–1305. DOI: `10.1126/science.1231711`.

[6] H. Öström, H. Öberg, H. Xin, J. LaRue, M. Beye, et al. "Probing the Transition State Region in Catalytic CO Oxidation on Ru". In: *Science* 347 (2015), pp. 978–982. DOI: `10.1126/science.1261747`.

[7] D. Diesing and E. Hasselbrink. "Chemical Energy Dissipation at Surfaces under UHV and High Pressure Conditions Studied Using Metal–Insulator–Metal and Similar Devices". In: *Chem. Soc. Rev.* 45 (2016), pp. 3747–3755. DOI: `10.1039/C5CS00932D`.

[8] A. M. Wodtke. "Electronically Non-Adiabatic Influences in Surface Chemistry and Dynamics". In: *Chem. Soc. Rev.* 45 (2016), pp. 3641–3657. DOI: `10.1039/C6CS00078A`.

[9] M. M. Montemore, R. Hoyt, G. Kolesov, and E. Kaxiras. "Reaction-Induced Excitations and Their Effect on Surface Chemistry". In: *ACS Catal.* 8 (2018), pp. 10358–10363. DOI: `10.1021/acscatal.8b03266`.

[10] A. Peña-Torres, H. F. Busnengo, J. I. Juaristi, P. Larregaray, and C. Crespos. "Energy Dissipation Effects on the Adsorption Dynamics of N2 on W(100)". In: *J. Phys. Chem. C* 123 (2019), pp. 2900–2910. DOI: `10.1021/acs.jpcc.8b10173`.

[11] B. Hellsing and M. Persson. "Electronic Damping of Atomic and Molecular Vibrations at Metal Surfaces". In: *Phys Scr* 29 (1984), p. 360. DOI: `10.1088/0031-8949/29/4/014`.

5

[12] M. Head-Gordon and J. C. Tully. "Molecular Dynamics with Electronic Frictions". In: *J Chem Phys* 103 (1995), pp. 10137–10145. DOI: 10.1063/1.469915.

[13] J. I. Juaristi, M. Alducin, R. D. Muiño, H. F. Busnengo, and A. Salin. "Role of Electron-Hole Pair Excitations in the Dissociative Adsorption of Diatomic Molecules on Metal Surfaces". In: *Phys. Rev. Lett.* 100 (2008), p. 116102. DOI: 10.1103/PhysRevLett.100.116102.

[14] M. J. Puska and R. M. Nieminen. "Atoms Embedded in an Electron Gas: Phase Shifts and Cross Sections". In: *Phys. Rev. B* 27 (1983), p. 6121. DOI: 10.1103/PhysRevB.27.6121.

[15] J. I. Juaristi, M. Alducin, R. D. Muiño, H. F. Busnengo, and A. Salin. "Juaristi et al. Reply:" in: *Phys. Rev. Lett.* 102 (2009), p. 109602. DOI: 10.1103/PhysRevLett.102.109602.

[16] A. C. Luntz, I. Makkonen, M. Persson, S. Holloway, D. M. Bird, et al. "Comment on "Role of Electron-Hole Pair Excitations in the Dissociative Adsorption of Diatomic Molecules on Metal Surfaces"". In: *Phys. Rev. Lett.* 102 (2009), p. 109601. DOI: 10.1103/PhysRevLett.102.109601.

[17] S. P. Rittmeyer, J. Meyer, J. I. Juaristi, and K. Reuter. "Electronic Friction-Based Vibrational Lifetimes of Molecular Adsorbates: Beyond the Independent-Atom Approximation". In: *Phys. Rev. Lett.* 115 (2015), p. 046102. DOI: 10.1103/PhysRevLett.115.046102.

[18] O. Bünermann, H. Jiang, Y. Dorenkamp, A. Kandratsenka, S. M. Janke, et al. "Electron-Hole Pair Excitation Determines the Mechanism of Hydrogen Atom Adsorption". In: *Science* 350 (2015), pp. 1346–1349. DOI: 10.1126/science.aad4972.

[19] R. J. Maurer, M. Askerka, V. S. Batista, and J. C. Tully. "Ab Initio Tensorial Electronic Friction for Molecules on Metal Surfaces: Nonadiabatic Vibrational Relaxation". In: *Phys. Rev. B* 94 (2016), p. 115432. DOI: 10.1103/PhysRevB.94.115432.

[20] M. Askerka, R. J. Maurer, V. S. Batista, and J. C. Tully. "Role of Tensorial Electronic Friction in Energy Transfer at Metal Surfaces". In: *Phys. Rev. Lett.* 116 (2016), p. 217601. DOI: 10.1103/PhysRevLett.116.217601.

[21] M. Askerka, R. J. Maurer, V. S. Batista, and J. C. Tully. "Erratum: Role of Tensorial Electronic Friction in Energy Transfer at Metal Surfaces [Phys. Rev. Lett. 116, 217601 (2016)]". In: *Phys. Rev. Lett.* 119 (2017), p. 069901. DOI: 10.1103/PhysRevLett.119.069901.

5

[22] R. J. Maurer, B. Jiang, H. Guo, and J. C. Tully. "Mode Specific Electronic Friction in Dissociative Chemisorption on Metal Surfaces: H_2 on Ag(111)". In: *Phys. Rev. Lett.* 118 (2017), p. 256001. DOI: 10.1103/PhysRevLett.118.256001. arXiv: 1705.09753 [cond-mat.mtrl-sci].

[23] P. Spiering and J. Meyer. "Testing Electronic Friction Models: Vibrational De-Excitation in Scattering of H_2 and D_2 from Cu(111)". In: *J. Phys. Chem. Lett.* 9 (2018), pp. 1803–1808. DOI: 10.1021/acs.jpclett.7b03182.

[24] Y. Zhang, R. J. Maurer, H. Guo, and B. Jiang. "Hot-Electron Effects during Reactive Scattering of H_2 from Ag(111): The Interplay between Mode-Specific Electronic Friction and the Potential Energy Landscape". In: *Chem. Sci.* 10 (2019), pp. 1089–1097. DOI: 10.1039/C8SC03955K.

[25] D. Novko, M. Alducin, M. Blanco-Rey, and J. I. Juaristi. "Effects of Electronic Relaxation Processes on Vibrational Linewidths of Adsorbates on Surfaces: The Case of CO/Cu(100)". In: *Phys. Rev. B* 94 (2016). DOI: 10.1103/PhysRevB.94.224306.

[26] L. Diekhöner, L. Hornekær, H. Mortensen, E. Jensen, A. Baurichter, et al. "Indirect Evidence for Strong Nonadiabatic Coupling in N2 Associative Desorption from and Dissociative Adsorption on Ru(0001)". In: *J. Chem. Phys.* 117 (2002), pp. 5018–5030. DOI: 10.1063/1.1498476.

[27] H. Mortensen, E. Jensen, L. Diekhöner, A. Baurichter, A. C. Luntz, et al. "State Resolved Inelastic Scattering of N2 from Ru(0001)". In: *J. Chem. Phys.* 118 (2003), pp. 11200–11209. DOI: 10.1063/1.1575210.

[28] A. C. Luntz and M. Persson. "How Adiabatic Is Activated Adsorption/Associative Desorption?" In: *J. Chem. Phys.* 123 (2005), p. 074704. DOI: 10.1063/1.2000249.

[29] V. Smil. "Detonator of the Population Explosion". In: *Nature* 400 (1999), p. 415. DOI: 10.1038/22672.

[30] K. Shakouri, J. Behler, J. Meyer, and G.-J. Kroes. "Analysis of Energy Dissipation Channels in a Benchmark System of Activated Dissociation: N2 on Ru(0001)". In: *J. Phys. Chem. C* 122 (2018), pp. 23470–23480. DOI: 10.1021/acs.jpcc.8b06729.

[31] M. J. Murphy, J. F. Skelly, A. Hodgson, and B. Hammer. "Inverted Vibrational Distributions from N2 Recombination at Ru(001): Evidence for a Metastable Molecular Chemisorption Well". In: *J. Chem. Phys.* 110 (1999), pp. 6954–6962. DOI: 10.1063/1.478601.

[32] L. Diekhöner, H. Mortensen, A. Baurichter, and A. C. Luntz. "Laser Assisted Associative Desorption of N2 and CO from Ru(0001)". In: *J. Chem. Phys.* 115 (2001), pp. 3356–3373. DOI: 10.1063/1.1386810.

5

[33] C. Díaz, A. Perrier, and G. J. Kroes. "Associative Desorption of N2 from Ru(0 0 0 1): A Computational Study". In: *Chem. Phys. Lett.* 434 (2007), pp. 231–236. DOI: 10.1016/j.cplett.2006.12.016.

[34] K. Shakouri, J. Behler, J. Meyer, and G.-J. Kroes. "Accurate Neural Network Description of Surface Phonons in Reactive Gas–Surface Dynamics: N_2 + Ru(0001)". In: *J. Phys. Chem. Lett.* 8 (2017), pp. 2131–2136. DOI: 10.1021/acs.jpclett.7b00784.

[35] B. Hammer, L. B. Hansen, and J. K. Nørskov. "Improved Adsorption Energetics within Density-Functional Theory Using Revised Perdew-Burke-Ernzerhof Functionals". In: *Phys. Rev. B* 59 (1999), pp. 7413–7421. DOI: 10.1103/PhysRevB.59.7413.

[36] J. Behler, S. Lorenz, and K. Reuter. "Representing Molecule-Surface Interactions with Symmetry-Adapted Neural Networks". In: *J. Chem. Phys.* 127 (2007), p. 014705. DOI: 10.1063/1.2746232.

[37] C. Diaz, J. K. Vincent, G. P. Krishnamohan, R. A. Olsen, G. J. Kroes, et al. "Multidimensional Effects on Dissociation of N_2 on Ru(0001)". In: *Phys. Rev. Lett.* 96 (2006), p. 096102. DOI: 10.1103/PhysRevLett.96.096102.

[38] D. Novko, M. Blanco-Rey, M. Alducin, and J. I. Juaristi. "Surface Electron Density Models for Accurate *Ab Initio* Molecular Dynamics with Electronic Friction". In: *Phys. Rev. B* 93 (2016), p. 245435. DOI: 10.1103/PhysRevB.93.245435.

[39] D. A. Sivak, J. D. Chodera, and G. E. Crooks. "Time Step Rescaling Recovers Continuous-Time Dynamical Properties for Discrete-Time Langevin Integration of Nonequilibrium Systems". In: *J. Phys. Chem. B* 118 (2014), pp. 6466–6474. DOI: 10.1021/jp411770f.

[40] L. Verlet. "Computer "Experiments" on Classical Fluids. i. Thermodynamical Properties of Lennard-Jones Molecules". In: *Phys. Rev.* 159 (1967), p. 98. DOI: 10.1103/PhysRev.159.98.

[41] G. Bussi, D. Donadio, and M. Parrinello. "Canonical Sampling through Velocity Rescaling." In: *J. Chem. Phys.* 126 (2007), p. 014101. DOI: 10.1063/1.2408420.

[42] L. Diekhöner, H. Mortensen, A. Baurichter, E. Jensen, V. V. Petrunin, et al. "N2 Dissociative Adsorption on Ru(0001): The Role of Energy Loss". In: *J. Chem. Phys.* 115 (2001), pp. 9028–9035. DOI: 10.1063/1.1413746.

[43] C. Díaz, J. K. Vincent, G. P. Krishnamohan, R. A. Olsen, G. J. Kroes, et al. "Reactive and Nonreactive Scattering of N2 from Ru(0001): A Six-Dimensional Adiabatic Study". In: *J. Chem. Phys.* 125 (2006), p. 114706. DOI: 10.1063/1.2229197.

5

[44] D. Novko, M. Alducin, and J. I. Juaristi. "Electron-Mediated Phonon-Phonon Coupling Drives the Vibrational Relaxation of CO on Cu(100)". In: *Phys. Rev. Lett.* 120 (2018), p. 156804. DOI: 10.1103/PhysRevLett.120.156804.

[45] D. Novko, J. C. Tremblay, M. Alducin, and J. I. Juaristi. "Ultrafast Transient Dynamics of Adsorbates on Surfaces Deciphered: The Case of CO on Cu(100)". In: *Phys. Rev. Lett.* 122 (2019), p. 016806. DOI: 10.1103/PhysRevLett.122.016806.

[46] C. Díaz, E. Pijper, R. A. Olsen, H. F. Busnengo, D. J. Auerbach, et al. "Chemically Accurate Simulation of a Prototypical Surface Reaction: H2 Dissociation on Cu(111)". In: *Science* 326 (2009), pp. 832–834. DOI: 10.1126/science.1178722.

[47] F. Nattino, D. Migliorini, G.-J. Kroes, E. Dombrowski, E. A. High, et al. "Chemically Accurate Simulation of a Polyatomic Molecule-Metal Surface Reaction". In: *J. Phys. Chem. Lett.* 7 (2016), pp. 2402–2406. DOI: 10.1021/acs.jpclett.6b01022.

[48] S. Baroni, S. de Gironcoli, A. Dal Corso, and P. Giannozzi. "Phonons and Related Crystal Properties from Density-Functional Perturbation Theory". In: *Rev. Mod. Phys.* 73 (2001), pp. 515–562. DOI: 10.1103/RevModPhys.73.515.

[49] P. Giannozzi, S. Baroni, N. Bonini, M. Calandra, R. Car, et al. "QUANTUM ESPRESSO: A Modular and Open-Source Software Project for Quantum Simulations of Materials". In: *J Phys Condens Matter* 21 (2009), p. 395502. DOI: 10.1088/0953-8984/21/39/395502.

[50] M. A. L. Marques, M. J. T. Oliveira, and T. Burnus. "Libxc: A Library of Exchange and Correlation Functionals for Density Functional Theory". In: *Comput. Phys. Commun.* 183 (2012), pp. 2272–2281. DOI: 10.1016/j.cpc.2012.05.007.

[51] D. R. Hamann. "Optimized Norm-Conserving Vanderbilt Pseudopotentials". In: *Phys. Rev. B* 88 (2013), p. 085117. DOI: 10.1103/PhysRevB.88.085117.

[52] M. Schlipf and F. Gygi. "Optimization Algorithm for the Generation of ONCV Pseudopotentials". In: *Comput. Phys. Commun.* 196 (2015), pp. 36–44. DOI: 10.1016/j.cpc.2015.05.011.

[53] M. Abadi, A. Agarwal, P. Barham, E. Brevdo, Z. Chen, et al. "TensorFlow: Large-Scale Machine Learning on Heterogeneous Systems". In: (2015). Software available from tensorflow.org.

[54] S. Plimpton. "Fast Parallel Algorithms for Short-Range Molecular Dynamics". In: *J. Comput. Phys.* 117 (1995), pp. 1–19. DOI: 10.1006/jcph.1995.1039.

[55] J. Meyer. "Ab Initio Modeling of Energy Dissipation during Chemical Reactions at Transition Metal Surfaces". PhD thesis. Freie Universität Berlin, Freie Universität Berlin, Germany, 2012.

5

[56] I. Goikoetxea, J. Beltrán, J. Meyer, J. I. Juaristi, M. Alducin, et al. "Non-Adiabatic Effects during the Dissociative Adsorption of O_2 at Ag(111)? A First-Principles Divide and Conquer Study". In: *New J. Phys.* 14 (2012), p. 013050. DOI: 10.1088/1367-2630/14/1/013050.

[57] S. Manzhos and T. Carrington. "A Random-Sampling High Dimensional Model Representation Neural Network for Building Potential Energy Surfaces". In: *J. Chem. Phys.* 125 (2006), p. 084109. DOI: 10.1063/1.2336223.

[58] S. Manzhos, R. Dawes, and T. Carrington. "Neural Network-Based Approaches for Building High Dimensional and Quantum Dynamics-Friendly Potential Energy Surfaces". In: *Int. J. Quantum Chem.* 115 (2015), pp. 1012–1020. DOI: 10.1002/qua.24795.

5

Chapter 6

Machine-Learning based Continuous Representations of Electronic Friction Tensors

Abstract

Electronic friction theory allows to account for effects of electron-hole pair excitation on the dynamics of molecules on metal surfaces in a computationally efficient manner, given that continuous representations of the molecular-coordinate-dependent electronic friction tensors are available. In general, those tensors can be anisotropic and non-diagonal, which makes continuous representations more challenging than for scalar quantities, like e.g. potential energy surfaces. In this chapter neural-network-based machine learning models are developed and compared that account for symmetry properties of molecule-surface systems to meet this challenge. First, a formalism is presented to describe symmetry properties of electronic friction tensors for molecules on frozen metal surfaces. Two strategies result that allow these properties to be enforced within machine learning algorithms: an "*a priori*" and an "*a posteriori*" method. For the "*a priori*" method, different symmetry adapted input coordinates can affect the fitting accuracy and computational efficiency. The elements of the tensor can either be obtained by assigning a unique neural network to each element, or by constructing a neural network with multiple outputs and subsequently arrange these outputs as a tensor. Positive definite tensors can be enforced by generating a lower triangular tensor that is subsequently squared. Comparing different methods shows that the best results are obtained for an "*a priori*" method when including "asymmetric" contributions for the symmetry adapted input coordinates using a single neural network for all tensor elements and enforcing positive definiteness.

6.1 Introduction

Machine learning has become an ubiquitous technique in computational chemistry for the construction of continuous representations of quantities that depend on a large number of atomic coordinates based on first-principles calculations [1–14]. In particular potential energy surfaces (PESs) have received a lot of attention, usually in order to perform molecular dynamics (MD) simulations at considerably reduced computational cost [1, 5, 10, 12–14]. One essential ingredient for all machine learning models is the

representation of atomic coordinates, since it is the only way to rigorously enforce (spatial) symmetries of the studied systems (molecules, solids and/or interfaces) in the model [1, 5, 7, 10, 12, 15]. When PESs are the target quantities, it is "only" the invariance of these scalar quantities under the corresponding symmetry transformation that needs to be directly accounted for. Forces that are calculated as the partial derivatives with respect to the atomic coordinates from the machine learning model for the PES automatically conform to the proper symmetries [1, 15], but need more care to be represented accurately [2, 3, 5, 16]. On the other hand, making atomic forces the primary target quantities requires constructing and incorporating the symmetry-related invariance of vectors into a machine learning model, which is a much more difficult challenge, that Chmiela et al. [10, 16] have mastered only recently. For tensors the situation is even more challenging. In their recent work Grisafi et al. [6] have developed a machine learning model that includes symmetries of an atomistically described system for its "global" (intensive) property tensors (e.g. the 3×3 polarizability tensor).

The focus here is on the construction of machine learning models for electronic friction tensors. Given its computational efficiency, electronic friction theory [17] is the current workhorse for modeling the effect of electron-hole pair excitations in a metal surface on molecules moving close to the latter [18, 19]. These so-called non-adiabatic effects can considerably affect the vibrationally inelastic scattering of diatomic molecules [20–23] as well as their dissociation probabilities [24], when the electronic friction calculations are based on electronic structure theory that in principle allows them to be non-isotropic and non-diagonal (in their Cartesian representation) [25].

In that case, these so-called orbital-dependent friction (ODF) tensors are atom-specific (extensive) quantities, i.e. the amount of elements and coordinate dependence scales with the amount of atoms for which non-adiabatic effects are to be considered, which is a significant difference compared to the aforementioned work of [6]. At present, the computational burden of evaluating electronic friction tensors practically forbids including surface atom motion [20], which is currently considered to not significantly affect the non-adiabatic effects described by electronic friction.[26] Machine

6

learning models that capture the combined symmetry of diatomic molecules on highly-symmetric low-index metal surfaces are therefore currently the only way to calculate sufficiently many MD trajectories (based on a Langevin equation) as required to obtain observables that can be compared with experimental data [21–24].

The goal of this chapter is to formalize symmetry constraints for atom-specific tensors and subsequently obtain a method for constructing continuous representations via machine learning that incorporate the aforementioned symmetry - with a particular focus on ODF tensors for molecules interacting with frozen surfaces. Three key strategies of the latter are considered here.

The first strategy is the most straightforward one, where the neural network (NN) is expected to learn the symmetries from the presented data set. This approach can easily be enhanced by using the relevant symmetry operators to extend the training and test data sets. The subsequent fit will, however, not strictly obey the correct symmetry behavior because of the fitting error which is arbitrarily different also for symmetrically equivalent configurations. A further downside is that the training time increases substantially since a much larger data set is required.

The second strategy is to perform *a posteriori* correction to a non-symmetric NN fit in order to correct symmetry violations using an explicit symmetrization method. This approach results in fitting errors that are also symmetrized. Although the overall result is guaranteed to be exactly symmetric, the NN has to be evaluated multiple times at symmetrically equivalent configurations. This results in both increased training and evaluation times.

Finally, the third strategy, which is the most desirable, is to present an *a priori* symmetry-adapted model to the machine learning algorithm. Non-scalar quantities are the same at symmetrically equivalent configurations only after the appropriate well-defined mathematical transformation. Here a pragmatic approach is provided to construct the appropriate tensor transformations, which are validated by applying the second approach to the postulated model and verifying that that no symmetry violations were observed.

This chapter is structured as follows. First, symmetry properties of tensors are

introduced using an abstract formalism, which allows to selectively incorporate the aforementioned key strategies. Afterwards, this formalism is applied to construct NN-based continuous representations of electronic friction tensors that have recently been studied [21, 24]. Using the same reference data for training and test sets, the resulting fits thus allow one to compare practical performance of these machine learning models.

6.2 Tensor Field Properties of Systems with Symmetry

Here a systematic approach is provided for obtaining symmetry-constrained representations of tensor fields. These symmetric representations are obtainable by considering their behavior under coordinate transforms and impose this behavior on analytical expressions, such as NN fits. Specifically, the focus is on the imposed behaviour on tensor fields that transform in the same way as the electronic friction tensor, which has previously been obtained NN fits [21, 24]. In order to obtain these coordinate transformations, it is necessary to define the configuration $\mathbf{p}$ that describes the location of all atoms in the system. This $\mathbf{p}$, while in principle an abstract object, can be expressed in different coordinate systems. Two examples, which are commonly used in chemistry, are a Cartesian coordinate system, where each atom is described by its three Cartesian coordinates, and an internal coordinate system, where the center of mass (COM) of a group of atoms is used in combination with some measure of the relative positioning of the atoms in that group together with its orientation. Now let $\mathbf{R}$ and $\mathbf{R}'$ denote two such different coordinate systems where the atomic configuration $\mathbf{p}$ is expressed in the respective coordinates as $\mathbf{R_p}$ and $\mathbf{R'_p}$. Here the elements $R_\mathbf{p}^i$ and $R'^i_\mathbf{p}$ of $\mathbf{R}$ and $\mathbf{R}'$ then simply describe the same physical object in their respective different coordinate systems. Moreover, assume that a forward mapping $\hat{M}_{\mathbf{R}'}\mathbf{R_p} = \mathbf{R'_p}$ and a backward mapping $\hat{M}_\mathbf{R}\mathbf{R'_p} = \mathbf{R_p}$ exist, noting that these mappings would usually be non-linear.

Tensor field properties are then simply properties that are associated with a configuration $\mathbf{p}$ and that transform in a specific way when a different coordinate system is chosen. Some such properties, like the PES $V(\mathbf{p})$, do not have a transformation rule and can thus also be considered scalar fields ($V(\mathbf{p})$). Other properties of the system,

which are at least partially defined through a change in the configuration $\mathbf{p}$, do have associated transformation rules. Examples are velocities $\left[v^i\left(\mathbf{p}\right)\right]^{\mathbf{R}} = \frac{dR_{\mathbf{p}}^i}{dt}$ and forces $\left[F_i\left(\mathbf{p}\right)\right]_{\mathbf{R}} = -\frac{dV}{dR_{\mathbf{p}}^j}$. The elements of these properties are related to a change in the configuration $\mathbf{p}$ expressed in a specific coordinate system $\mathbf{R_p}$. It is convenient to be able to transform the elements of these properties to allow expressing them in a different coordinate system. Even though $\hat{M}_{\mathbf{R}'}$ (and $\hat{M}_{\mathbf{R}}$) in general do not describe linear transformations in the context of chemical systems (e.g. typically internal coordinates are given by distances and angles), the transformation of both the aforementioned differential properties is given by a point-wise linear transformation i.e.

$$\left[v^i\left(\mathbf{p}\right)\right]^{\mathbf{R}'} = \frac{dR_{\mathbf{p}}'^i}{dt} = \frac{\partial R_{\mathbf{p}}'^i}{\partial R_{\mathbf{p}}^j}\frac{dR_{\mathbf{p}}^j}{dt} = \frac{\partial R_{\mathbf{p}}'^i}{\partial R_{\mathbf{p}}^j}\left[v^j\left(\mathbf{p}\right)\right]^{\mathbf{R}} \tag{6.1}$$

for velocities and

$$\left[F_i\left(\mathbf{p}\right)\right]_{\mathbf{R}'} = \frac{dV}{dR_{\mathbf{p}}'^i} = \frac{\partial R_{\mathbf{p}}^j}{\partial R_{\mathbf{p}}'^i}\frac{dV}{dR_{\mathbf{p}}^j} = \frac{\partial R_{\mathbf{p}}^j}{\partial R_{\mathbf{p}}'^i}\left[F_j\left(\mathbf{p}\right)\right]_{\mathbf{R}} \tag{6.2}$$

for forces. Here Einstein's summation convention for implicitly summing over repeated indices is used. A tensor field such as the velocity $\boldsymbol{v}\left(\mathbf{p}\right)$ or force $\boldsymbol{F}\left(\mathbf{p}\right)$ can thus be defined invariant of the chosen coordinate system. Elements of these invariant velocity $\left[v^i\left(\mathbf{p}\right)\right]^{\mathbf{R}}$ and force $\left[F_i\left(\mathbf{p}\right)\right]_{\mathbf{R}}$ tensors can then be expressed for a specific coordinate system, this is indicated here explicitly using a bracket notation, as it will later be necessary to keep track of the coordinate system for introducing symmetry properties. Moreover, the elements of the force have a lower index to indicate that they transform covariantly, i.e. in the same way as the tangent vector basis (linearized) of the corresponding coordinate system, while the elements of the velocity have an upper index to indicate that they transform contravariantly, i.e. in the same way as the dual of the tangent vector basis.

Tensor fields can also describe properties that transform as a combination of co- and contravariant elements. An example of this is when the partial derivatives in equation 6.2 are written as the Jacobian tensor

$$\left[J_i^j\left(\mathbf{p}\right)\right]_{\mathbf{R}'}^{\mathbf{R}} = \frac{\partial R_{\mathbf{p}}^j}{\partial R_{\mathbf{p}}'^i} = \frac{\partial\left(\hat{M}_{\mathbf{R}}\mathbf{R}_{\mathbf{p}}'\right)^j}{\partial R_{\mathbf{p}}'^i}. \tag{6.3}$$

Here we focus on tensor fields that transform in the same way as the electronic friction tensor: the doubly covariant tensor field $\left[\eta_{ij} \left(\mathbf{p} \right) \right]_{\mathbf{RR}}$. The transformation rule for the elements of this type of tensor field from coordinate system $\mathbf{R}$ to $\mathbf{R}'$ is written as

$$\left[\eta_{i'j'} \left(\mathbf{p} \right) \right]_{\mathbf{R'R'}} = \left[J^i_{i'} \left(\mathbf{p} \right) \right]^{\mathbf{R}}_{\mathbf{R}'} \left[\eta_{ij} \left(\mathbf{p} \right) \right]_{\mathbf{RR}} \left[J^j_{j'} \left(\mathbf{p} \right) \right]^{\mathbf{R}}_{\mathbf{R}'}, \tag{6.4}$$

with indices i, j and i', j' denoting tensor elements in the R and R' coordinate systems respectively. Here and in the following, the use of the Einstein summation convention for these tensor elements is limited to indices that appear exactly once covariantly and once contravariantly, while they are expressed in the same basis.

Some systems also have symmetries, which means that there exist symmetrically equivalent configurations that have equivalent tensors. Equivalent for tensor fields however, does not mean that all the elements of the tensor are the same. For example, if a mirror symmetry exists then the symmetrically equivalent configurations have the same forces, except that the forces are additionally mirrored themselves, or equivalently, the coordinate basis is mirrored and the same force is now found in this symmetry coordinate system as illustrated in Figure 6.1. This can be elegantly expressed using the above tensor field transformations.

Let $\hat{s}$ be a symmetry operator that generates the symmetrically equivalent configuration $\mathbf{p}_{\hat{s}}$ of $\mathbf{p}$ and $\hat{M}_{\hat{s}\mathbf{R}}$ be the mapping which obtains the concomitant symmetry coordinate system of $\hat{s}$. Following the above reasoning, the elements of a symmetric tensor field then must be the same at configurations $\mathbf{p}$ and $\mathbf{p}_{\hat{s}}$ if the latter is expressed in the mapped coordinate system according to

$$\hat{s} \left[\eta_{ij} \left(\mathbf{p} \right) \right]_{\mathbf{RR}} = \left[\eta_{ij} \left(\mathbf{p}_{\hat{s}} \right) \right]_{\hat{s}\mathbf{R}\hat{s}\mathbf{R}} = \left[\eta_{ij} \left(\mathbf{p} \right) \right]_{\mathbf{RR}} \ \forall \ \hat{s} \ \in \ G. \tag{6.5}$$

This equivalence holds for all symmetry operators $\hat{s}$ in the group G that together describe the symmetry of the system. By making use of equation 6.4 it is possible to write $\hat{s}\boldsymbol{\eta} \left(\mathbf{p} \right)$ expressed in the original coordinate system R according to

$$\hat{s} \left[\eta_{ij} \left(\mathbf{p} \right) \right]_{\mathbf{RR}} = \left[J^{i'}_i \left(\mathbf{p}_{\hat{s}} \right) \right]^{\mathbf{R}}_{\hat{s}\mathbf{R}} \left[\eta_{i'j'} \left(\mathbf{p}_{\hat{s}} \right) \right]_{\mathbf{RR}} \left[J^{j'}_j \left(\mathbf{p}_{\hat{s}} \right) \right]^{\mathbf{R}}_{\hat{s}\mathbf{R}}, \tag{6.6}$$
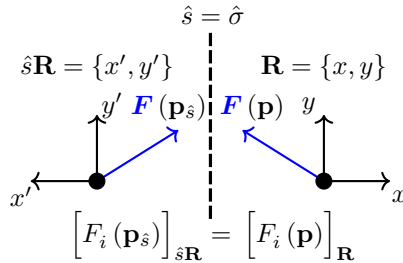
149

Figure 6.1: Schematic explanation of the behavior of tensors (force $\boldsymbol{F}(\mathbf{p})$) if a mirror symmetry (indicated by the dashed black line) $\hat{\sigma}$ can be identified. On the right hand side of the mirror, the original configuration $\mathbf{p}$ is indicated together with the force $\boldsymbol{F}(\mathbf{p})$ and Cartesian coordinate system $\mathbf{R} = \{x, y\}$. The left hand side shows the symmetrically equivalent configuration $\mathbf{p}_{\hat{s}}$ which has the mirrored force $\boldsymbol{F}(\mathbf{p}_{\hat{s}})$ that has the same elements as $\boldsymbol{F}(\mathbf{p})$ if they are expressed in the symmetry coordinate system $\hat{s}\mathbf{R} = \{x', y'\}$ and the Cartesian coordinate system $\mathbf{R}$ respectively.

where if $\mathbf{R}$ is taken in cartesian coordinates then the resulting Jacobian tensor $\boldsymbol{J}(\mathbf{p}_{\hat{s}})$ is independent of $\mathbf{p}$ and equal to the appropriate transformation matrix describing the symmetry operator $\hat{s}$.

A continuous representation of a tensor field $\boldsymbol{\eta}^{\text{cont}}(\mathbf{p})$ can thus be symmetrized *a posteriori* by taking the average over the h symmetrically equivalent configurations under the symmetry operators in G, represented in the appropriately rotated basis, according to

$$\left[\eta_{ij}^{\text{post}}(\mathbf{p})\right]_{\mathbf{R}\mathbf{R}} = \frac{1}{h}\sum_{\hat{s}\in G}\hat{s}\left[\eta_{ij}^{\text{cont}}(\mathbf{p})\right]_{\mathbf{R}\mathbf{R}} = \frac{1}{h}\sum_{\hat{s}\in G}\left[\eta_{ij}^{\text{cont}}(\mathbf{p}_{\hat{s}})\right]_{\hat{s}\mathbf{R}\hat{s}\mathbf{R}}. \tag{6.7}$$

The other way round, equation 6.7 also provides a test for a candidate tensor construction $\boldsymbol{\eta}^{\text{cand}}(\mathbf{p})$ which is intended to already have the correct symmetry behavior. If it can be shown that this test is passed based on analytical arguments then this is considered an *a priori* symmetrized tensor $\boldsymbol{\eta}^{\text{priori}}(\mathbf{p})$. In practice, this can also be verified by a numerical test on a sufficiently large grid of configurations, or be used as an estimate of how large the violation of symmetry is (e.g. in comparison with the fitting error of $\boldsymbol{\eta}^{\text{cand}}(\mathbf{p})$).

A special case exists when a configuration exists that is invariant under one of the symmetry operators $\hat{s}$ such that independent of the chosen coordinate system it is found that $\mathbf{R_p} = \hat{s}\mathbf{R_p} = \mathbf{R_{p^{\text{seam}}}}$. Example of such configurations are the fixed points (as present on the dashed line in Figure 6.1) on a mirror plane. These configurations consist along what is defined here as the symmetry seam, which would in the case of a mirror plane be the entire mirror plane, and have additional constraints on their elements. The constraints on the elements can be found by using the relevant $\hat{s}$ in equation 6.5 as

$$\left[\eta_{ij}\left(\mathbf{p}^{\text{seam}}\right)\right]_{\mathbf{RR}} = \left[\eta_{ij}\left(\mathbf{p}^{\text{seam}}\right)\right]_{\hat{s}\mathbf{R}\hat{s}\mathbf{R}}, \tag{6.8}$$

and realize that the constraints are now imposed due to the equivalence being required for the exact same configuration, i.e. the same tensor is required to be the same in two (or more) coordinate systems. These symmetry constraints are automatically satisfied for both *a priori* and *a posteriori* tensor constructions.

6.2.1 *a priori* Symmetric Coordinate Systems and Mappings

There are several methods to obtain an *a priori* symmetric tensor field $\boldsymbol{\eta}^{\text{priori}}\left(\mathbf{p}\right)$ by choosing an appropriate coordinate system and concomitant mapping from and to Cartesian coordinates. The general idea is to obtain the tensor elements in a coordinate system $\mathbf{R}^{\text{sym}}$ which for symmetry equivalent configurations $\mathbf{p}_{\hat{s}}$ yields the same elements in the representation of that coordinate system i.e. $(R^{\text{sym}})^i_{\mathbf{p}_{\hat{s}}} = (R^{\text{sym}})^i_{\mathbf{p}}$. After this representation is obtained (e.g. through fitting a NN) it can then be transformed to the required coordinate system $\mathbf{R}$ using Eq. 6.4. For fitting it is not strictly necessary to have a well defined backwards mapping because forward mapping in combination with back-propagation (as implemented automatically in TensorFlow) can circumvent the need to transform the fitting data into the $\mathbf{R}^{\text{sym}}$ representation.

Reduced Dimensional Mapping

By choosing a reduced dimensional dependence on the configuration it is possible to avoid some of the symmetry considerations, although at the cost of having a lower

6

fitting accuracy. This can be done by defining a reference configuration $\mathbf{p}^{\mathsf{ref}}$ to be the same as the actual configuration $\mathbf{p}$ except for one (or possible multiple) direction(s) of a certain coordinate system $\mathbf{R}^{\mathsf{ref}}$ being a reference constant. A tensor can then be expressed in a different coordinate system $\mathbf{R}$ but including the imposed reduction in dependence in the reference coordinate system according to

$$
\left[\eta_{ij}^{\mathsf{ref}}\left(\mathbf{p}\right)\right]_{\mathbf{R}\mathbf{R}} = \underbrace{\left[J_i^k\left(\mathbf{p}\right)\right]_{\mathbf{R}}^{\mathbf{R}^{\mathsf{ref}}} \left[J_k^m\left(\mathbf{p}^{\mathsf{ref}}\right)\right]_{\mathbf{R}^{\mathsf{ref}}}^{\mathbf{R}}}_{\left[T_i^m\left(\mathbf{p},\mathbf{p}^{\mathsf{ref}}\right)\right]_{\mathbf{R}}^{\mathbf{R}}} \left[\eta_{mn}^{\mathsf{ref}}\left(\mathbf{p}^{\mathsf{ref}}\right)\right]_{\mathbf{R}\mathbf{R}} \left[J_l^n\left(\mathbf{p}^{\mathsf{ref}}\right)\right]_{\mathbf{R}^{\mathsf{ref}}}^{\mathbf{R}} \left[J_j^l\left(\mathbf{p}\right)\right]_{\mathbf{R}}^{\mathbf{R}^{\mathsf{ref}}}.
$$

$$(6.9)$$

For this approximation to work, the dependence of the tensor on the coordinate direction that is kept constant must be sufficiently small.

Piece-Wise Mapping

A piece-wise mapping is obtained by defining a region of the configuration space, the irreducible wedge, that has the property that starting from that region it is possible to access the entire configuration space by only applying consecutive symmetry operations. The piece-wise mapping is then constructed to map any configuration $\mathbf{p}$ to the irreducible wedge $\mathbf{p}^{\mathsf{irr}}$. In practice this can be done by applying consecutive symmetry operations until a configuration within the irreducible wedge is found. The tensor only needs to be fitted within this irreducible wedge and if the queried configuration is outside the irreducible wedge then the tensor can be unfolded using Equation 6.4.

While this method does obtain the correct symmetry of the system, there is no *a priori* reason for the behavior at the symmetry seam (which coincides with the boundary of such a irreducible wedge) to be correct. This becomes immediately clear by using the example of mirror symmetry in Figure 6.1. A piece-wise mapping procedure would assign an identity rotation when the configuration is still in the irreducible wedge and an infinitesimally small distance from the mirror plane while it would assign a mirror if it is an infinitesimally small distance on the other side of the mirror plane. This imposes, in this particular case, that the x component of the force tensor is exactly zero. If this is not the case then a discontinuity occurs, as in, the x component of the

force tensor would be positive on one side of the mirror plane and negative on the other side. Doubly covariant tensors would e.g. have such discontinuities in the off-diagonal xy and yx components in this case.

The symmetry seam is only a small region and the violation can be kept under control by appropriately generating the data for a fitting procedure (i.e. provide enough data at the symmetry seam) and as such this method can still be effectively used in practice when proper care is taken.

Symmetry Adapted Coordinate Mapping

It is also possible to obtain a continuous mapping that can take into account the correct symmetry behavior. Let us assume a coordinate system $\mathbf{Q}$ exists that is invariant to any choice of symmetrically equivalent configuration $\mathbf{p}_{\hat{s}}$ such that $Q^i_{\mathbf{p}_{\hat{s}}} = Q^i_{\mathbf{p}}$ for all $\mathbf{p}$ and $\hat{s}$. Examples of such coordinates are symmetry adapted coordinates[27], permutation invariant polynomials [12] and the atom centered symmetry functions of Behler and Parinello [15].

If the tensor $\boldsymbol{\eta}^{\mathsf{sym}}(\mathbf{p})$ is expressed in this $\mathbf{Q}$ and its dependence on $\mathbf{p}$ is additionally constrained to yield the same tensor at configurations that are expressed the same in $\mathbf{Q}$ (i.e. $\boldsymbol{\eta}^{\mathsf{sym}}(\mathbf{Q_p})$) it automatically becomes an *a priori* symmetric tensor in any coordinate system $\mathbf{R}$. This is verified using Equation 6.4 to express $\boldsymbol{\eta}^{\mathsf{sym}}(\mathbf{Q_p})$ as the candidate tensor in Equation 6.7 according to

$$\left[\eta^{\mathsf{sym}}{}_{ij}(\mathbf{p})\right]_{\mathbf{RR}} = \frac{1}{h}\sum_{\hat{s}\in G} \underbrace{\left[J^{i'}_{i}(\mathbf{p}_{\hat{s}})\right]^{\mathbf{Q}}_{\hat{s}\mathbf{R}} \left[\eta_{i'j'}(\mathbf{Q_p})\right]_{\mathbf{QQ}} \left[J^{j'}_{j}(\mathbf{p}_{\hat{s}})\right]^{\mathbf{Q}}_{\hat{s}\mathbf{R}}}_{\left[\eta^{\mathsf{sym}}{}_{ij}(\mathbf{p}_{\hat{s}})\right]_{\hat{s}\mathbf{R}\hat{s}\mathbf{R}}}, \qquad (6.10)$$

where $\hat{s}\mathbf{Q}$ has been substituted with $\mathbf{Q}$ since they are the same by definition ($\mathbf{Q}_{\mathbf{p}_{\hat{s}}} = \mathbf{Q_p}$). Since the elements of $\left[J^{i'}_{i}(\mathbf{p}_{\hat{s}})\right]^{\mathbf{Q}}_{\hat{s}\mathbf{R}}$ are the same for any $\hat{s}$ due to substitution (see Equation 6.3), all terms in the sum are equivalent and $\boldsymbol{\eta}^{\mathsf{sym}}(\mathbf{p})$ passes the symmetry test.

Here at symmetry equivalent configurations $\mathbf{p}$ and $\mathbf{p}_{\hat{s}}$, the evaluation of $\boldsymbol{\eta}$ in the $\mathbf{Q}$ basis is the same, however, while $Q^i_{\mathbf{p}_{\hat{s}}} = Q^i_{\mathbf{p}}$, the Jacobian tensor (and thus the partial derivatives) are not. In fact, this exactly accounts for the transformation that

is expected to occur on the tensor after a symmetry operation.

The gain of using this method is that the tensor needs to be evaluated only once and not for every symmetry operator as would be the case for the *a posteriori* method, speeding up the evaluation by a factor equal to the number of available symmetries.

Naively, one may expect to be able to fit any tensorfield using this method, however this is not true for tensors of order two or higher. In those cases, the tensorfields transform as products of lower order tensorfields and thus also allow for asymmetric contributions when the product is again symmetric. Thus using only a symmetric mapping yields to the following problem. If the partial derivative $\frac{\partial Q_i(\mathbf{R})}{\partial \mathbf{R}_j} = 0$ for any element, which always occurs exactly where the space is symmetric since moving from such a symmetry seam yields the same value for $\mathbf{Q}$ in either direction (yielding zero derivatives), a cross like shape of zeros is formed in a second order tensor due to multiplying from both sides with a Jacobian which has a row of zeros. However, non-zero values are allowed at the crossings of these rows and columns of zeros if one also includes the product of asymmetric contributions. As a consequence, this method is not able to fit all possible tensorfields. It is important to note that these crosses of zeros only appear if some index of the tensor is along the same direction as the partial derivative, otherwise, they are hidden as a linear dependence of two (or more) such directions. In those cases, they still prevent this method from fitting all possible tensors. This issue can be solved using asymmetric transformations.

Symmetry Adapted Coordinate Mapping with Asymmetric Transformations

To solve the issue for tensors of order two or higher, following solution is proposed.

Assume that a set of n tensor fields $\left\{ \boldsymbol{J}^{\mathsf{A,B,C,\cdots}}(\mathbf{p}) \right\}$ exists such that any symmetry operator $\hat{s}$ only creates a permutation of the set and that at any $\mathbf{p}$, for any element ij, at least one tensor element of the tensors in this group is non zero. Moreover, the sum of these tensor fields are required to yield a tensor field that imposes the same constraints as the Jacobian tensor field in the symmetry adapted coordinate mapping does.

We can now define a tensor, for which we will check whether it is invariant under

the symmetrisation procedure

$$\left[\eta^{\text{test}}_{ij}\left(\mathbf{p}\right)\right]_{\mathbf{RR}} \quad = \quad \frac{1}{n}\sum_{\text{a}}^{\text{A,B,C,..}}\left[J^{\text{a}i'}_{i}\left(\mathbf{p}\right)\right]^{\mathbf{Q}}_{\mathbf{R}}\left[\eta_{i'j'}\left(\mathbf{Q_p}\right)\right]_{\mathbf{QQ}}\left[J^{\text{a}j'}_{j}\left(\mathbf{p}\right)\right]^{\mathbf{Q}}_{\mathbf{R}}. \quad (6.11)$$

Now since the symmetry operator $\hat{s}$ permutes only the terms of the sum in eq. 6.11, the test tensor is invariant under the symmetrisation and is thus already symmetric. The asymmetric tensor model thus consists of asymmetric terms that after addition form a symmetric model even when symmetry operators are applied. It should be noted here that the individual assymetric terms are technically not tensors themselves as only the sum of all terms transforms as a tensor.

6.3 Machine Learning Models for Orbital-Dependent Friction Tensors

This section describes the details on how to implement the *a priori* and *a posteriori* symmetric tensor fields in a machine-learning framework.

Neural Network architectures for tensor fields that reproduce the correct symmetry behaviour result in complex designs. First the hidden layer, which contains all the fitting parameters is explained. Then two different ways to obtain a order two tensor from such a hidden layer are shown. Next, a method is given to obtain a symmetric order two tensor (this is not the same as a tensor field with the correct symmetry behaviour), i.e. the two indices permute $\eta_{ij} = \eta_{ji}$. Finally, the correct symmetry behaviour is obtained by either using *a priori* or *a posteriori* architectures.

In this chapter, neural networks are a part of the building blocks used to design the algorithms for continuous representations of tensors. As such, these building blocks are henceforth refered to as hidden networks. The hidden networks used in this chapter (see Figure 6.2c) are constructed from L hidden layers (see Figure 6.2b) L^{l} labeled with l together with an output layer L^{out}. Each layer consists of N_l nodes (see Figure 6.2a) $\mathsf{N}^{l}_{n_l}$ where the output of the n_lth node defines the n_lth output of the lth layer. The number of inputs (M_l) in each layer is equal to the number of outputs from the
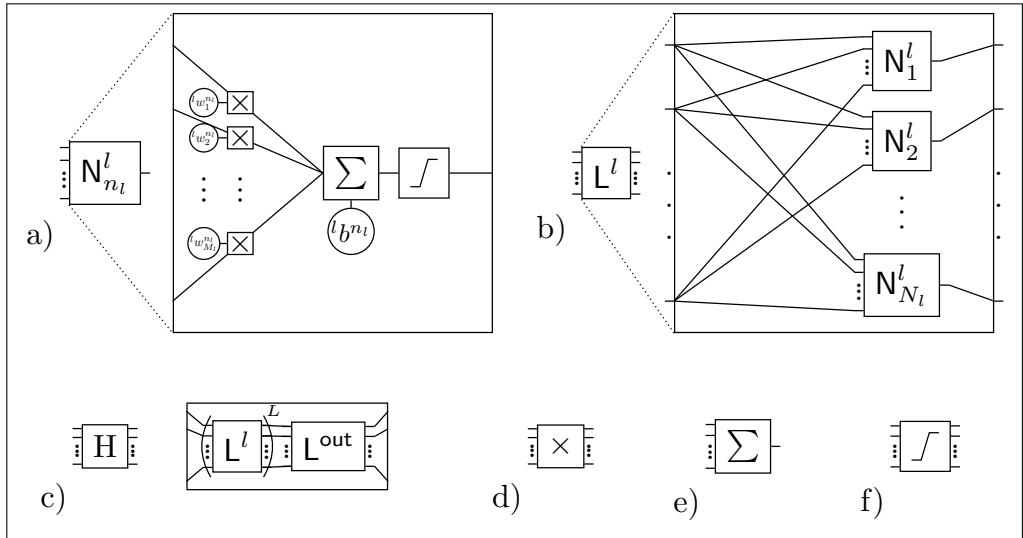
155

Figure 6.2: Schematic representation of the structure of a hidden network. a) Shows the inner structure of a node. b) Shows how nodes make up a layer. c) Shows how consequetive hidden and output layers make up a hidden network. d) Multiplication operator: multiplies two numbers. e) Sum operator that takes any amount of inputs and yields the sum. f) Activation function $F^{(l)}$.

previous layer $M_l = M_{l-1}$ except for the first layer which uses the N_0 inputs to the hidden network. Inputs of layer l are used for each node N_l in that layer and are first multiplied (see Figure 6.2d) with the weights ${}^l w_{m_l}^{n_l}$ after which the result is summed (see Figure 6.2e) and added to the bias ${}^l b^{n_l}$. Finally this sum is used as the argument of an activation function (see Figure 6.2f) F^l according to

$$y_{n_l} = F^l \left({}^l b^{n_l} + \sum_{m_l}^{M_l} {}^l w_{m_l}^{n_l} x_{m_l} \right). \tag{6.12}$$

The activation function $F^l(x)$ is chosen as the hyperbolic tangent $\tanh(x)$ for all hidden layers and as the linear function $f(x) = x$ for the output layer. Only the weights and biases are optimized during the training routine and not the architecture itself.

In order to obtain the 21 independent elements of an electronic friction tensor (in 6D), it is necessary to either fit one hidden network with 21 outputs or 21 hidden

networks with 1 output as is shown by the choice between option 1a and 1b in Figure
6.3. Once the 21 independent elements are obtained, they have to be arranged either as
a symmetric tensor directly or as a lower triangular tensor and subsequently multiplied
with its transpose. The latter method yields a positive-definite tensor which ensures
that for any velocity (direction and magnitude) a net energy loss is obtained.

6.3.1   Reduced Dimensional Mapping

A reduced dimensional mapping has been shown to work [21, 24] previously for H_2 on
Cu(111) and N_2 on Ru(0001). Here the Cartesian coordinates of the two atoms A and
B with coordinates X_A, Y_A, Z_A and X_B, Y_B, Z_B are transformed first to the molecular
coordinate system $\mathbf{R}^{\mathsf{sph}} = \{X, Y, Z, d, \theta, \phi\}$, where

$$X = \frac{m_A}{M} X_A + \frac{m_B}{M} X_B, \tag{6.13a}$$

$$Y = \frac{m_A}{M} Y_A + \frac{m_B}{M} Y_B, \tag{6.13b}$$

$$Z = \frac{m_A}{M} Z_A + \frac{m_B}{M} Z_B, \tag{6.13c}$$

$$d = \sqrt{(X_B - X_A)^2 + (Y_B - Y_A)^2 + (Z_B - Z_A)^2}, \tag{6.13d}$$

$$\theta = \arccos\left(\frac{Z_B - Z_A}{d}\right), \tag{6.13e}$$

$$\phi = 2\pi \mathcal{H}(Y_A - Y_B) + \mathrm{sign}(Y_B - Y_A) \arccos\left(\frac{X_B - X_A}{\sqrt{(X_B - X_A)^2 + (Y_B - Y_A)^2}}\right), \tag{6.13f}$$

where $\mathcal{H}(x)$ is the heaviside step function and $\mathrm{sign}(x)$ yields the sign of x. Note
that for H_2, N_2 and other homo-nuclear diatomic molecules X_2 consisting of identical
isotopes the mass fractions are always one half since the mass of atom A and B are
equal $(m_A = m_B = m)$ and the total mass M is thus equal to $2m$. Figure 6.4 shows
how the Cartesian coordinates in X are transformed to the molecular coordinates in
Q. Next the reference molecular coordinate is computed by setting both angles to
$\theta_{\mathsf{ref}} = \phi_{\mathsf{ref}} = 90°$. The Jacobian is then computed for both the reference and original
coordinate and the matrix product of these two Jacobians yields a transformation
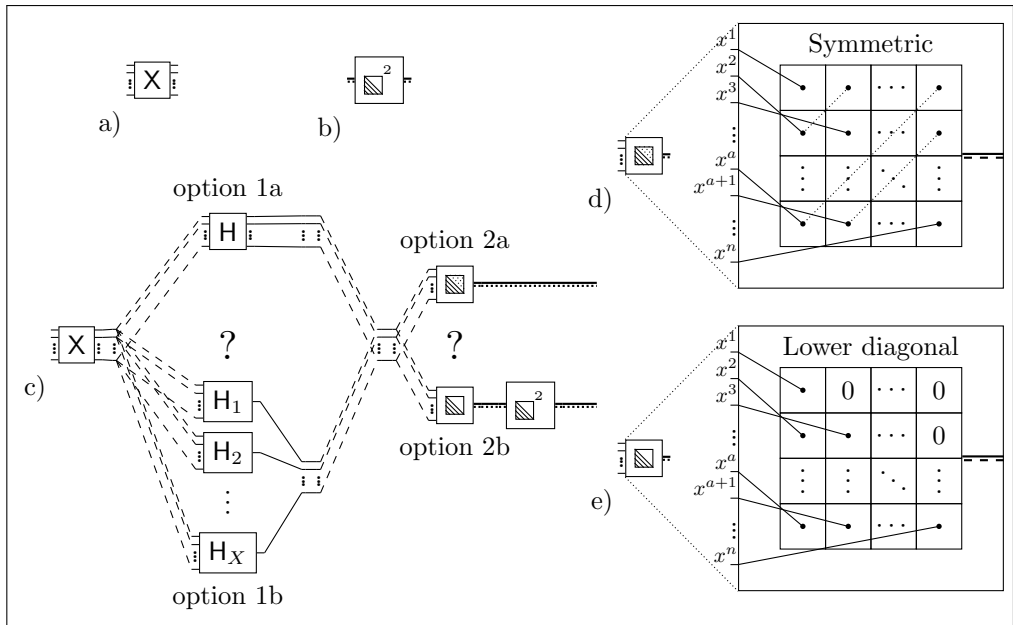
Figure 6.3: Schematic representation of how to use a hidden network for fitting a tensor field. a) Input vector to the NN(e.g. Cartesian coordinates). b) Multiplies a lower triangular matrix with its transpose. c) A tensor field is obtained by making two choices. First, the independent elements can be obtained using (1a) one hidden network with as many outputs as required elements or (1b) an hidden network with one output is used for every independent element. Second, the elements can be arranged directly in a symmetric fashion (2a) or a lower triangular can be obtained which is subsequently multiplied with its transpose to obtain a symmetric positive-definite tensor (2b). d) Shows the direct symmetric arrangement. e) Shows the lower triangular arrangement.
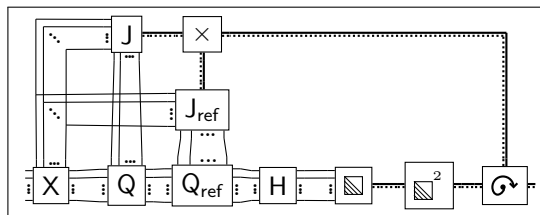
Figure 6.4: Schematic representation of the reduced dimensional mapping model used in Chap. 4 and Chap. 5 [21, 24]

.

tensor $\boldsymbol{T}(\mathbf{p}, \mathbf{p}_{\mathsf{ref}})$. Finally $\boldsymbol{T}(\mathbf{p}, \mathbf{p}_{\mathsf{ref}})$ is used to transform the output of the hidden network and subsequent positive definite arrangement. This transformation in this particular case is the same as taking the friction elements along the bond (d) of the molecule to be constant regardless of the chosen angular orientation. The coordinates that are given to the hidden network are $Q_{5...8}$ from Eq. 6.15 (*vide infra*) to also account for periodicity.

6.3.2 Piece-wise Mapping

Jiang and co-workers [22, 23] have shown that it is possible to obtain an accurate fit using a piece-wise mapping model. They have described this as applying subsequent symmetry operations until the mapping to the irreducible wedge is found. Here a slightly different approach is taken that yields the same result for a homonuclear-diatomic molecule X_2 consisting of identical isotopes.

To perform the mapping procedure, we first find the surface atom closest to the X_2 COM position and translate X_2 such that all molecules and up near the same surface atom. Secondly, the angle α_{map} is defined as the angle between the x-axis and the axis going through the formar surface atom and the X_2 COM projected on the surface plane. The X_2 molecule and concomitant friction tensor is then transformed

according to the symmetry operator $\hat{s}_?$ defined by the following case statement:

$$\hat{s}_? = \begin{cases} \hat{E} & \text{for } -\frac{1}{6}\pi < \alpha_{\mathsf{map}} \leq \frac{1}{6}\pi, \\[2mm] \hat{\sigma}_4 & \text{for } \frac{1}{6}\pi < \alpha_{\mathsf{map}} \leq \frac{3}{6}\pi, \\[2mm] \hat{C}_3^1 & \text{for } \frac{3}{6}\pi < \alpha_{\mathsf{map}} \leq \frac{5}{6}\pi, \\[2mm] \hat{\sigma}_2 & \text{for } \frac{5}{6}\pi < \alpha_{\mathsf{map}} \leq -\frac{5}{6}\pi, \\[2mm] \hat{C}_3^2 & \text{for } -\frac{3}{6}\pi < \alpha_{\mathsf{map}} \leq \frac{1}{6}\pi, \\[2mm] \hat{\sigma}_3 & \text{for } -\frac{5}{6}\pi < \alpha_{\mathsf{map}} \leq -\frac{3}{6}\pi. \end{cases} \tag{6.14}$$

These boundaries assign a different symmetry operator $\hat{s}_?$ depending at which of the 6 irreducable wedges (of the hexaganol surface) the X_2 COM is located. Applying the symmetry operator $\hat{s}_?$ then always maps the X_2 COM to the same irreducable wedge, namely the irreducable wedge that gets assigned the identy operator $\hat{E}$.

Jiang and co-workers also apply a permutation to the friction tensor of the coordinates associated with atom A and B if $Z_A > Z_B$. This method in principle takes care of the permutation symmetry, however, not correctly when the molecule is perpendicular to the surface. In practice, this is not a big issue for performing dynamics since the probability of being exactly perpendicular is very small. For the training set however, a significant amount of configurations where the molecule was exactly perpendicular was used thus amplifying this issue. The strategy of Jiang and co-workers has been adapted in this thesis by finding the Cartesian direction along which the separation between the two atoms is largest, and apply the permutation selection to that Cartesian direction instead of always along Z. This method is denoted as IW (irreducible wedge) henceforth. Additionally, a more simplified piece-wise mapping scheme has been used where the X_2 molecule is always mapped to a single unit cell (SUC). Using this method, the *a posteriori* method only requires a sum over all C_{3v} and permutation symmetries and not the translational symmetries (as those are included in the mapping). Note that a purely translational mapping does not introduce a transformation of the tensor, tensors elements are invariant under this operation.
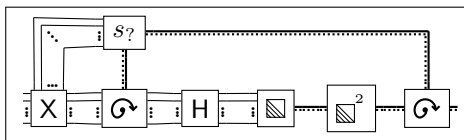
Figure 6.5: Schematic representation of the piece-wise mapping method.

6.3.3 Symmetry Adapted Coordinate Mapping

For the symmetry adapted coordinate mapping used in this thesis, the following symmetry adapted coordinates [27] are used

$$Q_1 = \frac{1}{2}\left[\exp\left(\frac{Z_A}{2}\right) \cdot g_1\left(X_A, Y_A\right) + \exp\left(\frac{Z_B}{2}\right) \cdot g_1\left(X_B, Y_B\right)\right] \tag{6.15a}$$

$$Q_2 = \exp\left(\frac{Z_A}{2}\right) \cdot g_1\left(X_A, Y_A\right) \cdot \exp\left(\frac{Z_B}{2}\right) \cdot g_1\left(X_B, Y_B\right) \tag{6.15b}$$

$$Q_3 = \frac{1}{2}\left[\exp\left(\frac{Z_A}{2}\right) \cdot g_2\left(X_A, Y_A\right) + \exp\left(\frac{Z_B}{2}\right) \cdot g_2\left(X_B, Y_B\right)\right] \tag{6.15c}$$

$$Q_4 = \exp\left(\frac{Z_A}{2}\right) \cdot g_2\left(X_A, Y_A\right) \cdot \exp\left(\frac{Z_B}{2}\right) \cdot g_2\left(X_B, Y_B\right) \tag{6.15d}$$

$$Q_5 = \exp\left(\frac{Z}{2}\right) \cdot g_1\left(X, Y\right) \tag{6.15e}$$

$$Q_6 = \exp\left(\frac{Z}{2}\right) \cdot g_2\left(X, Y\right) \tag{6.15f}$$

$$Q_7 = \exp\left(\frac{Z}{2}\right) \tag{6.15g}$$

$$Q_8 = d \tag{6.15h}$$

$$Q_9 = \cos\left(\theta\right)^2, \tag{6.15i}$$

which are based on the Cartesian and molecular coordinates.

The g_1 and g_2 generate a unique coordinate for every symmetry equivalent x and

y along a C_{3v} surface (e.g. Ru(0001) and Cu(111)) according to

$$g_1\left(x,y\right) = g\left(x - \frac{a}{4}, y - \frac{a}{4\sqrt{3}}\right) \tag{6.16a}$$

$$g_2\left(x,y\right) = g\left(x + \frac{a}{4}, y + \frac{a}{4\sqrt{3}}\right) \tag{6.16b}$$

$$g\left(x,y\right) = \frac{1}{3\sqrt{3}}\left[\sin\left(\frac{2\pi}{a}\left(x - \frac{1}{\sqrt{3}}y\right)\right) + \sin\left(\frac{2\pi}{a}\left(\frac{2}{\sqrt{3}}y\right)\right) + \sin\left(\frac{2\pi}{a}\left(x + \frac{1}{\sqrt{3}}y\right)\right)\right] + \frac{1}{2}. \tag{6.16c}$$

Using this coordinate system, a tensor field with the correct symmetry behavior is obtained (see Figure 6.6a) by transforming to the $\mathbf{Q}$ coordinate system and transforming the result of the hidden network from $\mathbf{Q}$ to $\mathbf{R}$.

6.3.4 Symmetry Adapted Coordinate Mapping with Asymmetric Transformations

To include asymmetric contributions, the following alternative g functions, based on seperating the different terms in g from Eq. 6.16c, are defined

$$g^{\mathsf{one}}\left(x,y\right) = \frac{1}{3\sqrt{3}}\left[\sin\left(\frac{2\pi}{a}\left(x - \frac{1}{\sqrt{3}}y\right)\right)\right] \tag{6.17a}$$

$$g^{\mathsf{two}}\left(x,y\right) = \frac{1}{3\sqrt{3}}\left[\sin\left(\frac{2\pi}{a}\left(\frac{1}{\sqrt{3}}y\right)\right)\right] \tag{6.17b}$$

$$g^{\mathsf{three}}\left(x,y\right) = \frac{1}{3\sqrt{3}}\left[\sin\left(\frac{2\pi}{a}\left(x + \frac{1}{\sqrt{3}}y\right)\right)\right]. \tag{6.17c}$$

These g functions define corresponding coordinate systems Q and Jacobian tensors $\boldsymbol{J}\left(\mathbf{p}\right)$ that are used to transform the same output of the hidden network in Figure 6.6b and an average of these transformed results is taken. Note that the hidden network is evaluated only once, which results in a significant performance increase compared to the *a posteriori* method.

Any of the symmetry operators in the C_{3v} group either cause the swapping of two of these Jacobian tensors J, which changes the permutation order, or reorder them by pulling the last one to the front, which keeps the permutation order. In both cases, the averaging of the transformed result remains the same and thus this representation is symmetry invariant.
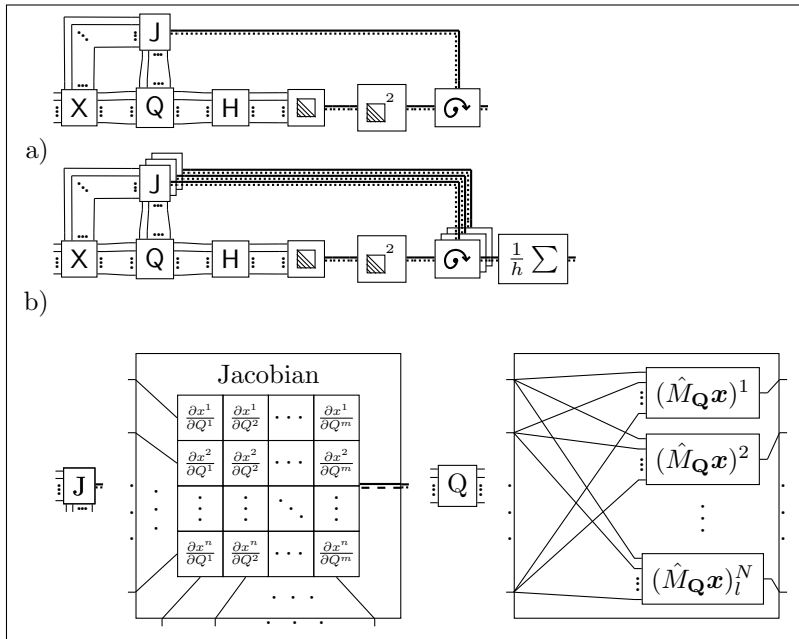
Figure 6.6: Schematic representation of the symmetry adapted coordinate mapping either without (a) or with (b) asymmetric transformations.
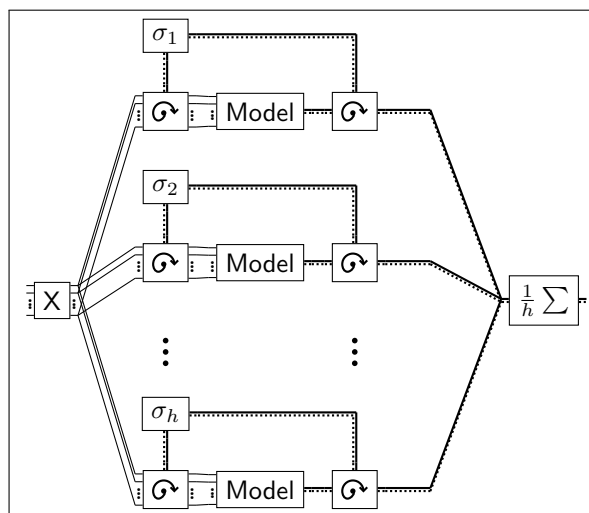
Figure 6.7: A schematic representation of the *a posteriori* architecture.

6.3.5   *a posteriori* Imposed Symmetry Behavior

The *a posteriori* method is implemented as shown schematically in Figure 6.7. For each symmetry operator in the C_{3v} group, the input coordinates are transformed and given to any of the previously discussed models. The result of these models are subsequently transformed and averaged.

6.4   Computational Details

TensorFlow [28] has been used for fitting the electronic friction tensors. The fitting parameters of the models were initialized using a normal distribution with $\mu = 0$ and $\sigma = \frac{1}{N_l}$ (N_l is the number of nodes in a specific layer) for the weights and $\sigma = 0.1$ for the biases. Next the RMSProp algorithm [29] is used in three consecutive runs of 100.000 epochs using a decay of 0.997 and a learning rate of 10^{-3}, 10^{-4}, and 10^{-5} for the first, second, and third run respectively. A training and test set was obtained by randomly shuffling the order of electronic friction tensors in the data set and assigning the first 10% of the data entries to the test set and the remaining data entries to the training set. Only the training set was used during the learning stage. A so-called committee

[30, 31] with 5 committee members was created by repeating all fitting procedures for each member with the same settings, but with different randomly initialized weights and biases. The training and test set shuffling was different for different committee member It has been kept the same for all machine learning models such that the respective committees are all presented the same training and test sets for the same member.

6.5 Results

Here a comparison is made between the different methods of obtaining continuous representations of friction tensors as discussed previously based on the root-mean-square errors (RMSEs). For each data set, both the RMSE of the training set and test set has been computed (see Sec. 6.4). The argument here is that the RMSE of the test set is a measure of how well the method is at continuously representing. The RMSE of the training set on the other hand shows the flexibility of the method. In particular, if the symmetry of the coordinate dependence is not correctly taken into account *a priori*, the training set may still yield a low RMSE if the data points in the training set are not sampled from different irreducible wedges. In contrast, the test set, which for this chapter is always replicated to other irreducible wedges, does yield a high RMSE if this symmetry is not taken into account properly.

All friction tensors discussed here are for N_2 on Ru(0001), where only the N_2 degrees of freedom are considered and the Ru(0001) surface is kept frozen in the hexagonal symmetry (including surface expansion in the lateral directions and interlayer relaxation that is representative for $T_s = 575K$). Ru(0001) is kept at its ideal configuration (but includes surface expansion and layer relaxation for 575K). Since the electronic friction tensor is symmetric, it has 21 independent elements for the 6 degrees of freedom of the N_2 molecule.

6.5.1 Reduced-Dimensional Models: Machine Learning Parameters

For this comparison, the data set of electronic friction tensors from Ref. [24] has been used, which directly accounts for the dependence of four of the six molecular coordinates. This data set has subsequently been fitted using the reduced dimensional method. This allows one to focus on how the friction tensor itself is represented rather than how the symmetry of the tensor field (i.e., the symmetry of the coordinate dependence) is included. Here the result of using one NN that produces the 21 independent elements as its output is compared with using 21 independent NNs (options 1a and 1b from Fig. 6.3, respectively). Moreover, a comparison is made between the procedure of obtaining 21 independent elements and arranging them in a symmetric tensor directly, and of obtaining 21 independent elements in a lower triangular tensor and subsequently squaring this tensor to obtain a positive-definite tensor (options 2a and 2b in Fig. 6.3, respectively). Finally, results obtained with different numbers of layers and nodes are compared with reference to the number of free parameters needed to construct the corresponding NN topologies.

Figure 6.8 shows the RMSEs for NN fits for directly obtaining a symmetric tensor (option 2a). When using a different NN for each element (option 1a), there is no substantial difference for the RMSE between using two or three NN layers over the wide range of NN topologies considered here. On the other hand, if a single NN to fit the entire tensor is used (option 1b) the RMSEs are significantly larger for two NN layers (not reported here). Apparently, in this case two layers are not enough and the additional NN layer is required to describe the difference between the different elements, in contrast to option 1a where using different NNs can provide this flexibility. The additional third layer under option 1a simply provides more fitting parameters, which is supported by the similar behavior of the RMSE as a function of the number of fitting parameters for both two and three layers as plotted in Fig. 6.8. Using option 1b with three layers performs significantly better than both two and three layers with option 1a with a much smaller number of fitting parameters. The minimum error is found with 15 nodes per layer (resulting in 891 fitting parameters in total). Option 1a with both two and three hidden layers only performs similar to option 1b f the number

of fitting parameters has the same order of magnitude as the number of data points.

Figure 6.9 shows the RMSEs for obtaining a lower triangular tensor and subsequently squaring it (option 2b). The RMSEs of option 1a with both two and three layers are again very similar in their behavior as a function of the number of fitting parameters. However, the range of the RMSE is slightly smaller as it is between 0.21 and 0.255 meVpsÅ^{-2} instead of 0.21 and 0.285 meVpsÅ^{-2} when comparing to the corresponding curves in Fig. 6.8. Option 1b on the other hand yields a higher RMSE if more than 2000 fitting parameters are used when combined with option 2b (Fig. 6.9) instead of option 2a (Fig. 6.8). For 10 and 15 nodes the results are essentially the same, in particular when considering the scattering over the respective neural network committees, while 21 and 25 nodes now give a lower RMSE with option 2b, with 21 nodes being the best fit.

The need for increasing the number of fitting parameters from 891 to 1971 in order to obtain the best fit when using option 2b over 2a is not surprising. When using option 2b the friction tensor is more constrained by construction and thus a larger number of parameters is required to obtain the same flexibility.

For the data set used here it is clear that using option 1b instead of 1a is clearly better. The same NN used to obtain the entire friction tensor yields better results for substantially fewer fitting parameters. Moreover, option 2b instead of 2a provides additional advantages: although the improvement to the RMSE is only 0.02 meVpsÅ^{-2} and comes at the cost of needing more fitting parameters, it ensures a positive definite and thus physically meaningful friction tensor by construction. This property is important for using friction tensors in the generalized Langevin equation (GLE) to perform molecular dynamics with electronic friction. Option 2a does not ensure that the result of the friction tensor is a dissipation of energy, it is possible that for some configurations the NN will predict an energy gain of the sy stem.

It is not clear whether these results generalize to other data sets. It is suggested here to use option 2b over option 2a as long as the RMSE is not influenced significantly. It is suspected here that option 1b will generally perform better than option 1a for the same number of fitting parameters, since the different friction tensor elements depend
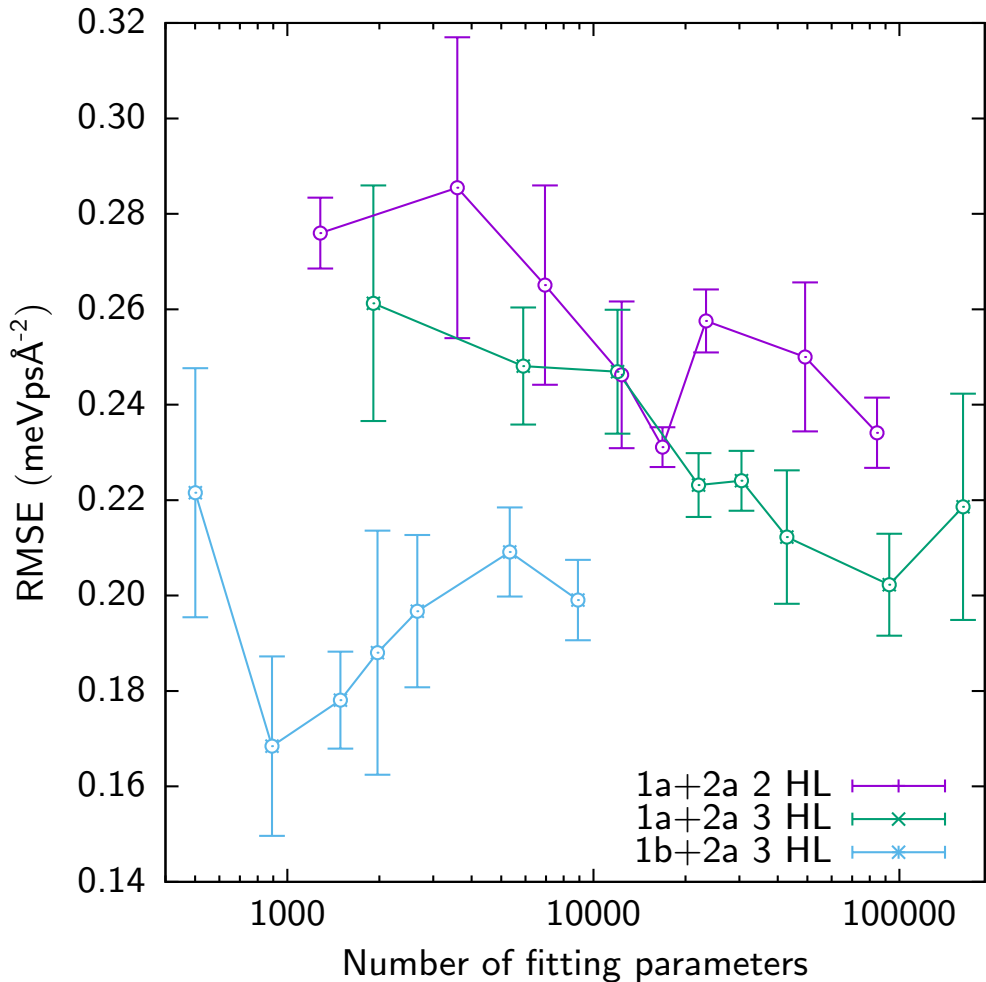
Figure 6.8: RMSE of the test set for the combination of options 1a+2a (details see text and Fig. 6.3) with 2 hidden layers (purple), options 1a+2a with 3 hidden layers (green), and options 1b+2a with 3 hidden layers (blue) as a function of the number of parameters (neural network weights and biases, on a logarithmic scale). Data points correspond to 5, 10, 15, 21, 25, 30, 45, and 60 nodes for each hidden layer in this order for option 1a while 5 nodes is ommited for option 1b due to too large errors. Error bars show the spread of RMSEs for different committee members (expressed as a RMSE itself). Note that since only a single NN is employed for the same amount of hidden nodes the blue curve corresponds to a factor of 20 fewer fitting parameters.
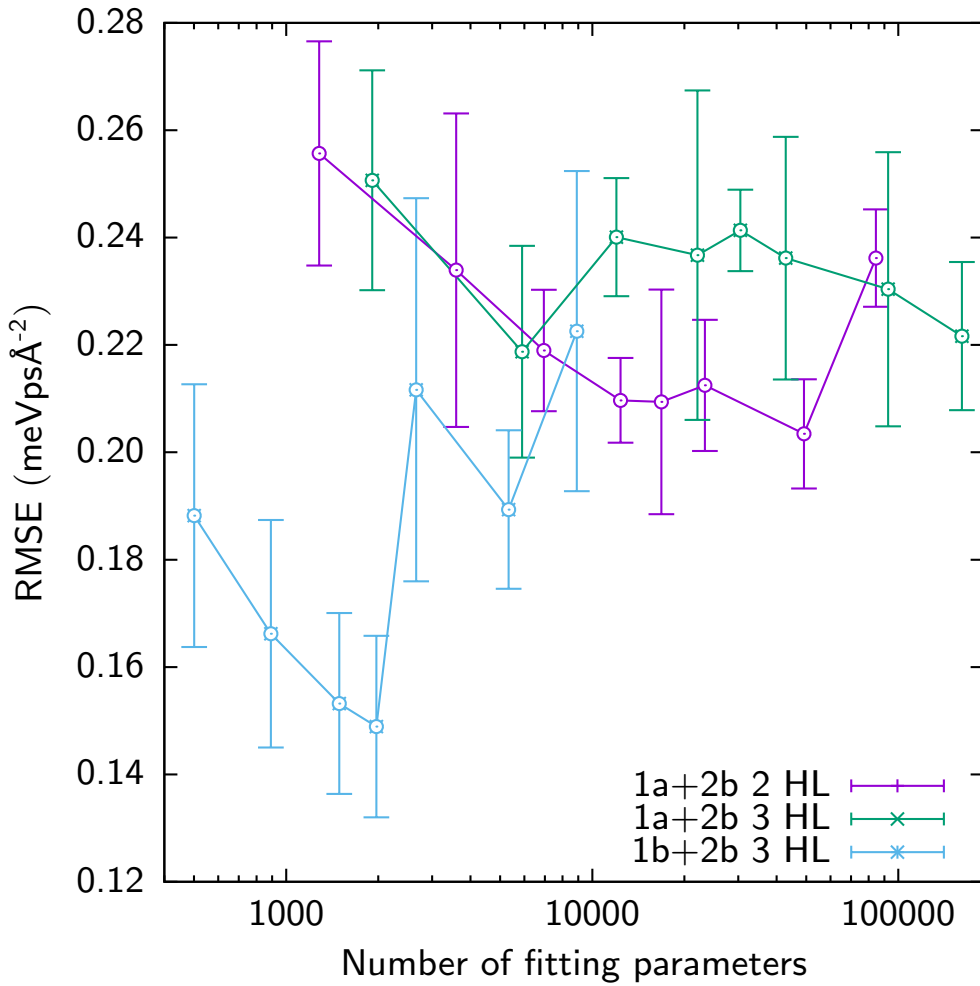
168

Figure 6.9: Same as Fig. 6.8, but for the combination of options 1a+2b with 2 hidden layers (purple), options 1a+2b with 3 hidden layers (green), and options 1b+2b with 3 hidden layers (blue).

similarly on the input coordinates. For example, all elements will be small when the molecule is far away from the surface. Using option 1b this information needs to be 'understood' by the NN only once while for option 1a this needs to be learned by all independent NNs. For results henceforth, option 1b is used in combination with 2b, together with three NN layers each with 21 nodes (using 25 nodes yields a comparatively small increase in fitting accuracy for a large increase in fitting parameters).

6.5.2   Six-Dimensional Symmetry Adapted Models

In order to assess the performance of the different symmetry adapted models, a 6D data set has been fitted with each method.

Fig. 6.10 shows the RMSEs of both the training and test set. Additionally, the amount of time needed for fitting is provided in hours per processor core. The single unit cell (SUC) piece-wise mapping (see Sec. 6.2.1) has been fitted in three ways: without any additional considerations (SUC in Fig. 6.10), using the *a posteriori* method (SUC-P) and by replicating the training set using the available symmetry operations (SUC-D). The SUC test RMSEs are the worst at 0.44 meVpsÅ^{-2} even though the training error is satisfactory. This is not a result of over-fitting, instead this is because the test set contains data from other irreducible wedges not included in the training set. Since there is no information available to the NN on how the friction tensors in different irreducible wedges are related and because there is not necessarily training data available in all regions, it is not possible for the NN to make good predictions. Using the SUC-P method substantially improves the description of the test RMSE at a slight setback of the training RMSE. Similar to previous arguments, this can be explained by the *a posteriori* method constraining the NN prediction which reduces flexibility. Inspection of the elements as a function of movement of N_2 along the Ru(0001) surface shows no jumps at the symmetry seams for SUC-P as expected. Replicating the training set for different irreducible wedges improves the test RMSE in the SUC-D method only slightly over the SUC method. While the SUC-D does have symmetry information available in the form of symmetrically replicated data, it misses the exact relation between and constraints of the individual elements, which is enforced

with the SUC-P.

The test and training RMSEs for all piece-wise mapping schemes based on the irreducible wedge (IW, see Sec. 6.3.2) are essentially the same (see Fig. 6.10). This is not surprising for IW and IW-D as the IW method already correctly takes into account symmetry. However, it was expected that IW-P, using the *a posteriori* method, no longer has the discontinuities at the symmetry seams present in IW. It turns out that they are still present since computational rounding errors (due to finite floating piont precision of the coordinates) can assign the N_2 molecule to the wrong irreducible wedges. This happens only when a data point is extremely close to the symmetry seam. No simple solution was found to circumvent these errors due to the large number of computations needed to obtain the mapping between irreducible wedges.

For the sym and asym methods (see Sec. 6.3.3 and Sec. 6.3.4 respectively) no results for the *a posteriori* and training data replication are shown in Fig. 6.10 because, as expected, the results are identical (only an increased computational effort was found). The sym method performs substantially worse due to the additional (nonphysical) constraint introduced along some directions at the symmetry seam which are not present in the asym method. Asym yields the smallest test RMSE (0.28 meVpsÅ^{-2}) with a similar training RMSE (0.20 meVpsÅ^{-2}) indicating that an accurate fit was obtained. There are no discontinuities at the symmetry seam for either method as the functional forms of these methods are completely continuous.

Generally the piece-wise models (SUC and IW) are computationally more expensive due to conditional statements present in the algorithm for mapping back to surface unit cell or irreducible wedge. The *a posteriori* method and training data replication method both increase the computational effort. Due to the additional input coordinate transformations and output tensor transformations necessary in the *a posteriori* method it is the most expensive. The *a priori* methods based on symmetry-adapted coordinates (sym and asym) are the computationally cheapest methods.
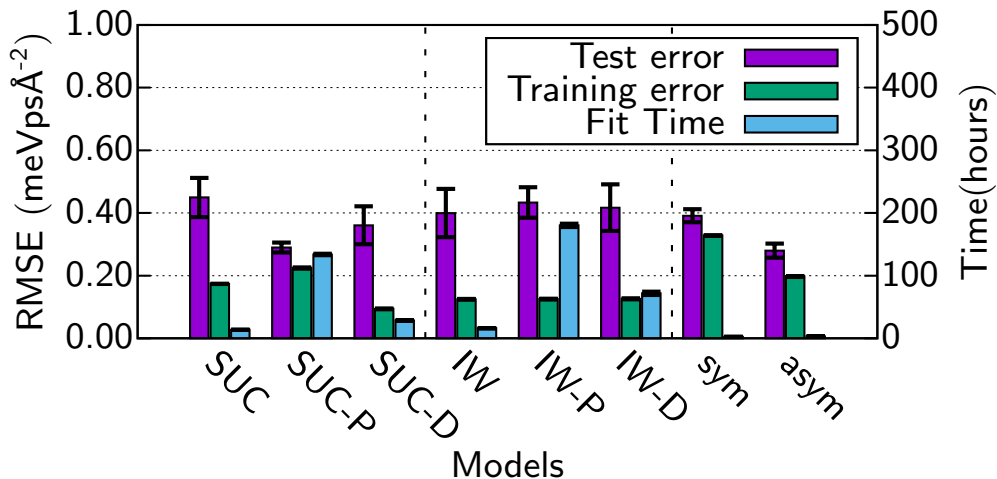
6

Figure 6.10: RMSE of test (purple) and training (green) data sets for several fitting models (see explanations in text) as well as concomitant fitting times (blue) in hours per processor core.

6.6 Conclusions

This chapter has introduced several strategies for obtaining continuous representations of friction tensors based on the properties of tensors under coordinate transformations. Obtaining all friction tensor elements using a single neural network with multiple outputs results in more accurate fits and additionally requires a substantially smaller number of fitting parameters. Positive-definite friction tensors were obtained by generating a lower triangular tensor and subsequently squaring it, which did not introduce additional difficulties for fitting the friction tensors compared to obtaining symmetric tensors only.

The piece-wise mapping procedure targetting the irreducible wedge, which is based on the work of Jiang and coworkers [22], yields accurate fits of the electronic friction tensors, albeit without exact compliance with the exact tensorial symmetry. Future dynamical studies are likely to confirm that the small concomittant RMSEs do not (significantly) affect calculated observables. From an analytical point of view these

discontinuities should be removed if the *a posteriori* method is used, this turned out to not work in practice due to computational rounding errors. As expected, the symmetry adapted machine learning model developed here properly captures the symmetry of the friction tensor. However, additional constraints are imposed which prevent an accurate fit in some regions. Most notably, constraints at the symmetry seams that should only be applicable for off-diagonal elements are also present for diagonal elements. The asymmetric tensor model has none of the above problems and yields the most accurate fit. Surprisingly, taking a simplified piece-wise mapping model targetting the entire surface unit cell yields almost the same accuracy when combined with the *a posteriori* method.

References

[1] J. Behler and M. Parrinello. "Generalized Neural-Network Representation of High-Dimensional Potential-Energy Surfaces". In: *Phys. Rev. Lett.* 98 (2007), p. 146401. DOI: 10.1103/PhysRevLett.98.146401.

[2] J. Behler. "Representing Potential Energy Surfaces by High-Dimensional Neural Network Potentials". In: *J. Phys. Condens. Matter* 26 (2014), p. 183001. DOI: 10.1088/0953-8984/26/18/183001.

[3] J. Behler. "Constructing High-Dimensional Neural Network Potentials: A Tutorial Review". In: *Int. J. Quantum Chem.* 115 (2015), pp. 1032–1050. DOI: 10.1002/qua.24890.

[4] A. Singraber, J. Behler, and C. Dellago. "Library-Based LAMMPS Implementation of High-Dimensional Neural Network Potentials". In: *J. Chem. Theory Comput.* (2019). DOI: 10.1021/acs.jctc.8b00770.

[5] A. P. Bartók, M. C. Payne, R. Kondor, and G. Csányi. "Gaussian Approximation Potentials: The Accuracy of Quantum Mechanics, without the Electrons". In: *Phys. Rev. Lett.* 104 (2010), p. 136403. DOI: 10.1103/PhysRevLett.104.136403.

[6] A. Grisafi, D. M. Wilkins, G. Csányi, and M. Ceriotti. "Symmetry-Adapted Machine Learning for Tensorial Properties of Atomistic Systems". In: *Phys. Rev. Lett.* 120 (2018), p. 036002. DOI: 10.1103/PhysRevLett.120.036002.

[7] M. Rupp, A. Tkatchenko, K.-R. Müller, and O. A. von Lilienfeld. "Fast and Accurate Modeling of Molecular Atomization Energies with Machine Learning". In: *Phys. Rev. Lett.* 108 (2012), p. 058301. DOI: 10.1103/PhysRevLett.108.058301.

6

[8] K. T. Schütt, F. Arbabzadah, S. Chmiela, K. R. Müller, and A. Tkatchenko. "Quantum-Chemical Insights from Deep Tensor Neural Networks". In: *Nat. Commun.* 8 (2017), p. 13890. DOI: 10.1038/ncomms13890.

[9] K. T. Schütt, H. E. Sauceda, P.-J. Kindermans, A. Tkatchenko, and K.-R. Müller. "SchNet – A Deep Learning Architecture for Molecules and Materials". In: *J. Chem. Phys.* 148 (2018), p. 241722. DOI: 10.1063/1.5019779.

[10] S. Chmiela, A. Tkatchenko, H. E. Sauceda, I. Poltavsky, K. T. Schütt, et al. "Machine Learning of Accurate Energy-Conserving Molecular Force Fields". In: *Sci. Adv.* 3 (2017), e1603015. DOI: 10.1126/sciadv.1603015.

[11] S. Chmiela, H. E. Sauceda, I. Poltavsky, K.-R. Müller, and A. Tkatchenko. "sGDML: Constructing Accurate and Data Efficient Molecular Force Fields Using Machine Learning". In: *Comp. Phys. Comm.* 240 (2019), pp. 38–45. DOI: 10.1016/j.cpc.2019.02.007.

[12] B. Jiang and H. Guo. "Permutation Invariant Polynomial Neural Network Approach to Fitting Potential Energy Surfaces. III. Molecule-Surface Interactions". In: *J. Chem. Phys.* 141 (2014), p. 034109. DOI: 10.1063/1.4887363.

[13] B. Kolb, X. Luo, X. Zhou, B. Jiang, and H. Guo. "High-Dimensional Atomistic Neural Network Potentials for Molecule–Surface Interactions: HCl Scattering from Au(111)". In: *J. Phys. Chem. Lett.* 8 (2017), pp. 666–672. DOI: 10.1021/acs.jpclett.6b02994.

[14] K. Shakouri, J. Behler, J. Meyer, and G.-J. Kroes. "Accurate Neural Network Description of Surface Phonons in Reactive Gas–Surface Dynamics: N_2 + Ru(0001)". In: *J. Phys. Chem. Lett.* 8 (2017), pp. 2131–2136. DOI: 10.1021/acs.jpclett.7b00784.

[15] J. Behler, S. Lorenz, and K. Reuter. "Representing Molecule-Surface Interactions with Symmetry-Adapted Neural Networks". In: *J. Chem. Phys.* 127 (2007), p. 014705. DOI: 10.1063/1.2746232.

[16] S. Chmiela, H. E. Sauceda, K.-R. Müller, and A. Tkatchenko. "Towards Exact Molecular Dynamics Simulations with Machine-Learned Force Fields". In: *Nat. Commun.* 9 (2018), pp. 1–10. DOI: 10.1038/s41467-018-06169-2.

[17] M. Head-Gordon and J. C. Tully. "Molecular Dynamics with Electronic Frictions". In: *J Chem Phys* 103 (1995), pp. 10137–10145. DOI: 10.1063/1.469915.

[18] M. Alducin, R. Díez Muiño, and J. I. Juaristi. "Non-Adiabatic Effects in Elementary Reaction Processes at Metal Surfaces". In: *Prog. Surf. Sci.* 92 (2017), pp. 317–340. DOI: 10.1016/j.progsurf.2017.09.002.

[19] W. Dou and J. E. Subotnik. "Perspective: How to Understand Electronic Friction". In: *J. Chem. Phys.* 148 (2018), p. 230901. DOI: 10.1063/1.5035412.

6

[20] R. J. Maurer, B. Jiang, H. Guo, and J. C. Tully. "Mode Specific Electronic Friction in Dissociative Chemisorption on Metal Surfaces: H_2 on Ag(111)". In: *Phys. Rev. Lett.* 118 (2017), p. 256001. DOI: 10.1103/PhysRevLett.118.256001. arXiv: 1705.09753 [cond-mat.mtrl-sci].

[21] P. Spiering and J. Meyer. "Testing Electronic Friction Models: Vibrational De-Excitation in Scattering of H_2 and D_2 from Cu(111)". In: *J. Phys. Chem. Lett.* 9 (2018), pp. 1803–1808. DOI: 10.1021/acs.jpclett.7b03182.

[22] R. J. Maurer, Y. Zhang, H. Guo, and B. Jiang. "Hot Electron Effects during Reactive Scattering of H_2 from Ag(111): Assessing the Sensitivity to Initial Conditions, Coupling Magnitude, and Electronic Temperature". In: *Faraday Discuss.* 214 (2019), pp. 105–121. DOI: 10.1039/C8FD00140E.

[23] Y. Zhang, R. J. Maurer, H. Guo, and B. Jiang. "Hot-Electron Effects during Reactive Scattering of H_2 from Ag(111): The Interplay between Mode-Specific Electronic Friction and the Potential Energy Landscape". In: *Chem. Sci.* 10 (2019), pp. 1089–1097. DOI: 10.1039/C8SC03955K.

[24] P. Spiering, K. Shakouri, J. Behler, G.-J. Kroes, and J. Meyer. "Orbital-Dependent Electronic Friction Significantly Affects the Description of Reactive Scattering of N_2 from Ru(0001)". In: *J. Phys. Chem. Lett.* 10 (2019), pp. 2957–2962. DOI: 10.1021/acs.jpclett.9b00523.

[25] M. Askerka, R. J. Maurer, V. S. Batista, and J. C. Tully. "Role of Tensorial Electronic Friction in Energy Transfer at Metal Surfaces". In: *Phys. Rev. Lett.* 116 (2016), p. 217601. DOI: 10.1103/PhysRevLett.116.217601.

[26] D. Novko, M. Blanco-Rey, M. Alducin, and J. I. Juaristi. "Surface Electron Density Models for Accurate *Ab Initio* Molecular Dynamics with Electronic Friction". In: *Phys. Rev. B* 93 (2016), p. 245435. DOI: 10.1103/PhysRevB.93.245435.

[27] J. Meyer. "Ab Initio Modeling of Energy Dissipation during Chemical Reactions at Transition Metal Surfaces". PhD thesis. Freie Universität Berlin, Freie Universität Berlin, Germany, 2012.

[28] M. Abadi, A. Agarwal, P. Barham, E. Brevdo, Z. Chen, et al. "TensorFlow: Large-Scale Machine Learning on Heterogeneous Systems". In: (2015). Software available from tensorflow.org.

[29] T. Tieleman and G. Hinton. "Lecture 6.5-Rmsprop: Divide the Gradient by a Running Average of Its Recent Magnitude". In: *COURSERA Neural Netw. Mach. Learn.* 4.2 (2012), pp. 26–31.

[30] S. Manzhos and T. Carrington. "A Random-Sampling High Dimensional Model Representation Neural Network for Building Potential Energy Surfaces". In: *J. Chem. Phys.* 125 (2006), p. 084109. DOI: 10.1063/1.2336223.

6

175

[31]   S. Manzhos, R. Dawes, and T. Carrington. "Neural Network-Based Approaches for Building High Dimensional and Quantum Dynamics-Friendly Potential Energy Surfaces". In: *Int. J. Quantum Chem.* 115 (2015), pp. 1012–1020. DOI: 10.1002/qua.24795.

6

Samenvatting

Reacties van moleculen op metaaloppervlakken zijn van levensbelang voor de samenleving in het hedendaagse tijdsgewricht. Zo is er bijvoorbeeld het Haber-Bosch proces, waarbij een mengsel van stikstofgas en waterstofgas omgezet wordt in ammonia door middel van een katalysator met metaaloppervlakken. Ongeveer de helft van de wereldbevolking wordt gevoedt door gewassen die bemest zijn met kunstmest vervaardigd uit, onder andere, ammonia geproduceerd middels het Haber-Bosch proces. Zeker één procent van het jaarlijks verbruik van primaire energie in de wereld is ten gunste van dit proces. Het is daarom ook niet verwonderlijk dat er meerdere Nobel-prijzen gewonnen zijn voor het verkrijgen van fundamentele kennis over reacties van moleculen op metaal oppervlakken.

Het hoofdonderwerp van dit proefschrift is de theoretische beschrijving van de reactieve verstrooiing van kleine moleculen aan overgangsmetaaloppervlakken, waarbij het Born-Oppenheimer statische oppervlaktemodel (BOSO) model niet langer gebruikt wordt. Reactieve verstrooiing vindt plaats bij een experiment waarbij een bundel van moleculen, in een specifieke quantummechanische toestandsverdeling, wordt afgeschoten op een metaal oppervlak. Deze moleculen kunnen dan óf reageren, waarbij één of meerdere chemische bindingen worden gevormd of verbroken, óf verstrooien, waarna de verstrooide moleculen zich in een andere quantummechanische toestanden kunnen bevinden, afhankelijk van het metaal oppervlak. Een belangrijk doel is het verkrijgen van fundamenteel begrip van de processen die de uitwisseling van energie tussen moleculen en metaaloppervlakken bepalen door simulaties op verschillende niveaus van theorie

zowel met elkaar als met experimentele resultaten te vergelijken. In het bijzonder wordt energie-uitwisseling waarbij de Born-Oppenheimer-benadering niet langer wordt gebruikt vanwege electronisch niet adiabatische excitaties die veroorzaakt worden door het ontbreken van een verboden zone in de bandstructuur van het metaaloppervlak. op het niveau van moleculaire dynamica met electronische wrijving (MDEW) vergeleken met experimenten.

In hoofdstuk 3 is het doel om een eerder ontwikkeld statischverruwingsmodel (SVM) te verbeteren om reactieve verstrooiing bij verhoogde oppervlaktetemperaturen te beschrijven. Een grote database van energieën van oppervlakteatoomverplaatsingen van een oppervlakte-adsorbaatsysteem is noodzakelijk voor het construeren en valideren van het verbeterde SVM. Het SVM, dat reactieve verstrooiing bij verhoogde temperaturen beschrijft en gebaseerd is op de "sudden" (plotselinge verandering) benadering, werd verbeterd door drie-lichaam interacties toe te voegen voor H_2 op Cu(111). De verbetering werd bereikt door de parameters van een eerder gepubliceerd model lineair afhankelijk te maken van de H_2 bindingsafstand en dus effectief drie-lichaamseffecten mee te nemen. Het drielichaams-SVM werd opgesteld met behulp van 15,113 configuraties met één of twee oppervlakatoomverplaatsingen. Bij verhoogde oppervlaktetemperaturen van 900K worden nauwkeurig gemeten experimentele reactiekansen van associatieve desorptie accuraat nagebootst door 6-dimensionale dynamische berekeningen met de specifiekereactieparameter-48-dichtheidsfunctionaal in combinatie met het SVM, alsmede met volledig dimensionale dynamica (d.w.z. ab initio moleculaire dynamica).

Theorie en experiment zijn niet in overeenstemming voor moleculen in de rovibrationele grondtoestand. Dit wordt toegeschreven aan de intrinsieke, en niet de extrinsieke, kromming van het potentiele-energieoppervlak langs het minimale energiepad. Gezien de sudden-benadering in het SVM, kan dus worden geconcludeerd dat oppervlaktebeweging niet belangrijk is om een chemisch nauwkeurige beschrijving van deze experimenten voor H_2 op Cu(111) te verkrijgen. Het is echter noodzakelijk om rekening te houden met de verandering van de H_2-Cu(111) interactiepotentiaal doordat Cu atomen bij verhoogde temperaturen van hun evenwichtspositie worden verplaatst.

In hoofdstuk 4 ligt de focus op het nauwkeurig beschrijven van elektronisch niet-adiabatische effecten voor de reactieve verstrooiing van H_2 en D_2 op Cu(111) met behulp van elektronische wrijvingstheorie. Een continue weergave van de wrijvings-tensor is noodzakelijk om de grote hoeveelheid trajecten te verkrijgen die vereist zijn voor het met voldoende statistisch bewijs berekenen van waarneembare waarden zoals de dissociatieve-chemisorptiewaarschijnlijkheid en rovibrationeel (in)elastische verstrooiingswaarschijnlijkheden. Coëfficiënten van orbitaalafhankelijke wrijving (OAW) werden berekend voor H_2 op een bevroren Cu(111) oppervlak om 6×6 elektronische wrijvingstensoren te verkrijgen. Er is een goede overeenstemming gevonden tussen de nieuw berekende en eerder (zeer beperkte) gerapporteerde wrijvingstensoren langs een reactiepad dat dissociatie beschrijft. De 21 onafhankelijke elementen van deze tensoren werden vervolgens bijeengebracht om een continue neuraal netwerk (NN) representatie met symmetrie aangepaste coördinaten te construeren. Elektronische wrijvingscoëfficiënten volgens de lokale-dichtheidswrijvingsbenadering (LDWB) werden ook berekend op basis van de elektronendichtheid van het schone Cu(111) oppervlak door beide waterstofatomen als onafhankelijk te behandelen en continu weer te geven door middel van een NN. MDEW simulaties die experimenten met moleculaire bundels nabootsen met behulp van zowel OAW als LDWB coëfficiënten toonden geen wezenlijk verschillende H_2 dissociatie-kansen ten opzichte van elkaar, in vergelijking met simulaties zonder elektronische wrijving (d.w.z. binnen de BOSO).

Anderzijds worden verstrooiingskansen van toestand naar toestand sterk beïnvloed door het meenemen van elektronische wrijving. Hiervoor maakt het ook uit of OAW of LDWB wordt gebruikt als het wrijvingsmodel. Bovendien maakt het bij het vergelijken van het verschil in initiële en uiteindelijke kinetische energie, voor deze simulaties van toestand naar toestand verstrooide moleculen, het mogelijk om onderscheid te maken tussen de OAW en LDWB modellen. Dit suggereert dat er 'vingerafdruk'-experimenten bestaan die gebruikt kunnen worden voor het valideren van de inherente benaderingen die gebruikt zijn voor de totstandkoming van beide modellen.

In hoofdstuk 5 wordt OAW gebruikt om de reactieve verstrooiing van N_2 op Ru(0001) te modelleren omdat eerder experimenteel en theoretisch werk van Luntz en collega's

had gesuggereerd dat niet-adiabatische effecten voor dit systeem van groot belang kunnen zijn. Een continue NN representatie werd verkregen voor OAW tensors van N_2 op Ru(0001). Moleculaire bundelsimulaties met behulp van MDEF zijn uitgevoerd inclusief de effecten van oppervlaktebeweging door verhoogde oppervlaktetemperaturen $(T_s = 575\text{K})$.

De initiële dissociatieve-chemisorptiewaarschijnlijkheden voor N_2 op Ru(0001) zijn ongeveer twee keer kleiner wanneer OAW wordt gebruikt als het wrijvingsmodel in vergelijking met LDWB, waardoor nu ook betere overeenstemming is met de beste momenteel beschikbare experimentele gegevens. Net als voor de meeste andere systemen levert LDWB nagenoeg dezelfde resultaten op als simulaties zonder elektronische wrijving.

Na rekening te hebben gehouden met de beste schattingen op basis van experimentele gegevens, verbetert OAW ook de beschrijving van energie-overdracht naar de vibratietoestand van het molecuul. Eén van de belangrijkste uitdagingen voor het beschrijven van N_2 verstrooiing van Ru(0001) is de juiste beschrijving van het verminderen van vibratie-excitatie. OAW was het enige model dat voldoende vermindering voorspelt om binnen de experimenteel bepaalde grenzen te vallen. Alleen wanneer rekening werd gehouden met zowel oppervlaktebeweging als OAW was het mogelijk om experimenten nauwkeurig na te bootsen.

In hoofdstuk 6 is het doel om modellen voor machinaal leren te ontwikkelen voor continue representaties van elektronische wrijvingstensoren, die rekening houden met symmetrie-eigenschappen van molecuuloppervlaksystemen, en die onderling te vergelijken

Eerst wordt een formalisme gepresenteerd om de symmetrie-eigenschappen van elektronische wrijvingstensoren voor moleculen op bevroren metaaloppervlakken te beschrijven. Er worden twee methoden voorgesteld waarmee deze eigenschappen kunnen worden opgelegd in algoritmen voor machinaal leren: een "*a priori*" en een "*a posteriori*" methode. Deze methoden kunnen worden gezien als een uitbreiding van gevestigde methoden die worden gebruikt om symmetrie-aangepaste potentiële energieoppervlakken te verkrijgen. Voor symmetrie-aangepaste, op machinaal leren gebaseerde poten-

tiële energie-oppervlakken wordt het neurale netwerk gerepresenteerd met symmetrie-aangepaste coördinaten of descriptoren, zodat het neurale netwerk hetzelfde resultaat oplevert voor symmetrisch equivalente invoer. Voor tensoren is het noodzakelijk om de uitvoer ook op een symmetrie-aangepaste manier te transformeren. In dit hoofdstuk wordt een vergelijking gemaakt tussen verschillende symmetrie-aangepaste en op neurale netwerken gebaseerde machinaal-leermodellen op basis van aanpasnauwkeurigheid en rekenefficiëntie. Het beste resultaat wordt verkregen voor een analytische "*a priori*" continue weergave met gebruik van "asymmetrische" bijdragen. Een andere nauwkeurige methode is om een eenvoudige uitdrukking te gebruiken om coördinaten toe te wijzen aan een enkele eenheidscel en vervolgens de "*a posteriori*" methode toe te passen om de juiste symmetriebeperking te verwezenlijken. Ook blijkt een methode op basis van het werk van Jiang en collega's nauwkeurige representaties op te leveren, hoewel er discontinuïteiten worden gevonden. Bovendien worden twee verschillende manieren om tensoren te verkrijgen als uitvoer van neurale netwerken vergeleken. De elementen van de tensor kunnen worden verkregen door een uniek neuraal netwerk aan elk element toe te wijzen, of door een neuraal netwerk met meerdere uitvoeren te construeren en deze uitvoeren vervolgens te rangschikken als een tensor. Positief-definiete tensoren kunnen worden afgedwongen door een lagere driehoekige tensor te genereren die vervolgens wordt gekwadrateerd. De beste resultaten worden verkregen voor neurale netwerken met meerdere uitvoeren waarbij aan de tensoren wordt opgelegd dat ze positief-definiet zijn. dutch

Curriculum Vitae

Paul Spiering was born on the 21$^{\text{st}}$ of November 1990 in Bergschenhoek (the Netherlands). From 2003 to 2009 he followed pre-university education (Voorbereidend Wetenschappelijk Onderzoek) at the Wolvert van Borselen scholengemeenschap in Rotterdam (the Netherlands). He received his B.Sc. degree in Molecular Science and Technology in 2012 from both the Technical University Delft and Leiden University. Continuing his studies at Leiden University, he received his Chemistry M.Sc. degree in 2015. His studies also included a six-month long assessed internship with Royal Dutch Shell in Rijswijk (the Netherlands). From 2014 up until 2017, Paul has been the treasurer of Stichting Kinderkampen Delftsche Zwervers. In 2015, Paul started with his PhD research in the group of dr. Jörg Meyer at the Leiden Institute of Chemistry in the Netherlands. His research was funded by Netherlands Organisation for Scientific Research (NWO).

List of Publications

[1] P. Spiering and J. Meyer. "Machine-Learning Based Continuous Representations of Electronic Friction Tensors". In preparation.

[2] P. Wright, P. Spiering, M. F. Somers, and J. Meyer. "Beyond the Frozen Surface-Approximation for H_2 on Cu(111): Rydberg Potentials vs Neural Networks". In preparation.

[3] P. Spiering and J. Meyer. "Testing Electronic Friction Models: Vibrational De-Excitation in Scattering of H_2 and D_2 from Cu(111)". In: *J. Phys. Chem. Lett.* 9 (2018), pp. 1803–1808.

[4] P. Spiering, M. Wijzenbroek, and M. F. Somers. "An Improved Static Corrugation Model". In: *J. Chem. Phys.* 149 (2018), p. 234702.

[5] P. Spiering, K. Shakouri, J. Behler, G.-J. Kroes, and J. Meyer. "Orbital-Dependent Electronic Friction Significantly Affects the Description of Reactive Scattering of N_2 from Ru(0001)". In: *J. Phys. Chem. Lett.* 10 (2019), pp. 2957–2962.

Afterword

Having finished all the requirements in order to publicly defend this thesis, and the research that I have performed as part of my PhD candidacy, I want to thank several people whom deserve my eternal gratitude.

First and foremost I would like to thank my PhD advisor *Jörg Meyer*. Working *with* you was a pleasure. I am also greatly indebted to prof. *Geert-Jan Kroes*, for hosting me and my research. *Mark Somers* has taught me all the skills I needed in order to start my PhD during my Master internship, for which I am still grateful. I am not sure how I would have been able to cope without your mentorship.

Next I would like to thank my colleagues:
Marc van Hemert for the times I needed a perspective wider than my own research,
Katharina, Sayan, Seeni, Soroush, Thanja, Andy, Bauke, Elham, Francesco, Gernot, Helen, Khosrow, Mark and *Theophile* for all the great times we had,
Davide, *Guido* and *Nick* for all the drinks, "jokes", goofing around and all the other things that are completely unrelated to work yet necessary for me to stay productive,
Also my students *Tim* and *Derk* have greatly contributed towards my fundamental understanding.

I would also like to thank all the friends I have made during my BHV activities. For helping me keep my stress levels acceptable, I thank *Arie, Bart, Bart, Guido, Jorrit, Koos, Maarten, Marloes, Robin, Rodi, Rutger* and *Ruud* for joining me for snowboarding vacations.

Finally I thank my family for their support. I will always miss you mom.